The Pennsylvania State University

The Graduate School

THIN-FILM PZT ON POLYMER AND GLASS SUBSTRATES: BREAKING THE RULES

A Dissertation in

Electrical Engineering

by

Tianning Liu

Submitted in Partial Fulfillment
of the Requirements
for the Degree of

Doctor of Philosophy

December 2020

The dissertation of Tianning Liu was reviewed and approved by the following:

Thomas N. Jackson
Dissertation Adviser
Chair of Committee
Robert E. Kirby Chair Professor of Electrical Engineering

Susan Trolier-McKinstry
Dissertation Co-Adviser
Co-Chair of Committee
Steward S. Flaschen and Evan Pugh Professor of Ceramic Science and Engineering &
Professor of Electrical Engineering

Mehdi Kiani
Dorothy Quiggle Career Development Assistant Professor of Electrical Engineering

Christopher Rahn
J. "Lee" Everett Professor of Mechanical Engineering

Kultegin Aydin
Professor of Electrical Engineering
Department Head of Electrical Engineering

Abstract

This dissertation investigates the material properties, device performances, and processing techniques for lead zirconate titanate (PZT) thin-films on flexible polymer and curved glass substrates.

For the study of PZT films on polymeric substrates, a release process has been developed to transfer high temperature crystallized PZT films from Si to thin layers of solution-cast polyimide through dissolution of an underlying sacrificial etch layer. This process not only enabled the assessment of domain responses in fully released piezoelectric films as a result of declamping, but also made useful contributions to the development of flexible piezoelectric devices. For a 1 μm thick blanket PZT film transferred to a 5 μm thick polyimide layer, superior electrical properties resulted relative to the same films on Si. Polarization-electric field hysteresis measurements showed a ~45% increase in the remanent polarization (from 17.5 μC/cm^2 to 26 μC/cm^2). High-temperature poling either induced more ferroelectric and ferroelastic realignment or significantly increased the density of domain walls in released films, which resulted in a reduction in relative permittivity of 17% compared to only 3% for clamped films. These measurement results confirmed the correlation between the reduced substrate clamping and improved domain wall mobility in released PZT films on polymeric substrates. Evaluation of piezoelectric responses in the released state was attempted through measurements of d_{33} using a commercial double-beam laser interferometer. Windows were etched in the polyimide layer so that the laser beams could directly probe the top and bottom electrodes of the released PZT structure. However, large apparent d_{33} values were measured due to a critical error associated with excess bending in the PZT membrane. Though correct d_{33} data in the released state were not successfully obtained, the experiments identified a critical artifact in the system, which has been overlooked by reports in the literature.

The above progress in the development of released PZT films enabled the design and fabrication of flexible ultrasonic transducers using 1 μm thick PZT on 5 μm thick polyimide substrates. The transducers were patterned single elements of PZT bar-resonators operating in width extension mode with center frequencies in the 8-80 MHz range. Pitch-catch was demonstrated with two 100 μm × 1000 μm

neighboring elements respectively transmitting and receiving against an aluminum reflector at 1.5 cm distance. The element in receive detected a 0.2 mV pre-amplified signal for a driving frequency of 9.5 MHz. Characterization with a hydrophone evaluated a sound pressure output of these devices at 33 kPa and a -6dB bandwidth at 32%.

PZT film development processing on unusual substrates was expanded through integrating thin-film PZT actuators on curved glass mirror segments for deterministic figure correction using the converse piezoelectric effect. Crystallization conditions, photolithography procedures and anisotropic conductive film (ACF) bonding were reinvented to accommodate the use of the unconventional substrate.

Two generations of X-ray mirror prototypes are reported: a cylindrical optic (HFDFC3) with 112 actuator cells and a pseudo-conical piece (C1S04) with 288 actuator cells routed through an insulation layer using two-level metallization.

Absolute figure correction could not be achieved for HFDFC3 due to processing-related impact being outside of the actuator dynamic range. However, it provided empirical influence function data that, through finite element analysis simulations, proved the feasibility of figure correction by the integrated PZT actuators.

C1S04 resulted in a 15% low yield upon fabrication. A rework process was developed to remove the top-level metallization and the insulation layer to assess the failure mechanism. Most of the shorted PZT actuator cells were repaired by a novel defect-burnout approach that used a combination of pogo pins, current-voltage characteristic measurements, and laser-cutting to vaporize the conductive filaments. The final yield was improved to 99%.

Table of Contents

List of Figures

List of Tables

Acknowledgement

First and foremost, I would like to express my deepest gratitude for the guidance and support of my thesis advisors, Dr. Thomas Jackson and Dr. Susan Trolier-McKinstry. Being taken on by two of the most knowledgeable world-class professors in the engineering and science field has been the most fortunate thing that happened to me during my time at Penn State. They taught me how to think and work at problems from the perspective of both a device engineer and a materials scientist. Without their tremendous patience and commitment to mentoring, I would not have become the independent researcher that I am today.

My gratitude is further extended to my first advisor Dr. Kenji Uchino for giving me the opportunity to further my study at Penn State as a graduate student, helping me through the transition, and introducing the world of piezoelectrics to me. I would also like to thank my thesis committee members: Dr. Chris Rahn and Dr. Mehdi Kiani, for the care and time in reviewing and guiding this doctoral thesis.

This work has also been made possible by a large group of colleagues and friends. First, I would like to thank all of the past and present members of the Jackson and Trolier-McKinstry research groups: Sora, Sang, Mohit, Alex, Quyen, Betul, Ryan, Lyndsey, Nathan, Nicole, Jung In, Song Won, Veronika, Smitha, Carl, Chris, Mike, Leonard, Travis, and Pannawit. A special thank you to Akanksha Gupta for connecting me with the Jackson research group at the very beginning and generously demonstrating experiments to me even before I was accepted to the team. I would also like to deliver a special thank you to Dr. Margeaux Wallace, Dr. Hong Goo Yeo, Dr. Haoyu Li and Dr. Yiyang Gong for giving me extensive training in device processing and equipment maintenance, and to Dr. Wanlin Zhu, Dr. Julian Walker, and Dr. Dixiong Wang for their constant support both professionally and personally. I would like to expressive a very special thank you to Kathleen Coleman; she has helped me tremendously at work and also in life. Besides the two research groups

that I am part of, I would also like to extend my gratitude to Dr. Noel Giebink's students and scholars; I am very thankful for all the tool/equipment exchange and fun social gatherings with them. I am especially thankful for Alyssa Brigeman and Jared Price for all the wonderful experiences in and outside EE West.

The collaborations at Penn State are gratefully acknowledged. In particular, I would like to thank Dr. Ajay Dangi and Dr. Raj Kothapalli for imparting me their knowledge and guidance in the underwater acoustic testing for the flexible transducers. I am also grateful for the opportunity of working on the fingervein sensor team; Dr. Kyusun Choi and Dr. Jeong Nyeon Kim were elemental in expanding my research directions and resources. Outside of Penn State, I would like to extend my gratitude to Smithsonian Astrophysical Observatory for the discussions and collaborations. In addition, my time at Penn State could not have been as fruitful without the help of the staff of the MRI Nanofab and MCL; I have learned many useful skills from Beth, Guy, Bill Drawl, Bill Mahoney, Mike, Kathy, Andy, Bangzhi, Ted, Shane, Chad, Gino, Manuel, Maria, and Jeff. I am also grateful for having the help from the MSC and EE finance and secretarial staff: SherryDawn, Erin, Alyshia, Sandie, and Jaime.

Finally, I would like to thank my parents for their unconditional love and encouragement in my life. Words cannot sufficiently express how much their support means to me.

This work was supported by: (1) National Science Foundation (NSF) grant number IIP-1547877 as part of I/UCRC Clusters for Grand Challenges: Center for Tire Research, (2) MTEC Global Co., Ltd., and (3) National Aeronautics and Space Administration (NASA).

Chapter 1. Introduction and Background

1.1 Introduction and thesis organization

Piezoelectrics are a family of materials that can realize the conversion between mechanical and electrical energy. When a mechanical stress is applied to a piezoelectric material, electrical charges are generated; this describes the direct piezoelectric effect. For the converse piezoelectric effect, the electrical energy is converted to the mechanical energy as strain is induced under an applied electric field. Piezoelectrics exist in a variety of formats, including polycrystalline ceramics, single crystals, piezoelectric polymers, and piezoelectric films. The applications also cover a broad spectrum of fields, such as sensors, actuators, transducers, transformers, and ultrasonic motors.

While bulk materials dominate the market for macro-scaled, high-power and high-voltage applications, such as underwater sonars [1-3], medical imaging transducers [4-6], and fuel injection systems [7-9], thin-film piezoelectrics enabled the development of miniaturized devices that can achieve higher mechanical precision, higher sensitivity, lower power consumption, and lower driving voltages that are compatible with complementary metal-oxide-semiconductor (CMOS) circuitry. Piezoelectric thin films are the core of piezoelectric microelectromechanical systems (piezoMEMS) development in applications such as piezoelectric micromachined ultrasonic transducers (pMUTs) [10-13], micropumps [13], energy harvesters [14, 15], and actuators [16, 17].

Initial piezoMEMS development mainly revolved around ZnO and AlN films because of their low thermal budget for deposition and the integration compatibility with silicon technology. Thin film $Pb(Zr_{1-x}, Ti_x)O_3$ (PZT) possesses piezoelectric responses that are two orders of magnitude higher, was delayed in the development process for piezoMEMS due to integration difficulties [18]. To achieve a dense structure and good properties, thin film PZT requires a minimum crystallization temperature of about 600°C [19]. At such high temperatures, integration faces challenges of interdiffusion and/or stress failure-associated delamination due to thermal expansion coefficient mismatch [18]. Despite the challenges and difficulties, PZT films have been studied extensively over the past two to three decades;

deeper understanding and significant advancements have been achieved in processing, characterization, and device integration.

Beyond thin film piezoMEMS is the next-generation of flexible piezoelectric systems that conform to objects with complex geometries and surface structures. Applications unachievable by conventional rigid substrate-based devices can be realized by bendable, stretchable, and foldable counterparts. Various flexible piezoelectric devices and systems have been demonstrated for applications as sensors, actuators, energy harvesters, etc.; prior reports in this field are reviewed below in detail.

Historically, flexible piezoelectric systems were predominantly based on polymeric piezoelectrics, such as polyvinylidene fluoride (PVDF) [20-23] and odd-numbered nylons (e.g., nylon-5, nylon-7, nylon-11) [24]. Despite their flexibility, the effectiveness of these materials is limited by low piezoelectric response and low operating temperature.

As an alternative, inorganic piezoelectric thin films can be integrated with metallic foils or polymeric substrates for improved electromechanical responses while realizing mechanical flexibility. Table 1-1 lists selected material properties of PVDF and three important inorganic piezoelectric thin films as candidates for flexible integration. Considering the fact that many of the inorganic materials require a crystallization temperature (e.g., PZT, PMN-PT, $BaTiO_3$) substantially higher than the thermal limit of nearly all polymeric materials, thermally robust metallic foils naturally become convenient choices for direct deposition. Nickel and stainless-steel foils have been reported as flexible substrates for PZT based MEMS devices due to their high mechanical and thermal robustness [25-29].

Table 5-1. Properties of selected thin-film piezoelectric materials for flexible device consideration.

	Thin Film PZT	**Thin Film ZnO**	**Thin Film AlN**	**PVDF**
$e_{31,f}$	-10 [30]	-0.8 [33]	-1.02 [37]	-
$d_{33,(f)}$ (pC/N)	120-130 [31]	10-12 [34]	3.4 [37]	-33 [39]
Relative Permittivity	1200 [32]	11 [35]	11 [37]	5 [40]
Crystallization Temp.	>600°C [16]	200°C [36]	250°C [38]	250 – 270°C [41]

Despite being thermally robust and mechanically ductile, metal foils are stiffer than polymers; some may require a buffer layer for insulation and/or passivation while some can be cost-prohibitive (e.g., Pt). Using polymer as the flexible substrate can therefore provide advantages to MEMS applications. Piezoelectric actuators on a compliant elastic layer undergo larger displacement for the same applied voltage. In the energy harvesting arena, the lower elastic stiffness produces lower resonance frequencies which provide a better frequency match to ambient vibrations. In terms of the feasibility of direct deposition on polymer, materials like AlN and ZnO films are convenient candidates as they can be grown at low temperature levels (200-250°C [36, 38]) below the glass transition or the decomposition temperature of many thermoplastic polymer materials. AlN and ZnO thin-film based flexible sensors and transducers have been demonstrated on polyimide and polyethylene terepthalate (PET) substrates via direct deposition methods [42-45].

However, the low piezoelectric coefficients of AlN and ZnO make them unsuitable for high sensitivity and large actuation applications. Materials with large piezoelectric properties, such as PZT and PMN-PT are otherwise preferred if there is a robust way to integrate them with polymeric substrates.

Several reports have demonstrated low temperature annealing for PZT films. Crystallization temperatures below 500°C were achieved using laser-assisted localized heating [46-48]. Alternatively, deposition of PZT nanostructures was realized on polyimide substrates using a heated AFM tip [49]. Besides localized heating, a crystallization temperature of 300-400°C was achieved for PZT films by adding crystalline nano-seeds (nanometric PZT powder) in the solution combined with UV-assisted heat treatment [50, 51], as the addition of the nano-seeds in the precursor lowered the activation energy for nucleation. While it is in principle possible to utilize these methods to achieve PZT crystallization on polymers, in practice the resulting films are generally limited in size, density, and/or functional properties.

As an alternative to direct deposition, the PZT layer can be grown on a thermally robust substrate and then transferred onto a polymeric layer. Transfer has been realized via various methods. Qi *et al*. reported a process to transfer PZT nanoribbons from the original growth substrate, MgO, to polydimethylsiloxane (PDMS) through wet etching of MgO in hot phosphoric acid [53]. As phosphoric

acid attacks PZT, small release area shortens the acid exposure time, thus minimizing the etch-induced damage. Thin-film PZT release onto PET substrates has been demonstrated using a laser lift-off technique. An excimer laser incident through a sapphire substrate melts and/or thermally shocks the interface between the PZT and the substrate, thus facilitating the separation [53, 54]. As the released area is governed by the laser beam spot size, the low throughput characteristic makes large area release difficult.

Amid the application-driven ardor for realizing flexible piezoelectric devices, an important opportunity space has been overlooked by the piezoelectric community. The approaches that enable stretchable, bendable, and conformal systems can also provide new insights into the fully-released state of thin film piezoelectrics. Films grown on rigid substrates experience a clamping effect, which, in combination with the large stress associated with film growth, contributes to reduced domain wall motion and inferior piezoelectric and dielectric properties with respect to their bulk counterparts [55-57]. Integration with polymeric substrates facilitates the investigation of material properties of piezoelectric films in the fully released state, as the applied stress from the surrounding inactive material and the substrate can be simultaneously removed. Thus, the material properties of films on polymeric substrates are expected to approach the values of bulk ceramics of the same composition.

If superior material properties result from putting inorganic piezoelectrics on polymer, mechanical flexibility is not the only advantage of integration with polymeric substrates. This, of course, necessitates that no damage is induced in the active components during the integration process.

Breaking the rules, this dissertation integrates 700°C-crystallized PZT films with polyimide substrates over large areas through a sacrificial-layer-release approach that causes no damage to any layers in the sample stack and makes no compromises on material properties. Flexible ultrasonic transducers were developed building upon the release method. The correlation between improved domain wall motion and reduced substrate-clamping was confirmed empirically. In other words, the integration process presented in this dissertation aims at advancements in the development of thin film piezoelectrics not only through adding flexibility as a form factor, but also by enabling a platform for studying material

responses in the released state and providing a means to enhance material responses and device performances.

Chapter 2 demonstrates the release process that transfers large-area blanket PZT films from Si to solution-cast polyimide through dissolution of an underlying ZnO release layer. The processing details, including the selection and the function of the release layer, etchant, diffusion barrier, and photoresists to yield a damage-free, cost-effective process are described. The electrical properties of PZT films were compared before and after release; the data confirmed the correlation between improved domain wall mobility and substrate declamping.

Chapter 3 describes the development of thin film PZT based-flexible ultrasonic transducers on polyimide layers incorporating the release technique. New processing steps were added to pattern the PZT layer, establish external electrical connections, and waterproof the devices. The fabricated transducers demonstrated pitch-catch testing and the achievable sound pressure level generated by a single resonator element was evaluated.

Chapter 4 describes attempts to measure the correct longitudinal piezoelectric coefficient, d_{33}, in released PZT films on polyimide substrates using a commercial double-beam laser interferometer (DBLI). Inflated displacements and implausibly large d_{33} results were measured, which led to the identification of a major artifact in the data. Detailed discussion on the possible cause of this artifact is presented, followed by a proposed setup to reduce its impact on the resulting data.

Chapter 5 continues the approach towards *breaking the rules* by exploring thin film PZT integration with a different type of unconventional substrate – 0.4 mm thick curved borosilicate glass for piezoelectrically adjustable X-ray mirror segments. Challenges in deposition, photolithography, electrical connections, stress-balancing, rework, and repair of shorted devices were addressed.

Chapter 6 concludes the discussion of thin film PZT development on two of the unconventional substrates and provides suggestions for future work – where *breaking the rules* can be extended to integrating piezoelectrics with a system or a whole realm of technology that is previously inaccessible.

1.2 Background of piezoelectrics and ferroelectrics

PZT is piezoelectric. Piezoelectrics are a family of materials that can realize the conversion between mechanical and electrical energy. When a mechanical stress is applied to a piezoelectric material, electrical charges are generated; this describes the direct piezoelectric effect. For the converse piezoelectric effect, the electrical energy is converted to the mechanical energy as strain is induced with an applied electric field. The direct and the converse piezoelectric effect are described by Equation 1-1 and 1-2, respectively, in a tensor format. The proportionality constant d_{ijk} (or d_{kij}) that links the coupling is the piezoelectric coefficient [58]. The coefficient values are numerically identical for both cases for mechanically free boundary conditions.

$$D_i = d_{ijk} T_{jk} \tag{1-1}$$

$$x_{ij} = d_{kij} E_k \tag{1-2}$$

In Equation 1-1 and 1-2, *i*, *j*, and *k* =1,2,3, *D* is the dielectric displacement (charge per unit area), *T* is the stress, *x* is the strain, and *E* is the electric field.

Perovskite structure and composition

PZT crystallizes in the perovskite structure with the ABO_3 chemical formula. As schematically shown in Figure 1-1 (a), this structure is a cubic unit cell at an elevated temperature with oxygens (O) in the face centers, a large cation (A) on the corners, and a smaller cation (B) in the body center [58]. For PZT, the large cation is Pb^{2+} and the smaller cation is either Zr^{4+} or Ti^{4+}.

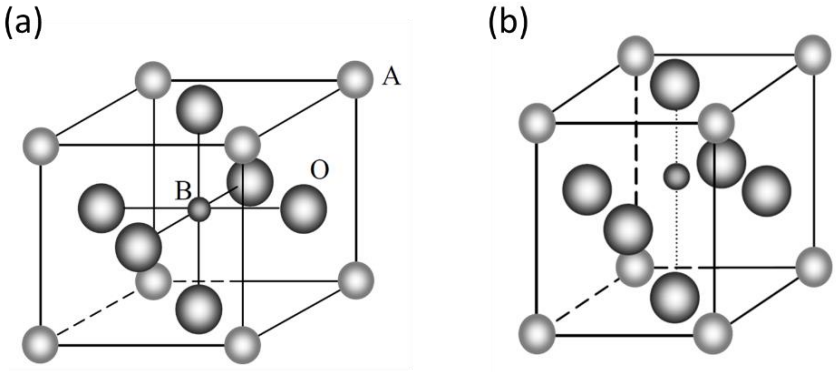

Figure 5-1. Schematic of a perovskite unit cell in (a) cubic phase, and (b) tetragonal phase. Image adapted from Gharb *et al*. [59].

Cooling through a temperature known as the Curie temperature T_c, the cubic structure elongates in the <100> direction as the B site cation (e.g., Zr^{4+} or Ti^{4+} for PZT) shifts towards one of the oxygens. The Curie temperature is 320°C-375°C for both PZT bulk ceramics and thin-films [60-62]. The displacement of the center ion results in a spontaneous polarization.

PZT is the solid solution of $PbZrO_3$ and $PbTiO_3$; the associated phase diagram is shown in Figure 1-2. The resulting structure distortion of PZT upon cooling through T_c depends on the composition ratio of Zr/Ti.

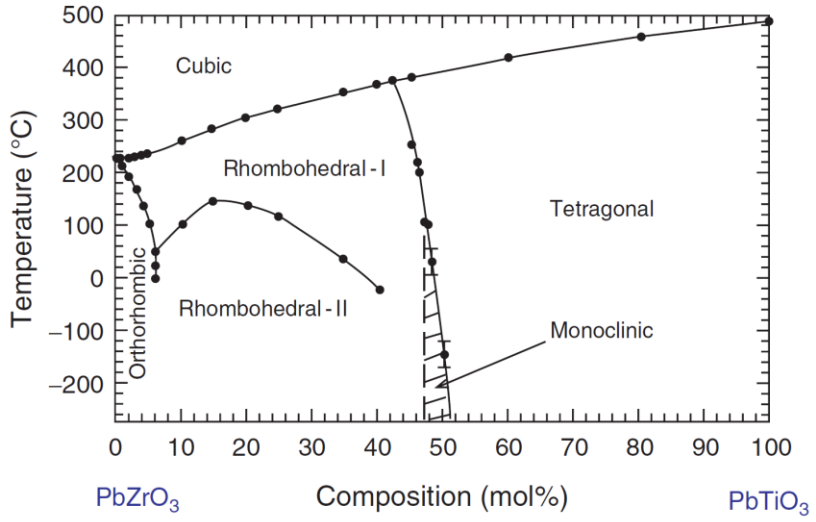

Figure 5-2. Phase diagram of solid solution $PbZr_{1-x}Ti_xO_3$ system. Image modified from Alberta *et al*. [63].

For Ti concentration larger than 48%, PZT adopts a tetragonally distorted ferroelectric phase and for Ti concentration less than 48%, a rhombohedral phase is formed. The morphotropic phase boundary (MPB) is where the two phases meet, which occurs at a Zr/Ti ratio of approximately 52/48. A monoclinic phase also exists near the MPB at low temperatures. The composition at the MPB is important for PZT device development as it is where the highest coupling factor and dielectric permittivity occur due to enhanced polarizability and degree of alignment during poling [64, 65].

Ferroelectricity of PZT

A ferroelectric is a material that possesses a spontaneous polarization switchable between crystallographically defined states with the application of a sufficient electric field over some temperature range [66]. All ferroelectrics are piezoelectric, but not vice versa. PZT is ferroelectric.

Each region containing the same, or nearly the same spontaneous polarization direction is defined as a domain. Domains are formed in PZT and all other ferroelectrics upon cooling through T_c as a way to minimize the electrostatic and elastic energy [67]. The directions of the domains tend to be random, which leads to zero net polarizations in the system. Separating the domains are the domain walls, which are described by the angle between the dipoles. There are typically 180° and non-180° domain walls. The 180° walls can only be switched by electric fields while the non-180° walls can be switched by mechanical excitations as well as electrical fields. The ferroelectricity disappears above the Curie temperature T_c, where the material becomes paraelectric [68].

A signature feature of ferroelectric materials is the polarization-electric field (P-E) hysteresis loop. Figure 1-3 shows a typical P-E loop for an appropriately oriented single crystal and schematically describes the corresponding domain states for a few important points.

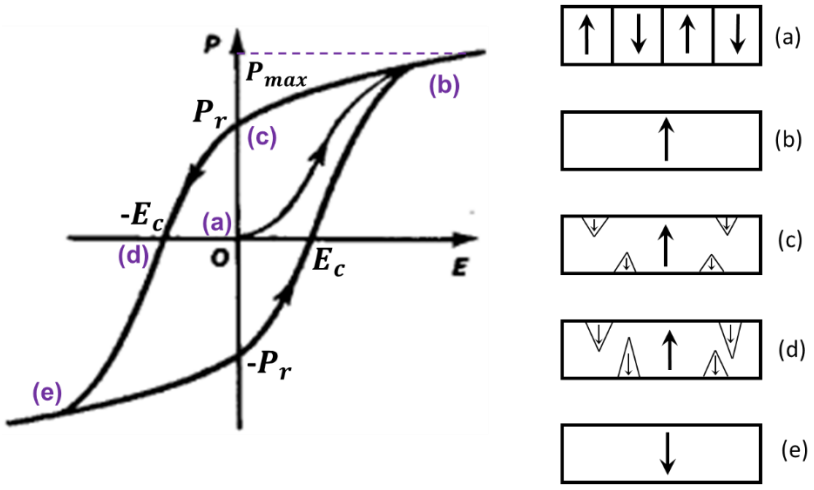

Figure 5-3. Polarization-electric field (P-E) hysteresis loop of an appropriately oriented single crystal. Figure adapted from [66].

Beginning from the origin of the coordinates at point (a), before the material sees any electric field, there is zero net polarization. When an electric field is applied, the polarization begins to align with the field and eventually merges into a single domain (for an appropriately oriented single crystal). Above that field, the polarization continues to rise due to electronic and ionic polarizability; at the maximum electric field at point (b), the P-E loop reaches the maximum polarization P_{max}. As the positive electric field decreases in magnitude, some small nuclei of domains with reversed polarization direction typically appear. When the field reaches zero at point (c), the polarization remaining is known as the remanent polarization P_r. In an ideal ferroelectric single crystal system, P_r should be almost identical to the spontaneous polarization P_s, but back switching causes reversal in a fraction of the polarizations, resulting in a lower P_r [69]. Subsequently, small nuclei of domains with the reverse polarization direction continue to grow as the electric field increases with the opposite polarity. The net polarization becomes zero at an electric field known as the coercive field, E_c, beyond which, the polarization continues to switch in the opposite direction and reaches the negative P_{max} at point (e).

The shape of the P-E hysteresis loop is frequency dependent. For PZT films in this work, 100 Hz is typically used for the characterization.

Poling

Most as-grown ferroelectrics, including PZT films, have randomly oriented domain states; the net piezoelectric responses is therefore near zero. In order to produce a net piezoelectric coefficient, the materials are poled with a strong DC electric field to align the dipoles [70]. When the electric field is removed, without stress- or strain-induced restoring forces, most dipoles remain aligned as well as possible along the poling direction. Some of the domain walls are removed on poling. The poling field used for a thin-film PZT system is usually 2-5 times the coercive field, and the field is applied for relatively long times (e.g., 15 minutes) [12][26][30][32]. High temperature (100-150°C) poling is often employed to produce more stable polarization states [71]. De-poling can occur when the material is subject to either a temperature above the Curie temperature, or a strong electric field in the opposite direction of the poling field, or a strong mechanical stress [72].

1.3 Chapter references

[1] E. Sun, and W. Cao, "Relaxor-based ferroelectric single crystals: Growth, domain engineering, characterization and applications," *Progress in Materials Science,* vol. 65, pp. 124-210, 2014

[2] S. Zhang, F. Li, X. Jiang, J. Kim, J. Luo, and X. Geng, "Advantages and challenges of relaxor-$PbTiO_3$ ferroelectric crystals for electroacoustic transducers – A review," *Progress in Materials Science*, vol. 68, pp. 1-66, 2015

[3] D. F. Waechter, S. E. Prasad, R. G. Blacow, and B. Yan, "Internally biased PZT materials for high-power sonar transducers," in *Proceedings of the 11th CF/DRDC International Meeting on Naval Applications of Materials Technology*, Dartmouth, Nova Scotia, Canada, June, 2005, pp. 223-232

[4] C. Liu, Q. Zhou, F. T. Djuth and K. K. Shung, "High-frequency (>50 MHz) medical ultrasound linear arrays fabricated from micromachined bulk PZT materials," in *IEEE Trans. Ultrason., Ferroelectr., Freq. Contr.*, vol. 59, no. 2, pp. 315-318, 2012

[5] K. K. Shung, J. M. Cannata, and Q. F. Zhou, "Piezoelectric materials for high frequency medical imaging applications A review," *J Electroceram*, vol. 19, pp.141–147, 2007

[6] T. Ritter, T. R. Shrout, R. Tutwiler, and K. K. Shung, "A 30-MHz piezo-composite ultrasound array for medical imaging applications," *IEEE Trans. Ultrason. Ferroelectr. Freq. Contr.*, vol. 49, no. 2, pp. 217–230, 2002

[7] R. Payri, R., J. Gimeno, J. P. Viera, and A. H. Plazas, "Needle lift profile influence on the vapor phase penetration for a prototype diesel direct acting piezoelectric injector," *Fuel*, vol. 113, pp. 257-265, 2013

[8] U. Augustin, "Piezoelectric injector for fuel-injection systems of internal combustion engines." U.S. Patent No. 6,085,990. 11 Jul. 2000.

[9] H. Wang, T. Matsunaga, and H-T Lin. "Characterization of poled single-layer PZT for piezo stack in fuel injection system," *Ceramic Engineering and Science Proceedings*, vol. 31, no. 2, American Ceramic Society, Inc., 2010, pp. 127-130

[10] S. Akhbari, F. Sammoura, S. Shelton, C. Yang, D. Horsley, and L. Lin, "Highly responsive curved aluminum nitride pMUT," In *27th International Conference on Micro Electro Mechanical Systems (MEMS)*, 2014, IEEE, pp. 124-127

[11] X. Jiang, H-Y. Tang, Y. Lu, E. J. Ng, J. M. Tsai, B. E. Boser, and D. A. Horsley, "Ultrasonic fingerprint sensor with transmit beamforming based on a PMUT array bonded to CMOS circuitry*," IEEE Trans. Ultrason., Ferroelectr., Freq. Contr.*, vol. 64, no. 9, pp. 1401-1408, 2017

[12] C. Y. Cheng, A. Dangi, L. Ren, S. Tiwari, R. R. Benoit, Y. Qiu, H. S. Lay, S. Agrawal, R. Pratap, S-R. Kothapalli, T. E. Mallouk, S. Cochran, and S. Trolier-McKinstry, "Thin film PZT-based PMUT arrays for deterministic particle manipulation," *IEEE Trans. Ultrason., Ferroelectr., Freq. Contr.*, vol. 66, no. 10, pp. 1606-1615, 2019

[13] N. Nguyen, X. Huang, and T. K. Chuan, "MEMS-micropumps: a review," *J. Fluids Eng.*, vol. 124, pp. 384–392, 2002.

[14] T. Xue, H. G. Yeo, S. Trolier-McKinstry, S. Roundy, "A wrist-worn rotational energy harvester utilizing magnetically plucked {001} oriented bimorph PZT thin-film beams," in *IEEE 19th International Conference on Solid-State Sensors, Actuators and Microsystems (Transducers)*, June 2017, pp. 375-378

[15] P. Wang, and H. Du, "ZnO thin film piezoelectric MEMS vibration energy harvesters with two piezoelectric elements for higher output performance," *Review of Scientific Instruments*, vol. 86, no. 7, pp. 075002, 2015

[16] S. Watanabe, M. Suzuki, and T. Fujiu, "Application of PZT thin film displacement sensors for atomic force microscopy," *J. Vac. Sci. Technol. B.*, vol. 13, p. 1119, 1995

[17] P. Lugienbuhl, G. A. Racine, P. Lerch, B. Romanowicz, K. G. Brookes, N. F. De Rooij, P. Renaud, and N. Setter, "Piezoelectric cantilever beams actuated by PZT sol-gel thin films," *Sensors and Actuators A: Physical*, vol. 54, no. 1-3, pp. 530-535, 1996

[18] P. Muralt, "Piezoelectric thin films for MEMS," *Integrated Ferroelectrics*, vol. 17, pp. 297-307, 1997

[19] K. D. Budd, S. K. Dey, and D. A. Payne, "Sol-gel processing of $PbTiO_3$, $PbZrO_3$, PZT, and PLZT thin films," *Brit. Ceram. Proc.*, vol. 36, pp.107-121, 1985

[20] Y. Kato, T. Sekitani, Y. Noguchi, T. Yokota, M. Takamiya, T. Sakurai, and T. Someya, "Large-area flexible ultrasonic imaging system with an organic transistor active matrix," *IEEE Transactions on Electron Devices*, vol. 57, no. 5, pp. 995-1002, 2010.

[21] L. F. Brown and J. L. Mason, "Disposable PVDF ultrasonic transducers for non-destructive testing applications," *IEEE Trans. Ultrason., Ferroelectr., Freq. Contr.*, vol. 43, no. 4, pp. 560–568, 1996.

[22] A. Ambrosy and K. Holdik, "Piezoelectric PVDF films as ultrasonic transducers," *J. Phys. E: Sci. Instrum.* vol.17, no. 10, pp.856-859, 1984

[23] M. D. Sherar and F. S. Foster, "The design and fabrication of high frequency poly(vinyldene fluoride) transducers," *Ultrason. Imag.*, vol. 11, pp. 75-94, 1989.

[24] L. F. Brown, J. L. Mason, D. Khataniar, J. I. Scheinbeim, and B. A. Newman, "Ferroelectric Nylon-7, -11 Ultrasonic Transducer Performance," in *10th International Symposium on Applications of Ferroelectrics (ISAF), IEEE*, 1996, vol. 2, pp.1255-1258,

[25] M. Losego, L. Jimison, J. Ihlefeld and J. Maria, "Ferroelectric response from lead zirconate titanate thin films prepared directly on low-resistivity copper substrates," *Appl. Phys. Lett.*, vol. 86, pp. 1, 2005.

[26] H. Yeo and S. Trolier-McKinstry, "{001} Oriented piezoelectric films prepared by chemical solution deposition on Ni foils," *J. Appl. Phys.*, vol. 116, pp. 14105, 2014.

[27] A. Kingon and S. Srinivasan, "Lead zirconate titanate thin films directly on copper electrodes for ferroelectric, dielectric and piezoelectric applications," *Nat. Mater, vol.* vol. 4, pp. 233-237, 2005.

[28] J. Cheng, W. Zhu, N. Li and L. Cross, "Electrical properties of sol-gel-derived $Pb(Zr_{0.52}Ti_{0.48})O_3$ thin films on a $PbTiO_3$-coated stainless steel substrate," *Appl. Phys. Lett.*, vol. 81, pp. 4805-4807, 2003.

[29] T. Suzuki, I. Kanno, J. Loverich, H. Kotera and K. Wasa, "Characterization of Pb (Zr, Ti)O_3 thin films deposited on stainless steel substrates by RF-magnetron sputtering for MEMS applications," *Sensors Actuators, A Phys.*, vol. 125, pp. 382-386, 2006.

[30] J. F. Shepard, P. J. Moses, and S. Trolier-McKinstry, "The wafer flexure technique for the determination of the transverse piezoelectric coefficient of PZT thin films," *Sens. Actuators A*, vol. 71, pp. 133-138, 1998

[31] V. Kovacova, N. Vaxelaire, G. Le Rhun, P. Gergaud, T. Schmitz-Kempen, and E. Defay, "Correlation between electric field induced phase transition and piezoelectricity in PZT films," *Physical Review B*, vol. 90, pp. 140101R, 2014

[32] T. Liu, M. Wallace, S. Trolier-McKinstry and T. N. Jackson, "High-temperature crystallized thin-film PZT on thin polyimide substrates," *J. Appl. Phys.*, vol. 122, pp. 164103, 2017.

[33] J. G. E. Gardeniers, Z. M. Rittersma, and G. J. Burger, "Preferred orientation and piezoelectricity in sputtered ZnO films," *J. Appl. Phys.*, vol. 83, pp. 7844-7854, 1998

[34] T. P. Alexander, T. J. Bukowski, D. R. Uhlmann, G. Toewee, K. C. McCarthy, J. Dawley, and B. J. J. Zelinski, "Dielectric properties of sol-gel derived ZnO thin films," in *ISAF '96. Proceedings of the Tenth IEEE International Symposium on Applications of Ferroelectrics*, East Brunswick, NJ, USA, 1996, vol. 2, pp. 585-588

[35] P. Muralt, "PZT thin films for microsensors and actuators: Where do we stand?" *IEEE Trans. Ultrason., Ferroelect., Freq. Contr.*, vol. 47, pp. 297-307, 1997

[36] J. Sun, D. A. Mourey, D. Zhao, and T. N. Jackson, "ZnO thin film, device, and circuit fabrication using low-temperature PECVD processes," *Journal of Electronic Materials*, vol. 37, no. 5, pp. 755-759, 2008

[37] M-A. Dubois, and P. Muralt, "Measurement of the effective transverse piezoelectric coefficient $e_{31,f}$ of AlN and $Pb(Zr_x, Ti_{1-x})O_3$ thin films," *Sensors and Actuators*, vol. 77, pp. 106-112, 1998

[38] J-B. Lee, D-H. Cho, D-Y. Kim, C-K. Park, and J-S. Park, "Relationships between material properties of piezo-electric thin films and device characteristics of film bulk acoustic resonators," *Thin Solid Films*, vol. 516, pp. 475-480, 2007

[39] L.F. Brown, "Design considerations for piezoelectric polymer ultrasound transducers," *IEEE Trans. Ultrason., Ferroelectr, Freq., Contr.*, vol. 47, no. 6, pp. 1377-1396, 2000

[40] L. F. Brown, J. L. Mason, M. L. Klinkenborg, J. I. Scheinbeim, and B. A. Newman, "Ferroelectric nylon materials and their feasibility for ultrasound transducers," *IEEE Trans. Ultrason., Ferroelect., Freq. Contr.*, vol. 44, no. 5, pp. 1049–1059, 1997

[41] K. Koga, and H. Ohigashi, "Piezoelectricity and related properties of vinylidene fluoride and trifluoroethylene copolymers," *J. Appl. Phys*. vol. 59, pp. 2142-2150, 1986

[42] M. Akiyama, Y. Morofuji, T. Kamohara, K. Nishikubo, M. Tsubai, O. Fukuda, and N. Ueno, "Flexible piezoelectric pressure sensors using oriented aluminum nitride thin films prepared on polyethylene terephthalate films," *J. Appl. Phys*., vol. 100, pp. 114318, 2006

[43] N. Jackson, L. Keeney, and Alan Mathewson, "Flexible-CMOS and biocompatible piezoelectric AlN material for MEMS applications," *Smart Mater. Struct*., vol. 22, pp. 115033, 2013

[44] S. Petroni, C. La Tegola, G. Caretto, A. Campa, A. Passaseo, M. De Vittorio, and R. Cingolani, "Aluminum nitride piezo-MEMS on polyimide flexible substrates," *Microelectronic Engineering*, vol. 88, pp. 2372-2375, 2011

[45] M. Laurenti, D. Perrone, A. Verna, C. F. Pirri, and A. Chiolerio, "Development of a flexible lead-free piezoelectric transducer for health monitoring in the space environment," *micromachine*s, vol. 6, pp. 1729-1744, 2015

[46] Y. Zhu, J. Zhu, Y. Song and S. B. Desu, "Laser-assisted low temperature processing of Pb(Zr, Ti)O_3 thin film," *Appl. Phys. Lett.*, vol. 73, pp. 1958-1960, 1998.

[47] A. Rajashekhar, A. Fox, S. Bharadwaja and S. Trolier-McKinstry, "In situ laser annealing during growth of $Pb(Zr_{0.52}Ti_{0.48})O_3$ thin films," *Appl. Phys. Lett*., vol. 103, pp. 32908, 2013.

[48] H-C. Pan, C-C. Chou, and H-L. Tsai, "Low-temperature processing of sol-gel derived $La_{0.5}Ti_{0.48}O_3$ films using CO_2 laser annealing," *Appl. Phys. Lett*., vol. 83, pp. 3156-3158, 2003

[49] S. Kim, Y. Bastani, H. Lu, W. King, S. Marder, K. Sandhage, A. Gruverman, E. Riedo and N. Bassiri-Gharb, "Direct fabrication of arbitrary-shaped ferroelectric nanostructures on plastic, glass, and silicon substrates," *Adv. Mater*., vol. 23, pp. 3786-3790, 2011.

[50] A. Wu, P. M. Vilarinho, I. Reaney, and I. M. Miranda Salvado, "Early stages of crystallization of sol-gel-derived lead zirconate titanate thin films," *Chem. Mater*., vol. 15, pp. 1147-1155, 2003

[51] I. Bretos, R. Jimenez, A. Wu, A. I. Kingon, P. M. Vilarinho, and M. L. Calzada, "Activated solutions enabling low-temperature processing of functional ferroelectric oxides for flexible electronics," *Adv. Mater*., vol. 26, pp. 1405-1409, 2014

[52] Y. Qi, N. Jafferis, K. Lyons, C. Lee, H. Ahmad and M. McAlpine, "Piezoelectric ribbons printed onto rubber for flexible energy conversion," *Nano Lett*., vol. 10, pp. 524, 2010.

[53] Y. Do, W. S. Jung, M. Kang, C. Kang and S. Yoon, "Preparation on transparent flexible piezoelectric energy harvester based on PZT films by laser lift-off process," *Sensors Actuators, A Phys*., vol. 200, pp. 51-55, 2013.

[54] K-I. Park, J. H. Son, G-T. Hwang, C. K. Jeong, J. Ryu, M. Koo, I. Choi, S. H. Lee, M. Byun, Z. L. Wang, and K. J. Lee, "Highly-efficient, flexible piezoelectric PZT thin film nanogenerator on plastic substrates," *Adv. Mater.*, vol. 26, pp. 2514-2520, 2014

[55] F. Xu, S. Trolier-McKinstry, W. Ren, B. Xu, Z. Xie and K. Hemker, "Domain wall motion and its contribution to the dielectric and piezoelectric properties of lead zirconate titanate films," *J. Appl. Phys.*, vol. 89, pp. 1336, 2001.

[56] M. Wallace, R. Johnson-Wilke, G. Esteves, C. Fancher, R. Wilke, J. Jones and S. Trolier-McKinstry, "In situ measurement of increased ferroelectric/ferroelastic domain wall motion in declamped tetragonal lead zirconate titanate thin films," *J. Appl. Phys.*, vol. 117, pp. 54103, 2015.

[57] F. Griggio, S. Jesse, A. Kumar, O. Ovchinnikov, H. Kim, T. Jackson, D. Damjanovic, S. V. Kalinin and S. Trolier-McKinstry, "Substrate clamping effects on irreversible domain wall dynamics in lead zirconate titanate thin films," *Phys. Rev. Lett.*, vol. 108, pp. 157604(1-5), 2012.

[58] B. Jaffe, W. R. Cook Jr., and H. Jaffe, *Piezoelectric Ceramics*, Academic Press London and New York, 1971

[59] N. B. Gharb, "Dielectric and piezoelectric nonlinearities in oriented $Pb(Yb_{1/2}Nb_{1/2})O_3$ thin films," Ph.D. dissertation, Department of Materials Science and Engineering, p. 19, Pennsylvania State University, University Park, PA, U.S.A, 2005

[60] R. Bruchhaus, D. Pitzer, R. Primig, M. Schreiter, W. Wersing, "PZT thin films grown by multi-target sputtering: analysis of thin film stress," *Integrated Ferroelectrics*, vol. 21, no. 1-4, pp. 461-467, 1998

[61] A. Okada, "Some electrical and optical properties of ferroelectric lead-zirconate-lead-titanate thin films," *J. Appl. Phys.*, vol. 48, no. 7, pp. 2905-2909, 1977

[62] *Piezoelectric Ceramics Principles and Applications*, 2nd ed., APC International, Ltd., Mackeyville, PA, USA, 2014, p. 32.

[63] E. F. Alberta, R. Guo, and A. S. Bhalla, "Structure–property diagrams of ferroic solid solutions. Part I: Perovskite relaxor ferroelectrics with morphotropic phase boundaries," *Ferroelectrics Review*, vol. 4, pp. 1-327, 2001

[64] B. Jaffe, R. S. Roth, and S. Marzullo, "Piezoelectric properties of lead zirconate-lead titanate solid-solution ceramics," *J. Appl. Phys.*, vol. 25, pp. 809, 1954

[65] B. Jaffe, R. S. Roth, and S. Marzullo, "Properties of piezoelectric ceramics in the solid-solution," *J. Res. Nat. Bur. Stds.*, vol. 55, pp. 239-254, 1955

[66] An American National Standard IEEE Standard Definitions of Terms Associated with Ferroelectric and Related Materials, *IEEE Trans. Ultras. Ferro. Freq. Control*, vol. 50, pp. 1, 2003

[67] M.E. Lines and A.M. Glass, *Principles and Applications of Ferroelectrics and Related Materials*, Oxford University Press, New York, 1977, pp. 87-101

[68] F. Jona, G. Shirane, *Ferroelectric Crystals*, International Series of Monographs on Solid State Physics. Pergamon Press Inc, Frankfurt, 1962.

[69] D. Damjanovic, "Ferroelectric, dielectric and piezoelectric properties of ferroelectric thin films and ceramics," *Reports Prog. Phys.*, vol. 61 pp.1267–1324, 1998.

[70] S. Trolier-McKinstry, "Crystal chemistry of piezoelectric materials," in *Piezoelectric and Acoustic Materials for Transducer Applications*, A Safari, and E. K. Akdogan Eds. Springer, Boston, MA, 2008, pp. 39-56.

[71] R. G. Polcawich, and S. Trolier-McKinstry, "Piezoelectric and dielectric reliability of lead zirconate titanate thin films," *J. Mater. Res.*, vol. 15, pp. 2505–2513, 2000

[72] K. Franke, H. Huelz, and M. Weihnacht, "Stress-induced depolarization in PZT thin films, measured by means of electric force microscopy," *Surface Science*, vol. 416, pp. 59-67, 1998.

Chapter 2. High temperature crystallized thin-film PZT on 5 µm polyimide substrates

Significant parts of this chapter have already been published in Journal of Applied Physics [1].

2.1. Introduction to PZT films on polymer substrates

Flexible thin-film piezoelectric devices are utilized in conformal sensors, actuators, and energy harvesters; these devices are useful in infrastructure and health monitoring. For example, ultrasound sensing systems installed on natural gas pipelines and nuclear power plants could detect corrosion and damage to pipe joints, elbows, steps, and welds [2]. Kato et al. has demonstrated a large-area PVDF-based ultrasonic imaging system able to detect targets behind thin objects and obtain three-dimensional images [3]. For human use, a flexible imaging system placed on the body would aid assessment of injury for trauma patients under critical conditions. As an example, a conformal Doppler transducer array positioned on the neck could report carotid pulse without requiring a highly trained ultrasound technician [2].

There are several methods that can be considered for flexible piezoelectric devices. Metallic foils can be utilized as flexible substrates for lead zirconate titanate (PZT) based piezoelectric microelectromechanical systems (MEMS) due to their high mechanical and thermal robustness; this in turn enables direct deposition of PZT [4, 5, 6, 7, 8]. Replacing metallic foils with polymeric layers, however, can provide advantages in MEMS applications due to the lower elastic stiffness of the polymer. Piezoelectric actuators on a compliant elastic layer undergo larger displacement for the same applied voltage. In the energy harvesting arena, the lower elastic stiffness produces lower resonance frequencies which provide a better frequency match to ambient vibrations.

Besides the incentives of realizing conformal piezoelectric devices with enhanced properties, thin-film PZT on polymeric substrates should experience less clamping from the substrate. Clamping, in combination with the large stress associated with film growth, contributes to reduced domain wall motion and inferior piezoelectric and dielectric properties with respect to their bulk counterparts [9, 10, 11].

However, integrating piezoelectric materials with polymers is challenging as many inorganic piezoelectrics require higher crystallization temperature than either the glass transition or decomposition temperature of the polymer. Although devices using piezoelectric materials with low processing temperature on polymer have been reported, such as ZnO, AlN, and PVDF [12, 13, 14], their low piezoelectric coefficients are not ideal for high sensitivity or large actuation. Materials with large piezoelectric properties, such as PZT, are otherwise preferred if there is a robust way to integrate them with polymeric substrates.

While it is in principle possible to utilize localized heating to achieve PZT crystallization on polymers, in practice the resulting films are generally limited in size and/or functional properties [15, 16, 17]. As an alternative, the PZT layer can be first grown on a thermally robust substrate and then transferred onto a polymeric layer. This transfer method has been realized via various methods. Qi *et al.* reported a process to transfer PZT nanoribbons from the original growth substrate, MgO, to polydimethylsiloxane (PDMS) through wet-etching of MgO in hot phosphoric acid [18]. Tue *et al.* etched underlying indium zinc oxide layers to transfer PZT films by fine patterning [19]. As phosphoric acid attacks PZT, small release area shortens the acid exposure time, thus minimizing the etch-induced damage. Alternatively, thin-film PZT release has been demonstrated using a laser lift-off technique. A KrF excimer laser incident through a sapphire substrate melts the interface between the PZT and the substrate, thus facilitating the separation [20]. As the released area is governed by the laser beam spot size, low throughput makes large area release difficult.

In this work, blanket high-temperature crystallized PZT thin-films are transferred from silicon to a thin solution-cast polyimide substrate over a relatively large area by dissolving the underlying ZnO sacrificial layer grown between the PZT and Si.

2.2 Fabrication process

ZnO was chosen as the sacrificial layer in this work because of its easy dissolution in weak acids and its compatibility with the PZT fabrication process. From the point of ZnO deposition to its complete dissolution in etchant, no degradation occurred to the PZT or to any other layers in the sample stack. Co-processing PZT with ZnO based electronics has been carried out in various fields such as piezoelectric MEMS energy harvesters [21] and adjustable x-ray optics [22]. Throughout this thesis, denotations of "clamped" and "released" films refer to the PZT films constrained on the original silicon substrate prior to release, and the films after release onto polyimide, respectively. The preparation process for clamped and released samples are illustrated in the flow diagram of Figure 2-1.

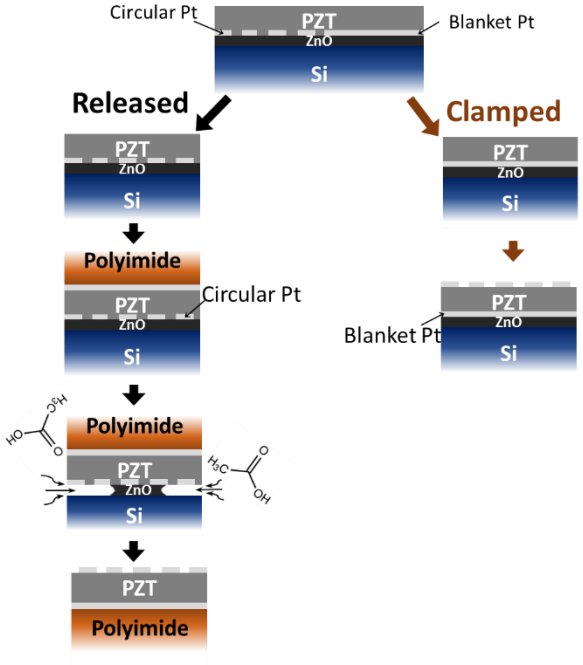

Figure 6-1. The flow chart for preparing released and clamped PZT films from the same deposition. Image reproduced from [1].

A 4 cm × 4 cm silicon substrate with a 1000 Å thermal SiO_2 layer was sonicated in acetone, then rinsed in isopropanol (IPA) and de-ionized (DI) water. The substrate was blown dry with clean air and ashed with an oxygen plasma to remove organic residue. The oxygen plasma ash step was carried out in a customer-modified Plasma Therm (Saint Petersburg, FL, USA) reactive ion etching (RIE) system with

parallel-plate electrode configuration. Theoretically, all commercial parallel-plate RIE systems, such as Plasma Therm 720 at the Penn State Nanofab, should be able to perform such process, and recommended parameters are: 50-100 V substrate bias, 100 mTorr pressure, 100% O_2 gas flow and 60 seconds duration. Over-etching will not cause damage to the silicon oxide nor will it etch the layer. Immediately following the plasma treatment, a 150 nm ZnO layer was deposited by plasma enhanced atomic layer deposition (PEALD) at 200ºC using diethylzinc (DEZ) as the metal organic precursor and N_2O as the oxidant gas. The sacrificial layer was then capped with a 10 nm thick Al_2O_3 barrier layer grown by PEALD in the same system to prevent interdiffusion of lead and zinc during the PZT crystallization step over the sacrificial layer. Trimethylaluminum (TMA) and CO_2 were the organic metal precursor and the oxidant gas for Al_2O_3, respectively. The PEALD system used for both oxide layer deposition was a completely original custom-built tool developed by Prof. Thomas N. Jackson's research group; a description can be found in [23]. Theoretically, any commercial systems (e.g., Kurt J Lesker 150 LE) equipped with TMA and DEZ, and appropriate oxidant should be able to deposit ZnO and Al_2O_3 to serve as the sacrificial layer and diffusion barrier. No released samples, however, have been made with any commercial (PE)ALD systems yet.

After PEALD growth of ZnO and Al_2O_3, 100 – 200 nm thick platinum was deposited by DC magnetron sputtering and patterned by lift-off through a double-layer resist process to serve as the first electrode layer. To allow characterization of clamped and released PZT films from the same deposition process, the platinum layer was patterned into circles on half of the substrate and a blanket layer on the other half, as shown in Figure 2-3. The blanket Pt was the bottom electrode for the clamped PZT while the circles served as the top electrode after transfer to polyimide. The process for this layer is described below.

The lithography for the metal patterning is a lift-off process and it happens before the metal deposition. After hotplate-baking the sample at 200°C in air for 10 minutes and letting it cool to room temperature, MicroChem PMMA C4, the first layer resist, was statically dispensed and spun on the $Al_2O_3/ZnO/SiO_2/Si$ stack at 3000 RPM for 40 seconds. It was then baked on a hotplate in air at 160°C for

8 minutes. After cooling to room temperature, Shipley 1811, the 2nd (top) layer photoresist was dispensed and spun in the same fashion and baked on a hotplate in air for 2 minutes. The Shipley 1811 layer was then exposed on a Gen II MA/BA 6 (Süss MicroTec, Garching, Germany) contact aligner with a soda-lime silica based hard mask for a total of 54 mJ/cm^2 broadband UV dose. The exposed resist was developed for 1 minute in MICROPOSIT™ 351 developer and DI water in a 1:4 ratio. The sample was then rinsed with DI water for 30 seconds and blown dry with clean air or N_2 gas. A 1.5 minute oxygen plasma treatment step was performed on the photoresist layers to remove an interlayer over the exposed PMMA, which was formed due to solvent intermixing during the spin-coating step for both photoresist layers. This interlayer, like Shipley 1811, is opaque to the deep ultraviolet (DUV) wavelength. Omitting the oxygen plasma etching will result in unexposed or underexposed PMMA in the following step, when the bottom PMMA resist layer was exposed in a PR-100 UV-Ozone photoreactor (UVP, Inc) for 600 seconds with the patterned top resist (Shipley 1811) serving as a mask. The PR-100 chamber was constantly purged with N_2 flow at 20 SLPM to prevent UV absorption by air. The exposed PMMA was puddle-developed in toluene for 1.5 minutes to undercut the top 1811 layer to form a re-entrant profile, as seen in Figure 2-2 (a), a feature necessary for the metal to successfully lift off the photoresist without flagging. The fundamental working principal of a metal lift-off using a double-layer lithography process is illustrated in Figure 2-2 (a) through (c).

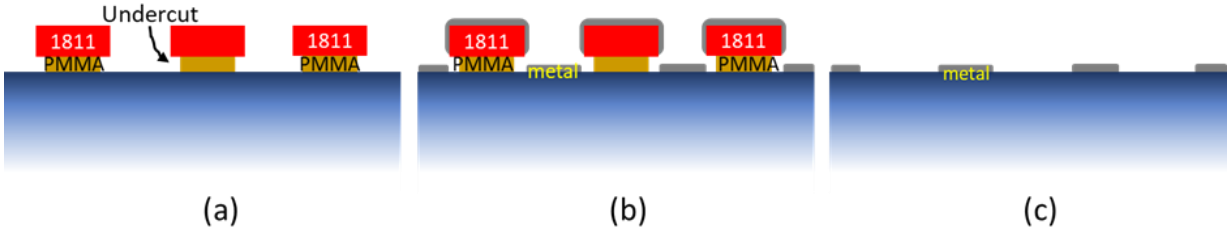

Figure 6-2. A double-layer lithography process that leads to the lift-off of the deposited metal layer. Starting with (a) creating a re-entrant profile where PMMA undercuts the 1811 photoresist, (b) the metal layer is then sputter-deposited everywhere on the sample surface. (c) The metal deposited on the 1811 is lifted off by removing 1811 and PMMA in an acetone bath, leaving the rest of the metal to form the desired pattern on the sample.

A photoresist process that requires MICROPOSIT™ CD-26 as the developer should be avoided for this step as the active ingredient in the developer, tetramethylammonium hydroxide (TMAH), etches

Al_2O_3 and ZnO [24]. Before moving on to Pt sputter-deposition, one more oxygen plasma treatment with the same parameters was performed to remove any possible photoresist residue and to increase the surface energy. An additional dehydration bake at 110°C for 15 minutes on a hotplate was carried out immediately before loading the sample into the metal sputter system. It was found that an immediate dehydration bake beforehand was crucial in preventing metal blistering and local adhesion failure.

The platinum deposition was at room temperature in a Kurt J. Lesker CMS 18 system at 2.5 mTorr process pressure with an RF power at 200 W. The 3-inch Pt target was tilted at 15° and placed at a 15 cm distance from the substrate in a sputter-up configuration. Ar was used as the sputtering gas. These parameters resulted in a ~0.4 Å/s deposition rate.

The metal patterning was achieved by immersing the sample in an acetone bath at room temperature or heated to 50-70°C, where the solvent dissolved both PMMA and Shipley 1811 and thus lifting off the metal deposited on the resist. The sample was then immersed in 80°C N-Methyl-2-pyrrolidone (NMP) for 5 minutes for a more thorough resist residue removal step as NMP is more aggressive in terms of photoresist stripping. The sample was rinsed by IPA followed by DI water, and blown dry with clean air or N_2 followed by an additional oxygen plasma cleaning step.

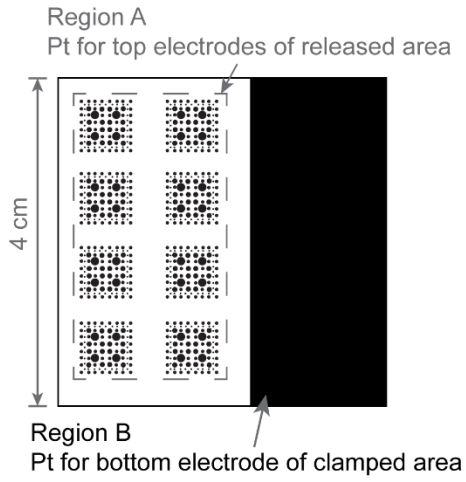

Figure 6-3. The sample is divided into Region A with patterned top Pt electrode and Region B with blanket bottom Pt electrode for the area to be released and to remain clamped, respectively. Image reproduced from [1].

PZT thin-films of the composition at the morphotropic phase boundary with 2% Nb doping were deposited over the patterned platinum electrodes via the sol-gel route. 15wt% Mitsubishi E1 PZT solution (Mitsubishi Materials Corporation, Hyogo, Japan) was statically dispensed onto the substrate and spin-casted at 2750 RPM for 40 seconds followed by a hotplate bake at 100ºC for 1 minute to drive away the 1-butanol and propylene glycol carrier solvent before the hotplate pyrolysis at 300ºC for 4 minutes. It was then crystallized in the AccuThermo AW 810 rapid thermal annealing (RTA) system (Allwin 21 Corp, Morgan Hill, CA, USA) at 700ºC for 1 minute in air. As a single deposition layer yields a thickness of ~90 nm, these steps were repeated 12 times to reach a desired thickness of ~1 µm. An individual crystallization step for each layer was preferred in order to achieve a maximal film density. A 0.08M PbO capping layer was applied after 12 layers of PZT coating to convert any surface pyrochlore on the PZT film to perovskite. The surface pyrochlore can be observed as small crystalline particles in the field effect scanning electron microscope (FESEM) image of Figure 2-4. The PbO solution was spin-casted at 5000 RPM in order to achieve a much thinner layer with respect to the main PZT film body. The PbO film was baked, pyrolyzed, and crystalized following the same temperature and time conditions of those for PZT.

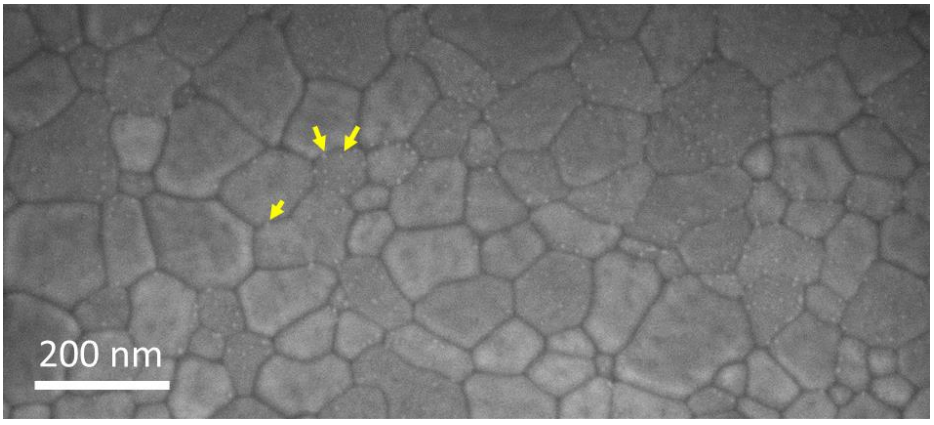

Figure 6-4. The lead deficient surface pyrochlore (selectively marked by arrows) are observed as small particles on the PZT surface captured by FESEM.

Before committing to further processing, the PZT films were inspected by examining the x-ray diffraction (XRD) pattern, as well as the field effect scanning electron microscopy (FESEM) images. The XRD pattern of a 1 µm thick sol-gel PZT film at MPB with 2% Nb doping, as shown in Figure 2-5,

confirms the pure perovskite phase with incomplete orientation. FESEM images in Figure 2-6 show well-formed PZT grain boundaries with an average grain size of 600 nm and a film surface free of pyrochlore. The cross-section micrograph shows the step coverage over the patterned Pt. At the surface of the PZT film, the absence of the step-like topography shows good planarization of multiple sol-gel depositions. The horizontal lines are a result of individual crystallization steps.

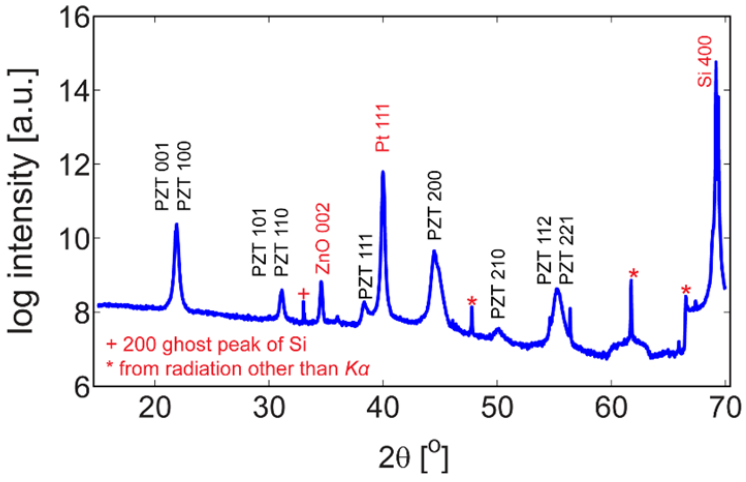

Figure 6-5. X-ray diffraction pattern of the CSD PZT film. It is phase pure and only partially oriented. Image reproduced from [1].

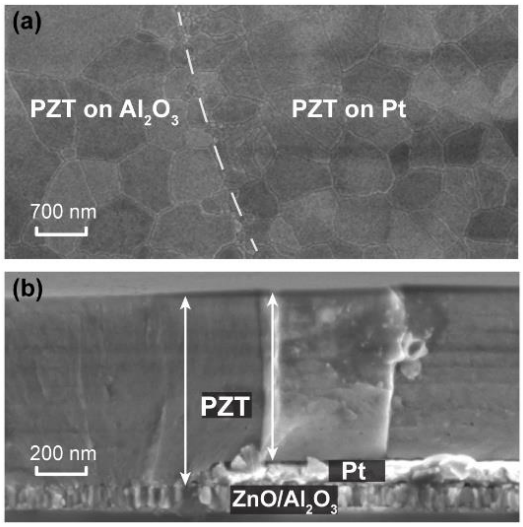

Figure 6-6. FESEM micrograph of the PZT film. (a) Film surface free of pyrochlore. (b) Cross-section of the PZT film over patterned Pt electrode. The Pt step is smoothed out at the PZT top layers due to good planarization [1].

After the inspection by XRD and FESEM, the sample was cleaved and divided into two sections: one with PZT on patterned Pt and the other with PZT on blanket Pt. The latter became the clamped sample, which was completed once a second platinum electrode layer was deposited and patterned into circles of diameters from 200 μm – 1 mm. The circle section of the lithography mask in Figure 1-2 was used for this step.

To continue the fabrication for the sample to be released, a blanket Pt of 100 nm thick was sputter-deposited to serve as the second electrode layer. 20 nm thick Al_2O_3 by PEALD was deposited on the blanket Pt to block the migration of free hydrogen, which was suspected to evolve from the polyimide during the imidization step. The free hydrogen degraded the PZT by reducing the switchable polarization [25, 26]. The polarization – electric field (P-E) hysteresis data comparing released PZT films with and without Al_2O_3 barrier are presented in Figure 2-8. The flexible substrate was deposited by spin-coating PI-2611 (MicroSystems, Parlin, New Jersey) polyamic acid precursor on the Al_2O_3 protected Pt layer at 2000 RPM for 40 seconds. The film was hotplate baked at 110ºC for 5 minutes for solvent removal and cured on a hotplate in air at 330ºC for 6 hours. The curing ambient along with the patterning status of the PZT had an impact on the Al_2O_3 barrier effectiveness level and the polarization degradation magnitude. The two parameters were not taken into consideration until the PZT layer was patterned during the transducer device fabrication. Further discussion of flexible ultrasonic transducer devices follows in the next chapter of this thesis.

The degradation to the PZT film is shown as the slanted P-E hysteresis loop with clockwise rotation in Figure 2-8 (a). The remanent polarization was reduced to 1-2 $\mu C/cm^2$ as opposed to a normal value of ~20-30 $\mu C/cm^2$. During the early development stage for the release process, little consideration was given to the curing ambient conditions and the focus was instead fixed on finding effective barrier layers to block the presumed free hydrogen migration. That is why a layer of 20 nm Al_2O_3 was used to protect the PZT and it was indeed able to effectively prevent the degradation. The hysteresis of a non-degraded sample is shown in Figure 2-8 (b) with a fuller shape and normal remanent polarization value.

To release the PZT and polyimide combination from the Si substrate, the sample stack was immersed in a 50% acetic acid bath heated to 60-70ºC. Diluting and heating the etchant assisted the mass transport by encouraging the exchange of reaction products and fresh etchant at the exposed ZnO edges. Acetic acid at higher concentration does not necessarily yield a faster release due to the slow mass transport resulting from the high viscosity. Figure 2-7(a) shows the PZT-polyimide combination in the etchant bath near the completion of the release process.

Harvesting the released PZT films on 5 μm polyimide required meticulous handling considering the significant flexibility of the thin polymeric substrate. After the ZnO was fully dissolved in the acetic acid, the released PZT film was flipped up-side-down in the bath with a pair of tweezers to have the device side face up. While the film was floating in the etchant, a piece of rigid carrier substrate (e.g., glass, Si) was slid underneath the flexible sample and slowly lifted out of the bath. Occasionally a pair of tweezers was used to aid the sample to stay in-place on the carrier. The sample was transferred to at least three DI-water baths consecutively to clean off any acetic acid residue in a static manner. Direct rinsing using a DI water hose might damage the flexible sample. The same "slide-and-lift" technique was used between bath transfers as well as in the final sample retrieval from the water bath. The released film stack was dried in ambient air while the excess water on the carrier substrate was absorbed by gently dabbing a cleanroom swab or a piece of cleanroom cloth around the polyimide. A blow-dry step with air or N_2 should be avoided as it may cause the sample to flap or fly away. In fact, leaving the polyimide bottom surface moderately wet helped the sample stay flat and in-place on the carrier substrate due to the meniscus force.

Figure 2-7(b) shows the flexibility of the released film and 2-7(c) shows the film taped onto a rigid carrier wafer with the patterned Pt side up. After release and post-release handling, both the PZT and Pt were crack-free without any signs of electrode delamination from the PZT film, as shown in an optical microscope image in Figure 5(d). For a sample as described above, the release process took approximately one day to complete. To shorten the release time, especially in case of large area films,

thicker sacrificial layer film can be grown, and/or holes can be etched from the top polyimide layer to the sacrificial layer to provide more points of access for the etchant.

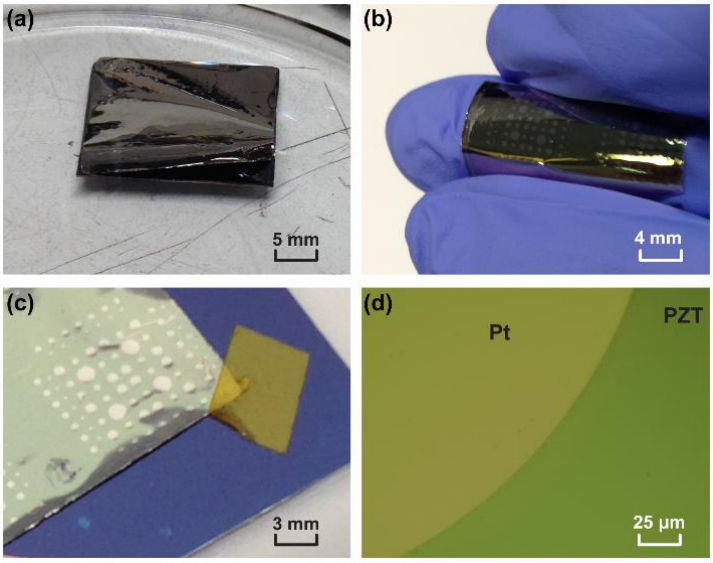

Figure 6-7. (a) In the etchant bath, the PZT film is largely freed from the silicon substrate. (b) The flexible released PZT film. (c) The released film taped onto a rigid carrier wafer with circular Pt contacts facing up. (d) No cracks or electrode delamination are observed by optical microscopy inspection. Figure reproduced from [1].

2.3 Electrical characterization results and discussion

Films on polyimide substrates (denoted as released) and films on silicon substrates (denoted as clamped) are characterized by the measurement of relative dielectric permittivity, loss tangent, and polarization – electric field (P-E) hysteresis loop. Rayleigh characteristics were also evaluated at 1 kHz to assess the ac electric field dependence. The PZT films were poled at three times the coercive field of 160 kV/cm at 125ºC for 15 minutes and cooled under the field.

Information on the switchable polarization was obtained by measuring the P-E hysteresis on a Radiant Technologies Precision LC ferroelectric tester with 500 kV/cm maximum electric field at 100 Hz and room temperature. For a PZT film of 1 µm thickness at MPB with 2% Nb doping, as seen in Figure 2-8, the remanent polarization increased to 26 µC/cm^2 upon release compared to 17.5 µC/cm^2 of the same

film on Si. An increase in the maximum polarization and a counterclockwise rotation of the hysteresis loop were also observed. The increased switchable polarization indicates improved domain reorientation, due to reduced mechanical clamping of the PZT film [10, 27]. The counterclockwise loop rotation was believed to be a result of a reduction in the PZT film stress compared to the as-grown films. The larger thermal expansion coefficient of PZT compared to Si induces a residual tensile stress in the PZT film upon cooling from the crystallization temperature to ambient. As tensile stress tends to cause a clockwise rotation to the P-E loop [28], the rotation in the opposite direction suggests a possible relief in the film stress upon release to polyimide [29].

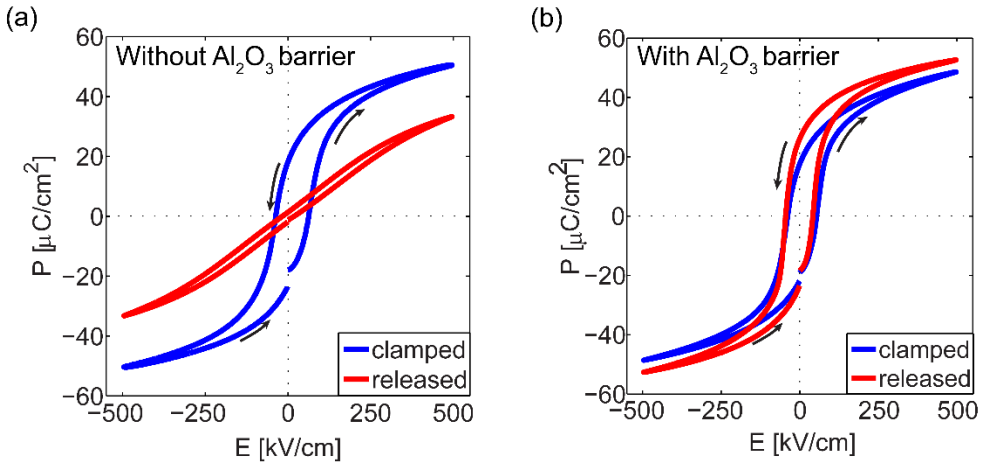

Figure 6-8. (a) Curing polyimide in air over unprotected Pt bottom electrode degraded the PZT film, shown as the slanted P-E hysteresis loop measured on released films. The remanent polarization suffered a 90% reduction. (b) With a 20 nm thick Al_2O_3 layer added between the polyimide and the blanket Pt electrode, degradation was successfully suppressed during polyimide curing. Moreover, the P-E loop of the released film here showed a 45% increase in the remanent polarization accompanied by a counterclockwise loop rotation, indicating enhanced domain wall motion due to substrate de-clamping [1].

A Hewlett-Packard 4284A LCR meter was used to measure the capacitance and dielectric loss ($\tan\delta$) at 30 mV excitation level from 100 Hz to 100 kHz at room temperature. Relative dielectric permittivity (ε_r) was then calculated based on the measured capacitance value C, the electrode area A, and the film thickness t as shown in Equitation 2-1 for a capacitor of parallel-plate configuration.

$$C = \frac{\varepsilon_r \varepsilon_0 A}{t} \qquad \text{Eqn. 2-1}$$

Figure 2-9 plots the relative permittivity as a function of frequency where each data point is the average value of five capacitors with the top electrode a circle of 600 μm diameter. At 1 kHz, the relative permittivity was slightly above 1100 in the clamped films on Si and slightly below 1200 for the released films on polyimide. The tan δ for both scenarios were around 3%. Poling reduced the permittivity for both clamped and released states because of the reduction in the number and/or the mobility of domain walls, and the switching from a-domain to c-domain, as the latter possesses a lower permittivity. Therefore, the level of ε_r reduction could be used to gauge the effectiveness of poling. The poling induced reduction in the permittivity was 17% in the released films and a mere 3% in the clamped films. This is consistent with the hypothesis found in the hysteresis loop study: in the released state, there is less restoring force from the substrate to hinder the dipole alignment with the poling electric field. Poling was therefore more effective [30] for the PZT films on polyimide. The dielectric loss was around 4% after poling.

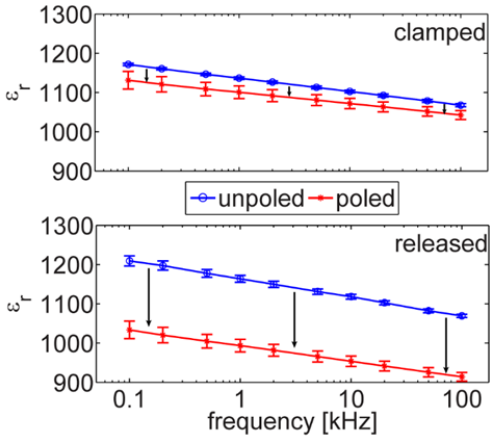

Figure 6-9. Dielectric permittivity measured at 30 mV level at a frequency range from 100 Hz to 1 kHz. The level of permittivity reduction reveals the effectiveness of poling, which then gives information on the restoring force level from substrate clamping [1].

The dielectric response in ferroelectrics is comprised of an intrinsic and an extrinsic component. The intrinsic component is a result of single domain lattice response while the extrinsic component is a contribution largely from domain wall motion [31]. The study of ac electric field (amplitude) dependence

of the dielectric behavior, or Rayleigh analysis, is an excellent tool for understanding the extrinsic response [32, 33]. Using the Rayleigh law, the real part of the relatively permittivity ε_r' can be written in the following form:

$$\varepsilon_r' = \varepsilon_{r,init}' + \alpha' E_0 \ , \qquad \text{Eqn. 2-2}$$

where the first term is the reversible Rayleigh parameter, representing a combined contribution of intrinsic lattice response and reversible domain wall motion. In the second term, α' is the irreversible Rayleigh parameter representing the irreversible domain wall motion, and E_0 is the amplitude of the ac electric field. Dielectric permittivity measurements at 1 kHz as a function of ac electric field amplitude are plotted in Figure 2-10. The Rayleigh behavior was observed up to one half of the coercive field. The Rayleigh parameters were obtained by linearly fitting the permittivity curve in the Rayleigh region where the crossing point at zero field is $\varepsilon_{r,init}'$ while the slope of the line gives the value of α'.

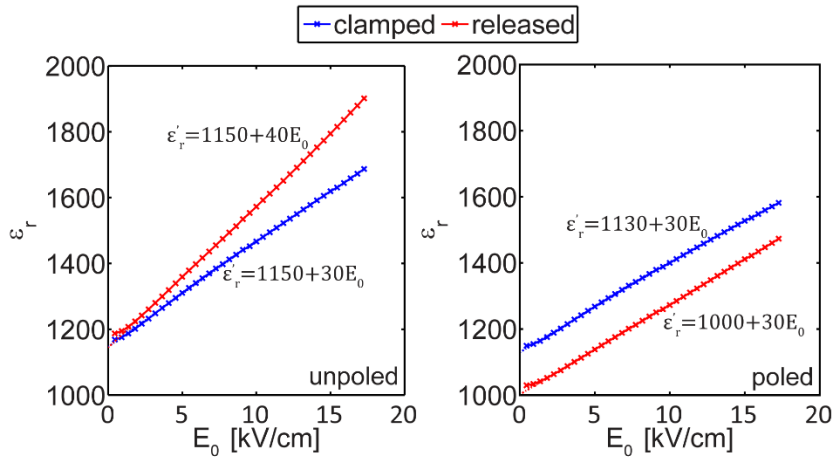

Figure 6-10. Rayleigh analysis at 1 kHz for the released and clamped PZT films before and after poling. Image reproduced from [1].

The parameters for the released and clamped PZT films before and after poling based on the data in Figure 2-10 are summarized in Table 2-1.

Table 6-1. The Rayleigh parameters obtained from the ac field dependence measurement of the relative dielectric permittivity.

1.1 μm PZT		ε'_{init}	α' [cm/kV]	$\alpha'/\varepsilon'_{init}$
Clamped	Unpoled	1150±5	30±0.2	0.026
	Poled	1130±15	30±1	0.027
Released	Unpoled	1150±9	40±1	0.035
	Poled	1000±11	30±0.5	0.030

The effects of releasing PZT films from rigid Si to flexible polyimide are reflected in the Rayleigh parameters. The reversible Rayleigh parameters for both clamped and released PZT films were nearly identical in the unpoled state, indicating that there is a similar combined effect from the reversible domain wall motion and the a-domain to c-domain switching. But upon poling, both states experienced a decrease in the ε'_{init} but to a larger degree in the released films. It is likely because the residual stress alleviation as the PZT film separated from the rigid Si allowed 1) more a-domains to be re-oriented to c-domains with the latter having less contribution in the intrinsic lattice response, 2) more strong pinning sites to be removed and/or the depth of potential wells lowered, and 3) a larger percentage of the reversible domain wall motion to be converted to irreversible motion.

The dynamics of the irreversible Rayleigh coefficient values in Table 2-1 also revealed how substrate de-clamping could increase domain wall mobility and result in more pronounced poling-induced domain wall removal in the PZT films on polyimide. The higher α' in the released films than the clamped ones before poling suggests a higher mobility in the domain walls. But poling appeared to be more effective in the released PZT films on polyimide, as can be seen from the α' reduction from 40 cm/kV to 30 cm/kV, while the number remained the same for clamped PZT films.

2.4 Exploring alternative polymeric substrates

The polyimide curing-induced degradation to the PZT polarizations motivated an excursion to search for alternative polymeric substrates. Two types of pre-imidized polyimides and two types of photoresist films: PMGI (LOR) and SU-8 were studied in this work as possible candidates.

CP1 Polyimide

As the degradation source, free hydrogen was suspected to have evolved during the PI-2611 imidization process, pre-imidized polyimides naturally became a choice for consideration. Solution-cast 25 µm or 45 µm thick CP1 was reported to be used as the flexible substrate for fabrication of large-area organic light-emitting diodes (OLEDs) that can be cut, folded, and "popped up", a concept borrowed from Kirigami, the Japanese art of paper cutting and folding [34]. To assess the feasibility of CP1 as the substrate for thin-film PZT devices, a 38 wt% clear polyimide CP1 powder (NeXolve, Hunsville, AL, USA) was dissolved in anhydrous diglyme (Sigma Aldrich) in a N_2 filled glove box. The resin was then spin-coated on the sample in air at 3000 RPM for 40 s and baked at 240 ºC in air for 2 hours to yield ~ 20 µm thick films. The PZT and electrodes were not protected by any Al_2O_3 hydrogen barrier layer in this case. A crosslinker treatment step was added prior to release, in which the sample was immersed for 20 minutes in a methanol based 10 wt% p-xylylenediamine solution to increase the CP1 film's chemical resilience. Without the crosslinker treatment, solvents like acetone readily swelled the hard-baked polymer film and formed cracks, as can be seen in Figure 2-11 (left). 1 µm thick PZT films with patterned Pt electrodes were then transferred to the CP1 after the ZnO release layer was dissolved in the acetic acid. Severe stress-induced delamination of the Pt electrodes was observed after the transfer (Figure 2-11, right). Electrical measurements could not be carried out due to the electrode delamination.

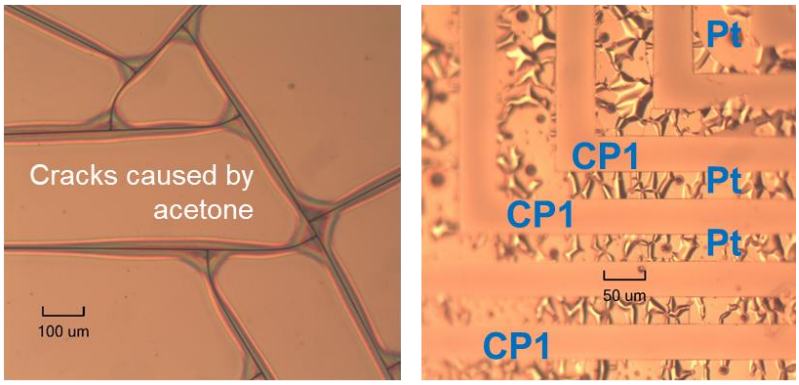

Figure 6-11. (Left) without a crosslinker treatment, the hard baked CP1 films were readily attacked by acetone and formed cracks. (Right) Severe delamination of the Pt traces observed after the release.

Polyimide by Alfa Aesar

With the dissatisfying mechanical characteristics of CP1, the focus turned to a different member in the pre-imidized polyimide family, a polyimide product manufactured by Alfa Aesar (Product number: 43656). 20 wt% powder was dissolved in N-Methyl-2-Pyrrolidone (NMP) solvent in air and the solution was stirred with a magnetic stir bar on a 50ºC hotplate for 40 minutes while capped. After cooling down to room temperature, the solution was spin-coated on the sample at 2000 RPM, baked at 160ºC for 3 minutes and hard baked at 250ºC for 1 hour in air. The final film thickness was 5 µm.

Unlike CP1, the as-baked Alfa Aesar polyimide film was already resistant to solvents like acetone without any need for crosslinker treatment. Additional testing confirmed its resilience also to basic developers like CD-26, and the ZnO release layer etchant, acetic acid. The better chemical robustness made the situation appear promising. However, like CP1, the released films also suffered Pt electrode delamination. An attempt was made to improve the metal-polymer adhesion by adding a 40 nm PEALD Al_2O_3 layer prior to the polyimide spin-casting. The delamination issue was lessened to a point that electrical measurements on a probe station could be made and the PZT showed no signs of polarization degradation after being transferred to the Alfa Aesar polyimide layer. But the mechanical characteristics, as shown in Figure 2-12, were still far from satisfactory. Cracks and wrinkles would likely become failure points that lead to unreliable devices.

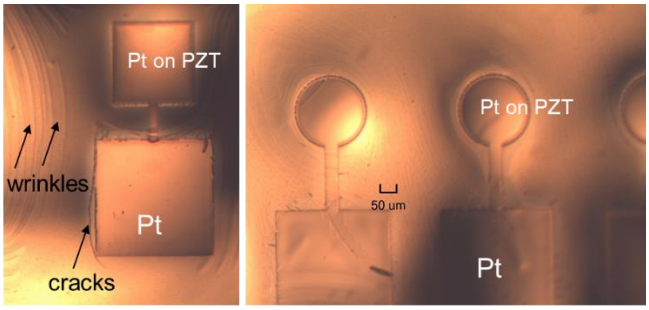

Figure 6-12. Patterned 1 µm PZT layer with patterned 100 nm Pt electrodes released on a 5 µm thick Alfa Aesar polyimide layer with 40 nm aluminum oxide adhesion promoter. Electrical measurements could be made and they confirmed no degradation to the PZT polarization. But the mechanical characteristics, as suggested by the wrinkles and cracks, were unsatisfactory.

Apart from the pre-imidized polyimides, photoresists are another possible category for flexible substrate candidates. As photoresists are involved in most microfabrication processes, they are likely to be chemically compatible with a variety of materials, including PZT and the rest of the sample stack. If the mechanical characteristics are compatible, crosslinked photoresists could serve as alternative flexible substrates. SU-8 and PMGI (LOR) were evaluated as flexible substrates for PZT films with Pt electrodes on an underlying ZnO sacrificial layer.

SU-8

SU-8 is a widely used negative-acting photoresist in microfabrication that can easily reach a thickness of tens of microns. Here, over patterned PZT and Pt electrodes on a Si substrate without Al_2O_3 barrier, the "SU-8 25" (MicroChem, Westborough, MA, USA) solution was spin-coated at 2000 RPM and baked at 65ºC for 3 minutes followed by 95ºC for 7 minutes in air. The film was then crosslinked by UV exposure on a Gen 4 MA/BA6 broadband aligner for a dose of 200 mJ/cm^2 and post-baked at 95ºC for 4 minutes before being developed in the "SU-8 developer" (Sigma-Aldrich) for 4 minutes. To make the SU-8 layer more mechanically and chemically stable, a 20 minute-long hard-bake was conducted at 200ºC. The final film thickness was measured to be 25 µm.

Patterned PZT along with the Pt electrodes were transferred to the 25 µm SU-8 layer after the ZnO sacrificial layer was fully dissolved in the acetic acid etchant. Despite some visible wrinkles on the

Pt traces, as shown in Figure 2-13(c), the released PZT and Pt layers were relatively well adhered to the SU-8 substrate, which was a major improvement compared to the pre-imidized polyimide substrates. However, the SU-8 layer was brittle and lacked flexibility, which caused small bits of the sample to chip off when being handled and flexed (See Figure 2-13 (a)).

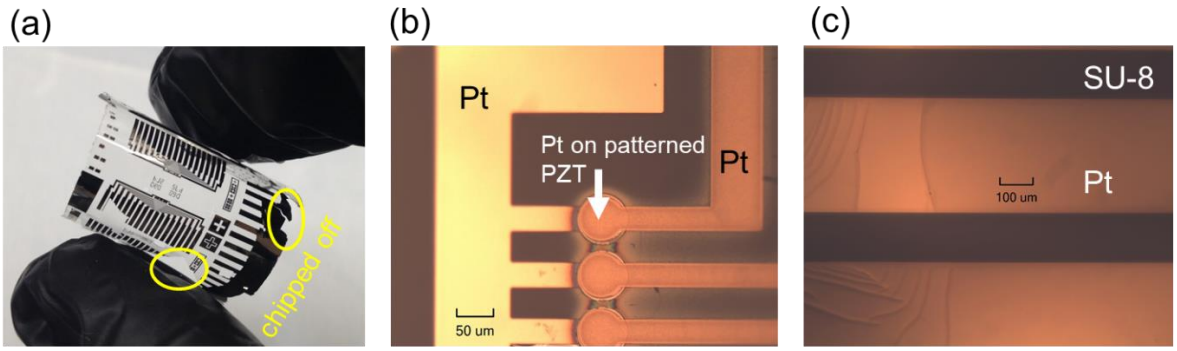

Figure 6-13. Patterned PZT with Pt electrodes released onto a 25 µm SU-8 layer. (a) Due to the brittleness of the SU-8 layer, the released sample lacked flexibility and began to crumble when flexed. (b) The Pt traces and the patterned PZT layer were relatively well adhered to the substrate despite a few wrinkles in the metal layer as shown in (c).

PMGI/LOR

The PMGI layer was introduced by spin-coating LOR 30B (MicroChem, Newton, MA, USA) at 1500 RPM and baked at 180ºC for 10 minutes to reach a final thickness of 5 µm. The sample was excessively soft and shapeless upon release. The PMGI thickness was then doubled by applying multiple coats in an attempt to stiffen the released structure but the improvement was negligible, as shown in Figure 2-14(a).

Adding a blanket metal or oxide layer was another solution considered. Following the PMGI spin-coating, as two separate experiments, a layer of either 100 nm Ti or 40 nm aluminum oxide (Figure 2-14 (a) and (b), respectively) was added to increase the rigidity. The Ti layer was deposited in a Perkin-Elmer DC magnetron sputtering system, 2400-8L. The Al_2O_3 was deposited in the same PEALD system with the same parameters as for the Al_2O_3 hydrogen-barrier layer. However, in either scenarios, the improvement was inadequate.

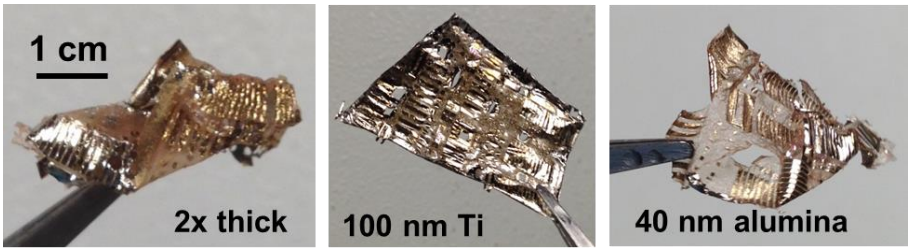

Figure 6-14. Futile attempts to stiffen the PMGI substrate-based released PZT sample by (a) doubling the PMGI thickness to 10 µm, (b) adding 100 nm Ti on the PMGI before release, and (c) adding 40 nm Al_2O_3 on the PMGI before release.

Even though none of the CP1, Alfa Aesar polyimide, SU8, and PMGI films qualified as an alternative flexible substrate, the process of studying them provided more understanding of the criteria for choosing flexible substrates for piezoelectric and oxide thin-film devices. To summarize the criteria, the polymer should possess the following characteristics as a suitable flexible substrate:

(1) Chemically robust so that the substrate will not be damaged during release, basic lithographic processes, and of course, in use.

(2) Compatible with PZT and other material layers in the sample stack where no degradations should occur when co-processed.

(3) Flexible but at the same time stiff enough to accommodate oxide and metal thin films without introducing cracks and wrinkles.

(4) Readily available in thickness of a few to tens of microns.

2.5 Chapter conclusions

In this work, 1 µm thick, blanket PZT thin films up to 2.5 cm × 2.5 cm in lateral dimension were transferred from thermally robust Si substrates to polyimide by etching away a ZnO release layer. Al_2O_3 buffer layers were used to prevent ZnO-PZT diffusion and to block imidization induced hydrogen migrating

to the PZT. The released films showed superior material properties compared to the same films on Si due to reduced substrate clamping. Polarization-electric field hysteresis measurements showed nearly a 45% increase in the remanent polarization (from 17.5 μC/cm^2 to 26 μC/cm^2). Poling at $3E_c$ for 15 minutes at 125°C either induced more ferroelectric and ferroelastic realignment or significantly decreased the density of reversible domain walls in released films, which resulted in a reduction in relative permittivity of 17% compared to only 3% for clamped films. These measurement results, along with Rayleigh analysis, confirmed the correlation between the reduced substrate clamping and improved irreversible domain wall contributions in the films on polymeric substrates.

Based on experimental studies on alternative polymer layers, solution-cast polymeric substrates for thin-film PZT based devices should be chemically resilient, co-processing compatible, flexible but mechanically robust, and available in appropriate thickness. The released films and the transfer process developed in this work are attractive for flexible sensor, transducer, and energy harvester applications.

2.6 Chapter reference

[1] T. Liu, M. Wallace, S. Trolier-McKinstry and T. N. Jackson, "High-temperature crystallized thin-film PZT on thin polyimide substrates," *Journal of Applied Physics,* vol. 122, pp. 164103, 2017.

[2] S. Trolier-McKinstry, F. Griggio, C. Yaeger, P. Jousse, D. Zhao, S. Bharadwaja, T. Jackson, S. Jesse, S. V. Kalinin and K. Wasa, "Designing piezoelectric films for micro electromechanical systems," *IEEE Trans. Ultrason., Ferroelectr., Freq. Control,* vol. 58, pp. 1782, 2011.

[3] Y. Kato, T. Sekitani, Y. Noguchi, T. Yokota, M. Takamiya, T. Sakurai and T. Someya, "Large-area flexible ultrasonic imaging system with an organic transistor active matrix," *IEEE Trans. Electron Devices,* vol. 57, pp. 995, 2010.

[4] M. Losego, L. Jimison, J. Ihlefeld and J. Maria, "Ferroelectric response from lead zirconate titanate thin films prepared directly on low-resistivity copper substrates," *Appl. Phys. Lett.* , vol. 86, pp. 1, 2005.

[5] H. Yeo and S. Trolier-McKinstry, "{001} Oriented piezoelectric films prepared by chemical solution deposition on Ni foils," *J. Appl. Phys.,* vol. 116, pp. 14105, 2014.

[6] A. Kingon and S. Srinivasan, "Lead zirconate titanate thin films directly on copper electrodes for ferroelectric, dielectric and piezoelectric applications," *Nat. Mater,* vol. 4, pp. 233, 2005.

[7] J. Cheng, W. Zhu, N. Li and L. Cross, "Electrical properties of sol-gel-derived $Pb(Zr_{0.52}Ti_{0.48})O_3$ thin films on a $PbTiO_3$-coated stainless steel substrate," *Appl. Phys. Lett.*, vol. 81, pp. 4805, 2003.

[8] T. Suzuki, I. Kanno, J. Loverich, H. Kotera and K. Wasa, "Characterization of Pb (Zr, Ti)O3 thin films deposited on stainless steel substrates by RF-magnetron sputtering for MEMS applications," *Sensors Actuators, A Phys.,* vol. 125, pp. 382, 2006.

[9] F. Xu, S. Trolier-McKinstry, W. Ren, B. Xu, Z. Xie and K. Hemker, "Domain wall motion and its contribution to the dielectric and piezoelectric properties of lead zirconate titanate films," *J. Appl. Phys.,* vol. 89, pp. 1336, 2001.

[10] M. Wallace, R. Johnson-Wilke, G. Esteves, C. Fancher, R. Wilke, J. Jones and S. Trolier-McKinstry, "In situ measurement of increased ferroelectric/ferroelastic domain wall motion in declamped tetragonal lead zirconate titanate thin films," *J. Appl. Phys.,* vol. 117, pp. 54103, 2015.

[11] F. Griggio, S. Jesse, A. Kumar, O. Ovchinnikov, H. Kim, T. Jackson, D. Damjanovic, S. V. Kalinin and S. Trolier-McKinstry, "Substrate clamping effects on irreversible domain wall dynamics in lead zirconate titanate thin films," *Phys. Rev. Lett.*, vol. 108, pp. 1, 2012.

[12] M. Kobayashi, C. Jen and D. Lévesque, "Flexible ultrasonic transducers," *IEEE Trans. Ultrason., Ferroelectr., Freq. Control,* vol. 53, pp. 1478, 2006.

[13] H. Gullapalli, V. S. M. Vemuru, A. Kumar, A. Botello-Mendez, R. Vajtai, M. Terrones, S. Nagarajaiah and P. M. Ajayan, "Flexible piezoelectric ZnO-paper nanocomposite strain sensor," *Small*, vol. 6, no. 15, pp. 1641, 2010.

[14] N. Bu, N. Ueno and O. Fukuda, "Monitoring of respiration and heartbeat during sleep using a flexible piezoelectric film sensor and empirical mode decomposition," in *Proceedings of the 29th IEEE EMBS*, 2007, pp. 1362.

[15] Y. Zhu, J. Zhu, Y. Song and S. B. Desu, " Laser-assisted low temperature processing of Pb(Zr, Ti)O_3 thin film," *Applied Physics Letters,* vol. 73, pp. 1958, 1998.

[16] S. Kim, Y. Bastani, H. Lu, W. King, S. Marder, K. Sandhage, A. Gruverman, E. Riedo and N. Bassiri-Gharb, "Direct fabrication of arbitrary-shaped ferroelectric nanostructures on plastic, glass, and silicon substrates," *Adv. Mater* , vol. 23, pp. 3786, 2011.

[17] A. Rajashekhar, A. Fox, S. Bharadwaja and S. Trolier-McKinstry, "In situ laser annealing during growth of Pb($Zr_{0.52}Ti_{0.48}$)O_3 thin films," *Appl. Phys. Lett.*, vol. 103, pp. 32908, 2013.

[18] Y. Qi, N. Jafferis, K. Lyons, C. Lee, H. Ahmad and M. McAlpine, "Piezoelectric ribbons printed onto rubber for flexible energy conversion," *Nano Lett.*, vol. 10, pp. 524, 2010.

[19] P. Tue, T. Shimoda and Y. Takamura, "Lift-off process for fine-patterned PZT film using metal oxide as a sacrificial layer," *J. Micromech. Microeng*, vol. 27, pp. 14004, 2017.

[20] Y. Do, W. S. Jung, M. Kang, C. Kang and S. Yoon, "Preparation on transparent flexible piezoelectric energy harvester based on PZT films by laser lift-off process," *Sensors Actuators, A Phys.*, vol. 200, pp. 51, 2013.

[21] H. Yeo, C. Yeager, X. Ma, J. Ramirez, K. Sun, C. Rahn, T. Jackson and S. Trolier-McKinstry, "Piezoelectric MEMS Energy Harvesters," in *Proc. ASME 2014 Conf. Smart Mater. Adapt. Struct. Intell. Syst.*, Newport, Rhode Island, 2014, no page numbers.

[22] R. Johnson-Wilke, R. Wilke, M. Wallace, J. Ramirez, Z. Prieskorn, J. Nikoleyczik, V. Cotroneo, R. Allured, D. Schwartz, S. McMuldroch, P. Reid, D. Burrows, T. Jackson and S. Trolier-McKinstry, "ZnO thin film transistors and electronic connections for adjustable x-ray mirrors: SMART-X telescope," in *In Adaptive X-Ray Optics III*, vol. 9208, International Society for Optics and Photonics, 2014, pp. 920809.

[23] D. Zhao, "Plasma-enhanced atomic layer deposition zinc oxide flexible thin film electronics," Ph.D. thesis, Department of Electrical Engineering, The Pennsylvania State University, University Park, PA, 2010.

[24] K. G. Sun, Y. V. Li, D. B. S. John and T. N. Jackson, "pH-controlled selective etching of Al_2O_3 over ZnO," *Appl. Mater. & Interfaces*, vol. 6, pp. 7028, 2014.

[25] J. C. Coburn, and M. T. Pottiger, "Thermal curing in polyimide films and coatings," in *Polyimides Fundamentals and Applications*, M. Ghosh and K. Mittal, Eds., New York, NY, Marcel Dekker Inc., 1996, pp. 207.

[26] K. Rho, S. Zurn, D. Markus and D. Polla, "Integration of a CMOS preamplifier with a lead zirconate titanate resonant frequency microsensor," *J. Electrochem. Soc.* , vol. 149, pp. J53, 2002.

[27] S. Buhlmann, B. Dwir, J. Baborowski and P. Muralt, "Size-effect in mesoscopic epitaxial ferroelectric structures: Increase of piezoelectric response with decreasing feature-size," *Appl. Phys. Lett.*, vol. 80, pp. 3195, 2002.

[28] J. F. Shepard, F. Chu, B. Xu and S. Trolier-McKinstry, "The effects of film thickness and texture on the high and low-field stress response of lead zirconate titanate thin films," *Mat. Res. Soc. Symp. Proc.*, vol. 493, pp. 81, 1997.

[29] R. Keech, S. Shetty, M. A. Kuroda, X. H. Liu, G. J. Martyna, D. M. Newns and S. Trolier-McKinstry, "Lateral scaling of $Pb(Mg_{1/3}Nb_{2/3})O_3$-$PbTiO_3$ thin films for piezoelectric logic applications," *J. Appl. Phys.*, vol. 115, pp. 234106, 2014.

[30] C. Yeager, "PZT thin films for piezoelectric MEMS mechanical energy harvesting," PhD dissertation, Department of Materials Science and Engineering, The Pennsylvania State University, University Park, 2015.

[31] R. Herbiet, U. Robels, H. Dederichs and G. Arlt, "Domain wall and volume contributions to material properties of PZT ceramics," *Ferroelectrics*, vol. 98, pp. 107, 1989.

[32] D. Damjanovic, "Ferroelectric, dielectric and piezoelectric properties of ferroelectric thin films and ceramics," *Rep. Prog. Phys.*, vol. 61, pp. 1267, 1998.

[33] D. V. Taylor, and D. Damjanovic, "Evidence of domain wall contribution to the dielectric permittivity in PZT thin films at sub-switching fields," *J. Appl. Phys.*, vol. 82, p. 1973, 1997.

[34] T. Kim, J. S. Price, A. Grede, S. Lee, G. Choi, W. Guan, T. N. Jackson and N. C. Giebink, "Kirigami-inspired 3D organic light-emitting diode (OLED) lighting concepts," *Adv. Mater. Technol.*, vol. 3, pp. 1800067, 2018.

Chapter 3. Flexible thin-film PZT based ultrasonic transducers on polyimide substrates

3.1 Motivation for developing flexible thin-film piezoelectric ultrasonic transducers

There is a growing interest in flexible, miniaturized ultrasonic transducer devices for use in medical diagnosis and biometric authentication applications. Compared to conventional ultrasound technologies, such devices can conform to complex shapes and geometries, integrate with portable electronics operating under low driving voltages, and access small apertures of imaging interest.

Advancing the performances of flexible, miniaturized ultrasonic transducer devices can benefit catheter-based ultrasound imaging technology, in which a transducer-fitted catheter is inserted into a target of imaging interest. Intravascular ultrasound (IVUS) is an example of such a modality and plays an important role in the diagnosis and treatment of coronary diseases by visualizing blood vessels and cardiac structures via a transducer introduced into an artery [1]. One implementation approach is to wrap an array of transducers around the catheter, which demands that transducer devices be flexible and small enough to be fitted with a catheter of ~1.2 mm in diameter. The operating frequency requirement for IVUS is approximately between 10 MHz – 20 MHz [2-5].

Another application of interest lies in the development of a flexible, thin-film based finger vein detection device. Finger veins, like fingerprints, are unique to every individual, and thus qualify as a means of biometric authentication. In fact, authentication by imaging finger veins has advantages relative to many other biometrics. Since the imaging target is subdermal, the results are difficult to forge and are less affected by epidermal and environmental conditions [6]. The clearly defined vein patterns also allow more accurate identification. The current commercial finger vein sensors use a CCD camera coupled with near infrared light; this coupling produces relatively large devices [7]. If piezoelectric thin-film based ultrasonic transducers are readily available for imaging finger veins, this authentication technology can be integrated into more portable electronics as well as a broader scope of applications. In fact, there are

related research efforts dedicated to developing piezoelectric micromachined ultrasonic transducer (pMUT) based fingerprint imaging devices [8-10]. A 22 MHz thin-film AlN array, fully integrated with complementary metal oxide (CMOS) circuitry, was demonstrated to produce a 2D pulse-echo image of a PDMS fingerprint phantom. In addition to miniaturization, adding flexibility to transducer devices will allow the detection sensors to conform to the shape of the finger or the components on the electronics, improving the imaging resolution.

Historically, flexible transducers were predominantly based on polymeric piezoelectrics. For example, polyvinylidene fluoride (PVDF)[11-14], odd-numbered nylons (e.g., nylon-5, nylon-7, nylon-11) [15], and composite piezoelectric materials [16][17]. Despite their flexibility, the effectiveness of these materials is limited by low piezoelectric response and low operating temperature. The composite transducers are mechanically stiff and have limited flexibility at moderate inspection frequencies around 2 MHz [18]. As an alternative, Bu et al. developed thin-film AlN sensors on polyimide substrates and polyvinylidene fluoride (PVDF) sensors that can be attached to the human body to detect pressure fluctuations resulted from the lung expansion and contraction during sleep, such that sleep apnea can be better diagnosed. [19].

3.2 Transducer fabrication building upon the release process

In this work, flexible thin-film PZT transducer devices were designed and fabricated on a 5 μm polyimide substrate targeting a width extension vibration mode with operating frequencies in the 8 MHz to 80 MHz range. The transducers were individual rectangular PZT bar resonators accessed by top and bottom Pt electrodes. The dimensions of the transducers were determined based on a simple theoretical model for a free-standing k_{31}-mode PZT ceramic plate as well as more complex computational simulations performed by Jeong Nyeon Kim using PZFlex [20]. As the flexible PZT transducer element is patterned and declamped from the rigid substrate, its boundary conditions can be approximated as similar to that of a free-standing k_{31}-plate. Operating in the fundamental width extension mode, the resonance

frequency is expressed in Equation 4-1 as a function of the sound velocity v in PZT and the width dimension W [21].

$$f_r = \frac{v}{2W} \tag{4-1}$$

Based on the PZFlex simulations and the free-standing plate model, the resonator width was predicted to be roughly 25 μm - 100 μm in order for the transducers to operate in the targeted frequency range. Width dimensions of 25 μm, 50 μm, 100 μm, and 200 μm were therefore designed with the L/W ratio of 5, 10, or 15 for a single element. Due to the novelty of the device structure, a complete set of material property parameters was not available for the simulation to precisely predict the frequency as a function of the width dimension nor the vibration behavior. Thus, some level of discrepancy was anticipated, and a better understanding of the device behavior was to be gained via empirical characterization.

The fabrication process for the flexible transducers is similar to that of the released PZT film described in Chapter 2 with a few modified and additional steps. This chapter will only highlight the differences in the fabrication process and leave out the reoccurring details that can be found in Chapter 2. The flow chart in Figure 3-1 illustrates the step-by-step fabrication process for the flexible transducers on polyimide with corresponding summarizing descriptions listed in Table 3-1.

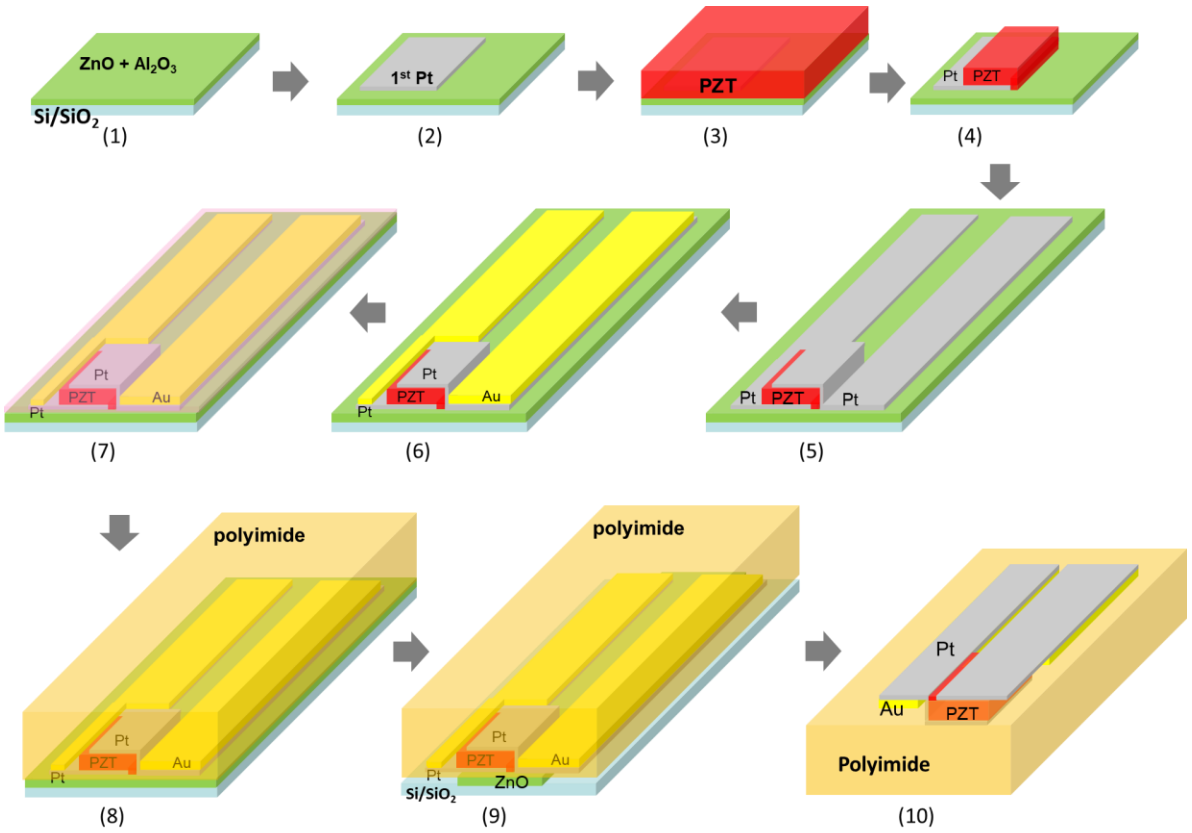

Figure 7-1. Schematics demonstrating the 10-step process for fabricating the flexible thin-film PZT based bar resonator-type transducers on a 5 µm polyimide substrate.

Table 7-1. Process summary for corresponding fabrication steps in Figure 3-1.

Step #	Process Summary
1	On a clean 4'' Si wafer with 10,000 Å SiO_2, deposit 150 nm ZnO sacrificial layer and 10 nm Al_2O_3 diffusion barrier by PEALD
2	Sputter 130 – 200 nm Pt and pattern by lift-off on Al_2O_3 to serve as the 1st electrode contact layer
3	Grow 1 µm PNZT (113/2/52/48) film by spin-casting the chemical solution, and crystallize at 700°C in RTA for 1 min
4	Pattern PZT by dry-etching in Ar, CF_4, and Cl_2 plasma in an inductively-coupled plasma etching system with 10 µm AZ 4620 photoresist etch mask
5	Sputter 130-200 nm and pattern the 2nd Pt electrode, which also overlaps the 1st Pt to form long contact leads in preparation for cable bonding
6	Sputter 500 nm Au over Pt and pattern by lift-off to reduce the overall contact resistance
7	Deposit 40-50 nm Al_2O_3 to protect the PZT transducers from degradation caused by the poly(amic acid) imidization process
8	Spin-coat polyimide precursor PI-2611 polyamic acid at 2000 RPM and cure in a tube furnace with constant Ar flow at 4 SLM at 305°C for 75 minutes
9	Immerse the sample stack in 50°C 50% acetic acid bath to etch away the ZnO sacrificial layer to facilitate the release
10	Obtain flexible PZT transducers on 5 µm polyimide after all the ZnO is dissolved in etchant

The fabrication began by depositing a ZnO sacrificial layer and an Al_2O_3 diffusion barrier layer on a clean 4-inch silicon wafer with 1 µm thick thermal SiO_2 following the same procedure in Chapter 2. Here, instead of pieces, whole Si wafers were used in order to facilitate the PZT etch process in the etch tool (explained below). After deposition of the release layer, 130 – 200 nm platinum was sputter-deposited and patterned by lift-off to define the first electrode layer for the PZT transducers. Next, 1 µm PZT was deposited over the patterned Pt contact by spin-coating the PNZT solution (Mitsubishi E1).

The PZT layer was patterned into individual bar resonators using an inductively coupled high-density plasma etching system ULVAC NE-550 (ULVAC, Inc., Japan) with a positive photoresist AZ 4620 (MicroChemicals GmbH, Germany) as the soft etch mask.

Table 3-2 describes the conditions for coating and patterning a 10 µm thick AZ 4620 layer. Due to the large photoresist film thickness, a rehydration step was necessary between the soft-bake and UV-exposure. This was achieved here simply by leaving the photoresist-coated wafer in a cleanroom ambient (~50% humidity) for about 60 minutes. While rehydration happens almost instantaneously in thin photoresist layers, the time required by the process increases in a strongly nonlinear fashion for thick photoresist coatings. Resist films that have insufficient water level will not be easily dissolved in developer [22]. Rehydration can also be expedited by immersing the wafer in a DI water bath (not verified in this work) [23].

Table 7-2. Conditions for processing AZ4620 to serve as the soft etch mask for patterning the PZT layer.

1	Substrate dehydration bake	10 min at 120°C on a hotplate
2	Spin speed	1500 RPM
3	Soft bake	2 min at 80°C followed by 4 min at 115°C on a hotplate
4	Rehydration time	60 min in ~50% ambient humidity
5	Edge bead removal	Lithographically remove by exposing the wafer edge and developing using the exposure and develop conditions in Step 6 and 7
6	Exposure	Broadband MA/BA6 contact aligner with 1400 mJ/cm^2 dose
7	Develop	7.5 min immersion in AZ400K 1:4 developer at room temperature with manual agitation (shake with hands)
8	Rinse & dry	30 sec DI water rinse and N_2 blow-dry
9	Final film thickness	10 µm measured by contact profilometry

Once the photoresist etch mask was ready, the etch process was carried out at 3.5 mTorr and 200 V self-bias (150 W power) with a gas mixture of Ar, CF_4, and Cl_2 in the ratio of 15:28:7. A substantial amount of heat was generated during the etch process due to ion bombardment. Therefore, to prevent overheating and potentially crosslinking/reticulating the photoresist, the etching process was carried out in multiple cycles of an etch-pause sequence with each cycle consisting of a 20 second etch and a 60 second pause. In addition, constant helium backside cooling was provided with the temperature set at 0°C. The above parameters gave a PZT etch rate of ~80 nm/min, roughly 10 times slower than that of the photoresist. The ULVAC NE-550 etch tool uses clamping rings compatible with only 4- or 6-inch whole wafers to cool the substrate. Etching sample pieces required mounting them onto a full-sized carrier wafer. As the mounting adhesives generally have poor thermal conductivity, cooling becomes less effective for mounted pieces, making the photoresist etch mask very susceptible to crosslinking or reticulation. As a result, full wafer substrates are strongly recommended.

After the PZT layer was etched through, the photoresist was stripped in N-Methyl-2-Pyrrolidone (NMP) at ~70ºC for 10 minutes. By inspection through optical microscope, small pieces of material were observed to be attached on the PZT and Pt near the sidewall in some areas, as shown in Figure 3-2 (a). As oxygen plasma was ineffective for removal, these material pieces were presumably an inorganic mixture of re-deposited PZT and Pt due to aggressive bombardment and excessive heating. They were so strongly

bound to the sample that removal attempts using prolonged sonication were unsuccessful. Fortunately, it was confirmed after the second Pt layer that the re-deposition was not conductive, and so did not cause an electrical short between top and bottom electrodes. After the re-deposition removal attempt, a post annealing step was performed at 550ºC in air in RTA for 2 minutes to recover any etch induced damage. Figure 3-2 (b) shows an individual PZT bar free of such re-deposition.

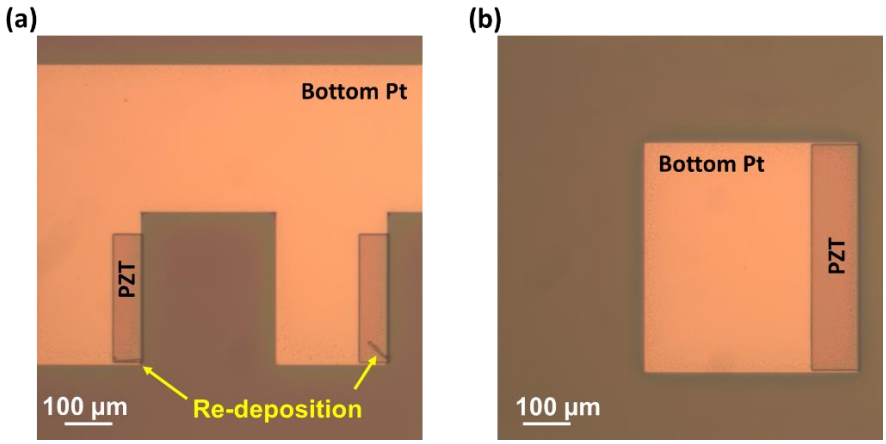

Figure 7-2. (a) A re-deposited PZT/Pt mixture was observed via optical microscope near the PZT sidewall after dry etching and photoresist stripping. The one on the right looks like a strip of material that was peeled off the PZT edge and shifted to land on the surface. (b) A larger individual PZT bar that is free of such re-deposition.

Following the post anneal, a second Pt electrode layer of 130 – 200 nm was deposited and patterned by lift-off following the same procedure as the first Pt. The second Pt extends away from the PZT resonator to form a 3.5 mm long and 250 µm wide contact in preparation for cable connections after release. The long lead extension was also applied to the first Pt layer. Step (4) through (5) in Figure 3-1 illustrates this process.

Accessing the PZT elements with long, narrow, and thin platinum contact leads results in a relatively high RC time constant for the targeted operating frequency in the MHz range, which will induce slow charge/discharge for the PZT elements and thus extraneous effects on the frequency response. The resistivity of the Pt and Au films in this work was measured to be 10.6 µΩ·cm and 2.75 µΩ·cm, respectively. For a typical segment of the Pt lead of 130 nm thick and 250 µm wide, and a PZT element with a capacitance of 50 – 300 pF, the RC time constant is in the range of 1.5 – 6 ns,

corresponding to a cutoff frequency of 25 – 100 MHz, partially overlapping the desired operating window. The overlap will further deteriorate if multiple elements are driven simultaneously. To eliminate the RC time constant effect, 500 nm thick Au films were sputter deposited overlaying the long-lead segment of both the top and bottom platinum electrode to shift the cutoff frequency window up by a factor of 5-6 times. A separate lithography step was performed to align the Au to the top and bottom Pt leads so that the PZT area could be excluded from thick metal deposition to avoid any undesirable bending as a result of structural asymmetry. Figure 3-3 shows the wafer after the Au step with a zoomed-in microscope image of a single PZT transducer element accessed by top and bottom Pt contact as well as the overlapping Au layer. The contact on the right also reveals the overlapping of the first and the second platinum layer that forms the lead extension.

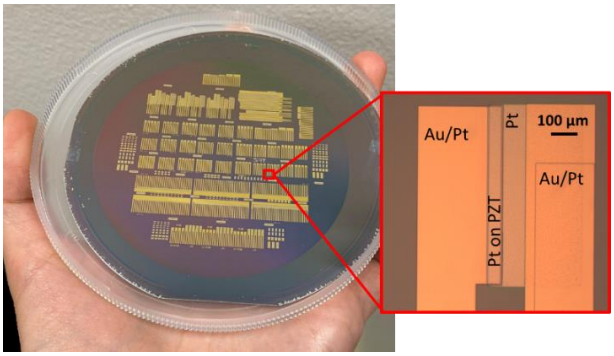

Figure 7-3. The 4-inch wafer after Au deposition and lift-off with a zoomed-in view of a single transducer element where the PZT resonator is accessed by top and bottom Pt contacts overlapped with Au. The Au layer deliberately avoids the PZT area to prevent potential undesired bending.

Before adding the flexible polyimide layer to the sample stack, a blanket 50 nm thick Al_2O_3 layer was deposited on the wafer by the same PEALD process described in Chapter 2; this layer served three important roles. First, as the sample had a large portion of open space after patterning PZT and Pt/Au, the released sample with polyimide substrate would have a structural rigidity close to that of a 5 µm free-standing polyimide film. The blanket Al_2O_3 could therefore stiffen the released structure to reduce the handling difficulty and to prevent potential damage to the elements from excessive flexing. The second function of the Al_2O_3 was to promote adhesion between the polyimide and the metal contacts. The last but

most important role, as previously discussed in Chapter 2, was for the Al_2O_3 to serve as a diffusion barrier to block the degradation-inducing species from migrating into PZT. These species, perhaps predominantly hydrogen, were likely generated during the polyimide imidization process. A large reduction in the switchable polarizations was observed in the P-E hysteresis loops as soon as PI-2611 was spin-coated and cured over the PZT transducer devices that were still clamped on Si. The following section analyzes the polarization degradation and steps taken to prevent the degradation.

3.2.1 PZT polarization reduction due to PI-2611 imidization

Hydrogen is suspected to be the origin of the degradation due to its well-known effect of significantly reducing the ferroelectric characteristics in PZT thin-films, with the situation aggravated by noble metal electrodes like Pt or Ir [24-27]. Miki et al. evaluated the degradation of thin-film Pt/PZT/Pt capacitors as a result of annealing in hydrogen ambient at 350°C in a tube furnace [27]. Their reported P-E hysteresis loop (Figure 3-4) measured after the anneal showed a near-zero remanent polarization and a ~30° clockwise rotation. The paraelectric-like loop appearance after hydrogen annealing resembles that of the degraded PZT films in Figure 2-8 (a) and Figure 3-6 (a) of this work, which were characterized after the polyimide deposition. Kushida-Abdelghafar reported the degradation of dielectric constant after the H_2 treatment to be much less drastic than the polarization: a ~50% reduction compared to that of the as-grown films. This is consistent with the observations in the released PZT films in this work, where the relative dielectric permittivity changed from 1200 to 740 (1 kHz, 30 mV excitation, RT) after curing the polyimide. The mechanism for the degradation has been proposed as a loss of tetragonality and hindered Pb-O bond formation in the PZT films [26].

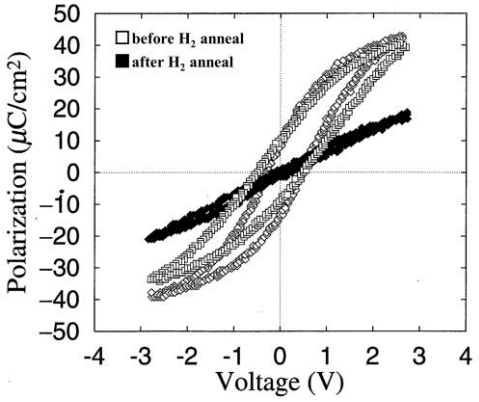

Figure 7-4. P-E hysteresis characterizations before and after annealing in forming gas with a N_2 base and 3% H_2 at 350°C for 15 minutes for a 150 nm PZT with 200 nm Pt electrodes. Figure reproduced from Miki et al. [27].

In addition, the presence of the Pt electrode can further accelerate the degradation by activating the hydrogen due to the catalytic characteristics [24]. The authors concluded that the damage existed in the Pt/PZT interface as higher leakage current was seen after H_2 treatment.

It is hypothesized that the hydrogen comes from cyclization (imidization) of the poly(amic acid) precursor of PI-2611. Among the large variety of polyimides, poly(amic acid) of PI-2611 is synthesized by reacting a dianhydride monomer of biphenyl-tetracarboxylic acid (BPDA) and a diamine monomer of p-phenylenediamine (PPD) [28]. When heat is applied to the poly(amic acid), as seen in Figure 3-5, the amide nitrogen attacks the acid carbonyl carbon and bonds to it, rejecting H^+ and OH^- to form water as a reaction product [28].

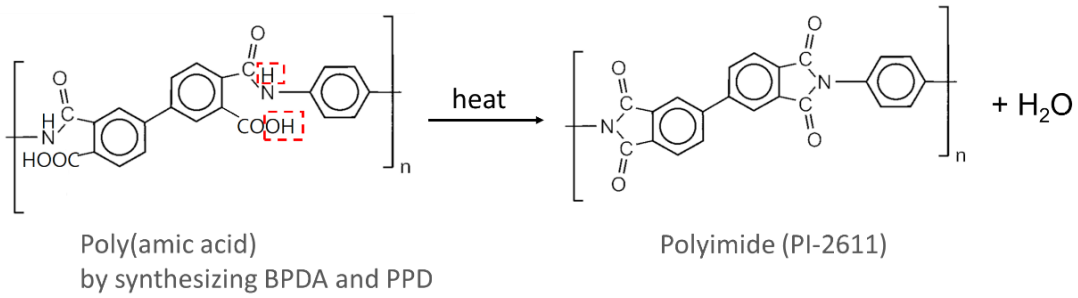

Figure 7-5. The imidization process of the BPDA/PPD poly(amic acid) form of PI-2611 generates H^+ and OH^- as the amide nitrogen bonds to the acid carbonyl carbon. The polyimide curing is therefore suspected to provide the degradation-inducing hydrogen to the PZT films.

3.2.2 Alumina as a *conditional* hydrogen barrier

In order to block the presumed hydrogen from migrating into the PZT layer to cause polarization reduction, a layer of Al_2O_3 deposited between PZT/Pt and polyimide was found to be an effective barrier, but only if two other processing conditions were met at the same time.

For curing PI-2611 poly(amic acid) in air over a blanket PZT/blanket Pt structure, as stated in Chapter 2, a 17 nm Al_2O_3 barrier layer alone was able to prevent the migration of the free hydrogen. However, for the transducers with patterned PZT and patterned metal contacts, the Al_2O_3 layer alone was no longer a sufficient barrier. As revealed by the P-E hysteresis loops in Figure 3-6 (a), reduction in the switchable polarizations occurred in PZT transducers capped with Al_2O_3 after being released to a 5 μm thick polyimide. The polyimide was hotplate-cured in air at 300°C. Although the transducer with absolutely no Al_2O_3 showed a more pronounced reduction in polarizations, no signs of improvement were observed when the barrier layer thickness was further increased from 17 nm to 40 nm.

3.2.3 An inert curing environment

The curing process described above was conducted on a hotplate in air. However, it has previously been reported that curing should be done in an environment that excludes moisture and oxygen (though no reasoning was provided). [29]. A hypothesis is that presence of oxygen could hinder the cyclization reaction by oxidizing the reagents during curing.

The missing piece to the PZT degradation suppression was therefore found by switching the curing environment from air to Ar. The PI-2611 poly(amic acid) was spun onto the Al_2O_3 barrier layer at 2000 RPM in air, baked on a hotplate at 110°C in air, and cured in a tube furnace at 305°C with constant Ar flow at 4 SLM. Due to the capacity of the furnace, the whole-wafer sample was cleaved into smaller pieces to fit onto the 3 in × 6 in graphite boat inside a quartz tube. The boat was placed right above the heating lamps. A groove at the bottom of the boat held a thermocouple tightly for close contact to ensure correct temperature measurement. The temperature profile started with a 50ºC/min ramp to reach 100ºC.

It was held at that temperature for 5 minutes, followed by ramping to 305ºC at 4ºC/min. The curing time at 305ºC was 75 minutes. The electrical properties were examined after the transducers were released and the corresponding P-E hysteresis loop, shown in Figure 3-7, was free of polarization reduction. Indeed, as was shown in the previous chapter, the switchable polarization increased on releasing the PZT from substrate-clamping.

3.2.4 The indispensable barrier layer

If the generation of hydrogen (and/or other species causing the polarization reduction) was successfully suppressed in the exclusion of oxygen and moisture, then, use of Al_2O_3 between the PZT/Pt and polyimide should be redundant. However, further investigation disapproved this hypothesis. As seen in the P-E hysteresis loops plotted in Figure 3-6 (b), when samples were prepared without Al_2O_3, reduced polarizations and pinching occurred, even though curing of the polyimide layer was carried out in a dry, inert ambient with constant Ar flow. This indicates that a proper curing environment does not necessarily suppress the polarization-reducing species. Instead degradation could be prevented only if the polyimide was cured in a dry, inert ambient and Al_2O_3 protective layer was employed. However, it is still worth noting that, the polarization reduction was less severe, and the loops still maintain a ferroelectric characteristic without an Al_2O_3 protective layer, as opposed to the ones in Figure 2-8 (a) and Figure 3-4.

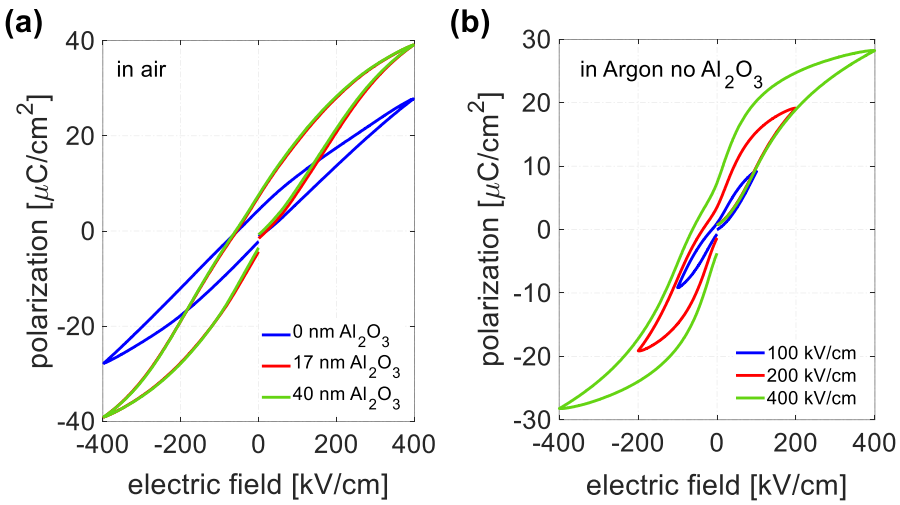

Figure 7-6. The polarization – electric field (P-E) hysteresis loops of patterned PZT transducers after polyimide was coated and cured. (a) When the polyimide was cured in air over the patterned PZT transducers coated with Al_2O_3, significant degradation was observed, in contrast to the data on released blanket PZT films with a blanket bottom Pt electrode (Chapter 2). Even though the sample without any Al_2O_3 showed worse reduction in the polarization than the ones with Al_2O_3, further increasing the barrier layer thickness did not mitigate the degradation. (b) Without any Al_2O_3, degradation still occurred in the released transducer devices after polyimide was cured in an inert Ar ambient. The P-E hysteresis loops demonstrate strong signs of pinching. This indicates that the absence of oxygen did not suppress the generation of the degrading specie.

3.2.5 Summary and discussion on imidization induced degradation

When processing the precursor of polyimide, PI-2611 poly(amic acid), over PZT/Pt devices, a large reduction of switchable polarization was observed in the PZT film. The degradation source was suspected to be hydrogen, as similar P-E hysteresis behavior and dielectric constant reduction were found in PZT/Pt capacitors annealed in H_2. H^+ is evolved during the cyclization when the amide nitrogen bonds to the acid carbonyl carbon during poly(amic acid) imidization. Depending on the PZT/Pt structure, the presence of a barrier layer, and the curing environment, PZT films respond differently to the PI-2611 co-processing.

Under the right conditions, curing PI-2611 poly(amic acid) precursor did not induce degradation.

For a blanket PZT and a blanket Pt electrode (patterned Pt electrodes on the other side of PZT not in contact with polyimide), the presumed hydrogen was blocked and the degradation averted once a layer

of Al_2O_3 was added on the Pt bottom electrode before introducing PI-2611. However, complication rose for patterned PZT with patterned Pt electrodes (both top and bottom contact). Even under the protection of Al_2O_3, the PZT was still degraded after polyimide was processed; increasing the Al_2O_3 thickness resulted in no improvement. This raised questions about the effectiveness and the mechanism of Al_2O_3 as a barrier layer for hydrogen blocking. Presumably patterned Pt had a more active catalytic reaction and either produced more degradation-inducing hydrogen species or enabled a shorter diffusion pathway for the hydrogen. The mechanism is still not well understood. In order to fully prevent the degradation for patterned structure, additional "assistance" was implemented by controlling the curing environment to an inert ambient in combination with the use of Al_2O_3. Without the oxide barrier layer, the P-E hysteresis loop became pinched and the polarization reduced. The reduction, however, was not as severe as if PI-2611 were cured in air. The absence of oxygen and moisture clearly suppressed some percentage of the degradation. But it is unclear whether the suppression was in terms of the quantity of the degrading species, or their reactivity.

Variation in the parameters of sample structure, curing environment, and presence of Al_2O_3 produced mixed results. While a working process is available for depositing PI-2611 on PZT/Pt to serve as the polyimide substrate, further investigation is required to verify the source of degradation and understand the mechanisms for both degradation and its prevention.

3.3 Release of the PZT transducer devices to polyimide

To transfer the PZT transducer devices from the Si substrate to the 5 μm polyimide layer, the device stack was immersed in a 50% acetic acid bath heated to ~50ºC to etch away the ZnO sacrificial layer. Special techniques for handling the flexible released devices are described in Chapter 2.

The released transducers were initially characterized at a probe station by directly probing the metal contacts on the polyimide to assess the basic dielectric properties. For transducer elements with 100

μm × 1000 μm lateral dimensions, the relative dielectric permittivity and dielectric loss were ~1250 and 0.03, respectively, measured at 1 kHz and 30 mV excitation level using a Hewlett-Packard 4284A LCR meter. The permittivity was ~3-5% higher after release. The switchable polarization was obtained by measuring the P-E hysteresis on a Radiant Technologies Precision LC ferroelectric tester with 400 kV/cm maximum electric field at 100 Hz and room temperature for elements of the same dimension. The P-E loop in Figure 3-7 exhibited a ~50% increase in the remanent polarization and a counterclockwise rotation on release. The results are consistent with those reported in Chapter 2 for the blanket PZT films.

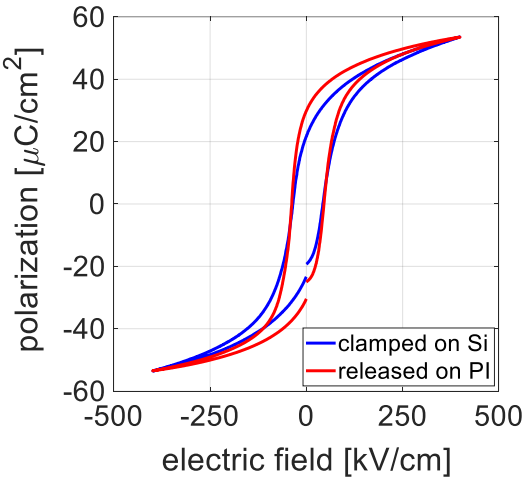

Figure 7-7. The P-E hysteresis loop of a 100 μm × 1000 μm PZT transducer element measured before and after release to the polyimide substrate. As the polyimide was cured in Ar over Al_2O_3 protected PZT and Pt, degradation was successfully prevented. Consistent with the results in Chapter 2, the released films show increased polarization due to declamping.

3.4 Making electrical connections with ACF

For testing beyond the probe station-based measurements, such as underwater acoustic testing, connections from the transducers to the external instruments were required. In this work, it was achieved via anisotropic conductive film (ACF) bonding a piece of flexible ribbon cable to the transducer devices and inserting the cable into a zero insertion force (ZIF) connector mounted on a printed circuit board. The connections on the circuit board were fanned-out to soldered pin-headers. The cables were a 50 μm thick

polyimide base with 3 µm copper traces that were arranged in the same pitch dimension as the contact pads on the flexible sample. Details on cable fabrication, ACF bonding procedure, and printed circuit board connections at Penn State are described below. This information is not limited to making connections for 5 µm polyimide substrate-based flexible transducer devices, but is also applicable to samples based on a variety of substrates and purposes. The ACF bonding technique is compatible with a selection of materials and has been frequently used on glass, silicon, polyimide substrate-based samples and printed circuit boards [30][31].

3.4.1 Flexible ribbon cable fabrication

At Penn State, the ribbon cables were designed and fabricated on Novaclad™ sheets – 50 µm polyimide coated with 3 µm copper on both sides (Sheldahl Corporation, Northfield, MN, USA). Figure 3-8 illustrates the steps for producing ribbon cables with customized designs. The cable pattern was first drawn with the software AutoSketch and printed on the copper-coated polyimide sheet using an HP LaserJet P2055dn. The Novaclad™ sheet was first cut to size and sonicated in acetone for 5 minutes followed by an IPA rinse, then blown-dry with clean compressed air. After solvent cleaning, it was treated with an oxygen plasma for 90 seconds in an RIE system described in Chapter 2, with a -30 V low substrate bias level, 100 mTorr process pressure, and 100 sccm O_2 gas flow rate. The purpose of the plasma treatment was to increase the surface energy of Cu for optimal adhesion to the printer ink. Using a high substrate bias or prolonged etching time may cause the copper sheet to burn. Immediately following the RIE treatment, the Novaclad™ was taped onto a letter-sized office paper, and fed into the printer for printing with the designed pattern. The reason for the immediate printing is because a plasma treatment for surface energy modification generally expires (becomes ineffective) in 15-30 minutes, which can be verified with a contact angle test using DI water droplets. The ink printed on the copper served as a protecting mask during copper etching, like photoresist. Due to the resolution of the printer, the printing method here can only be used for plotting features with minimum 100 µm line width and 250 µm line spacing. For finer dimensions, a photolithography route was used instead. The Novaclad™ was taped

onto a rigid substrate after the sonication and oxygen plasma cleaning; Shipley 1811 photoresist was statically dispensed and spun at 3000 RPM for 40 seconds and baked at 95 °C for 3 minutes on a hotplate in air as the sheet remained taped on the carrier.

With the protection from either the patterned ink or the photoresist, copper was etched in a 25v/v% $FeCl_3$ bath at room temperature for ~2.5 minutes or until all the unprotected copper was dissolved. The etched Novaclad™ cable was rinsed with DI water and blown dry with clean compressed air. It was then transferred to another etching bath of 0.5wt% $KMnO_4$ and 0.5wt% KOH aqueous solution for ~1.5 minutes to etch away an unknown residual conductive layer, which was suspected to be part of the seed layer deposition for the initial copper plating during the Novaclad™ manufacturing. Omitting this etch step would result in an unacceptable leakage current between adjacent traces. The cable was rinsed with DI water and blown dry with clean compressed air at the end of etching. Both $FeCl_3$ and $KMnO_4$/KOH solutions are suitable for multiple times of recycled use.

After etching, the ink was removed by sonicating the cable in acetone for 10 minutes followed by gently wiping the residual ink with a cleanroom swab. After rinsing with IPA, the cable was blown dry with clean compressed air. The same stripping procedure applied to the photoresist etch mask.

To prevent the traces from oxidizing, Au was plated onto the Cu surface using an electroless plating method, where the cable was immersed in 90°C Transene Bright electroless gold-plating solution for 10 minutes. The plating was a self-terminating corrosion process where Au in the solution replaced Cu near the trace surface. The end point was confirmed based on the visible appearance change of the traces: turning into a gold-like color. The plating solution can also be recycled and used multiple times until saturation – indicated by a blue color of the solution.

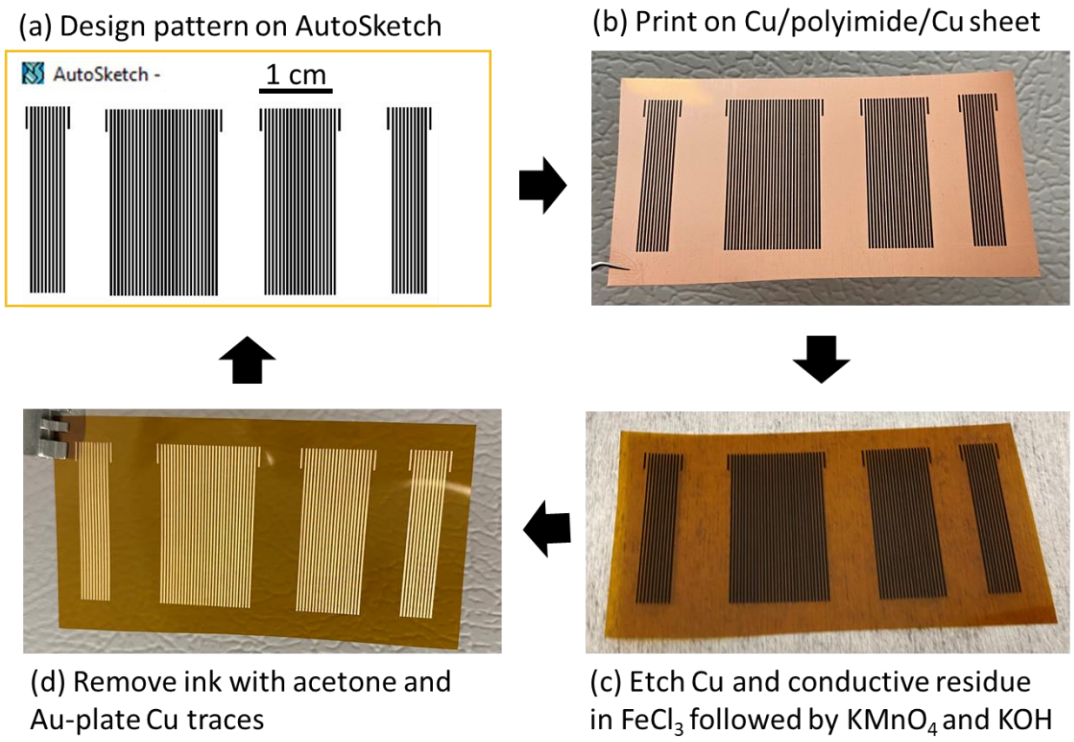

Figure 7-8. Fabrication process of the flexible ribbon cable. (a) Starting by designing the cable pattern on Autosketch, and (b) printing the design on the Novaclad sheet. (c) The Cu was patterned in 25% $FeCl_3$ followed by a conductive layer removal in 0.5% $KMnO_4$ and 0.5% KOH. (b) For anti-oxidation, Au was electroless-plated on Cu after ink removal in acetone.

The cable was then cut from the polyimide sheet and further trimmed to dimensions with a pair of scissors. For more precise dimension requirement, cutting should be done with a computer-controlled laser-cutter.

3.4.2. Bonding with ACF

The anisotropic conductive film (ACF) bonding technique is widely used in chip-on-film (COF) and chip-on-glass (COG) applications such as in flat panel display assembly [30-32]. The ACF, a B-stage epoxy matrix embedded with conductive particles, serves as a conducting adhesive tape between the cable and the sample to be bonded. The ACF tape is first tacked on either the sample or the cable with applied pressure and heat. The opaque backing is then peeled off to reveal the transparent ACF, which allows the cable traces to be aligned to the sample contacts. Pressure is applied to the sample/ACF/cable sandwich

structure to deform the epoxy and traps the conductive particles between each aligned electrode pair to establish electrical connections. While the particles between the corresponding electrodes are in contact with one another, the ones in regions outside of the electrodes stay isolated. As a result, electrical connections are restricted in the direction perpendicular to the bonding pads while electrical insulation is maintained between neighboring contacts. Simultaneously or subsequently, heat is applied to cure the epoxy to form mechanical bonds as well as to lock the conductive particles in place. The particles are usually 2-10 μm in diameter. Figure 3-9 illustrates the cross-sectional view of the bonding process.

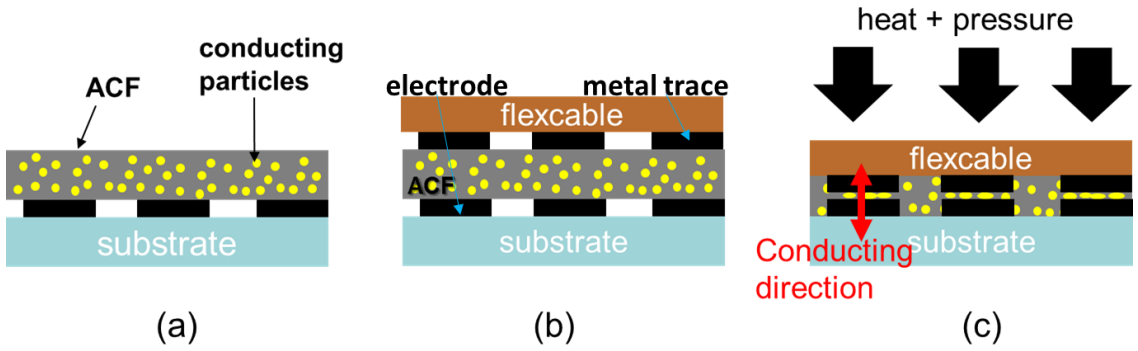

Figure 7-9. Cross-sectional schematics illustrating the bonding process using ACF. (a) The ACF is first tacked onto the substrate or the cable. (b) The cable is placed on the sample with the traces aligned to the sample electrodes once the ACF is stripped of its opaque backing. (c) Conducting particles are deformed and touch one another between the corresponding electrodes but stay unconnected in regions outside of the electrodes. As a result, electrical connections were restricted in the direction perpendicular to the bonding pads while electrical insulation was maintained between neighboring contacts.

The system that realizes the heat and pressure application is a UNITEK 9200 bonder (now obsolete) connected with a Hughes HTT-1000 power supply. As shown in Figure 3-10, the bonder consists of a pneumatic cylinder-driven thermode that moves up and down to apply pressure on the ACF adhesive. The HTT-1000 power supply provides current to the thermode to induce Joule heating. The thermode's movement and heating are controlled independently via depressing two footswitches. Most commercially available bonders execute these two functions simultaneously with a single switch, which leaves no opportunity for the thermode to be re-positioned before curing the ACF epoxy. In this study, the tool was rewired to allow separate control: heating will not start until the user confirms the thermode

position and depresses a second switch. The original hand switch was also replaced by foot pedals in order to free up the user's hands for sample manipulation.

The alignment between the cable traces and sample leads is visualized by a hobbyist microscope shown in Figure 3-10. The tackiness of an uncured ACF allows the alignment to be conducted away from the thermode site if desired. The aligned sample and cable will be held together with enough adhesion during transfer to the thermode.

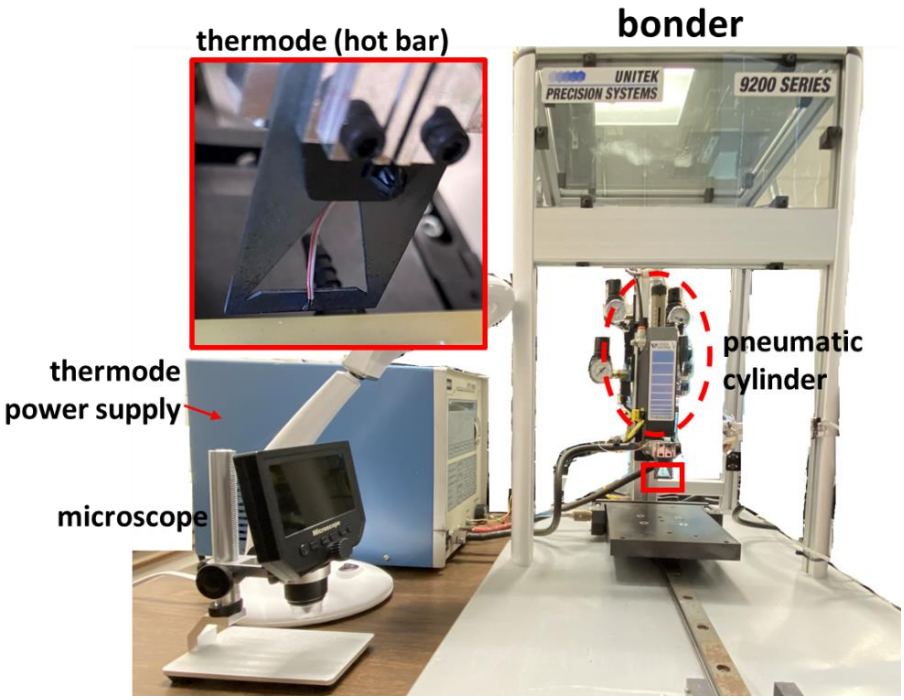

Figure 7-10. The bonding system that applies heat and pressure to the ACF adhesive and facilitates the bonding. The hobbyist microscope in the lower left corner provides visual aid to the offsite cable alignment.

Here, for bonding ribbon cables to the released PZT transducers on polyimide, a piece of 18 μm thick and 1.5 mm wide AC-7206U ACF (Hitachi, Japan) was first tacked onto the cable at 90°C for 10 seconds with a piece of thin thermally conductive silicone elastomer placed between the ACF and the bonder head to help uniformly distribute the force and heat. The ACF backing layer was then peeled off before bringing the cable to the transducer sample to align the traces with respect to the bonding pads. With the ACF sandwiched between the sample and the cable, heat and pressure were applied at 180ºC and approximately 1-3 MPa for 40 seconds to complete the final bonding step.

The above bonding temperatures generally apply to thermally insulating substrates. In case of bonding on more thermally conductive materials, such as Si and metal foil, 130ºC is used for ACF tacking and 240ºC is used for the final bonding step to compensate for the heat loss.

3.4.3 Connection with circuit boards

With one end bonded to the flexible transducer samples, as shown on the right-hand side of Figure 3-11, the other end of the ribbon cable was inserted into a ZIF connector mounted on a printed circuit board fanned out to soldered pin headers. Before the ZIF insertion, the ribbon cable was trimmed to the width dimension of the ZIF connector socket. A maximum offset tolerance of ~0.5 mm was allowed, otherwise misalignment would cause misconnections between the cable traces and the ZIF contacts. Additionally, a 100 µm Kapton tape was laminated on the ribbon cable in the insertion region to increase the cable thickness for secure insertion (left panel in Figure 3-11). The 50 µm as-fabricated cable described above (at Penn State) cannot be properly locked in-place in the socket due to insufficient thickness. For waterproofing, 1.5-2 µm parylene C (Parylene Coating Services, Inc.) was coated in a Lab Top Parylene Deposition System (Para Tech Coating) over the sample/cable combination circumventing the ZIF insertion region, which was masked with Kapton tape prior to parylene deposition. 2 g of the parylene C powder produced ~1.6 µm in the final coating thickness.

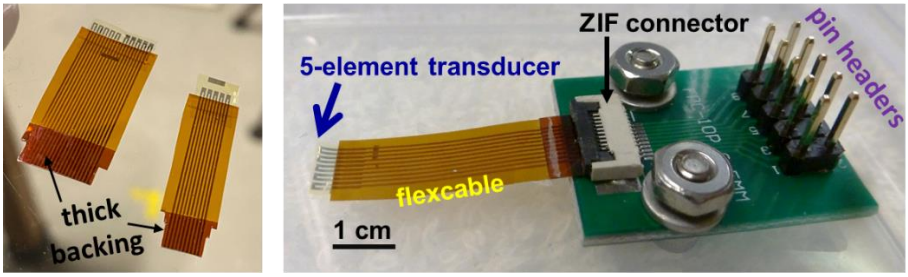

Figure 7-11. In order for the cable to be securely inserted into the ZIF connector with metal contacts properly aligned, the cables (left) were trimmed to the dimension of the ZIF socket with a maximum ~0.5 mm offset tolerance and laminated with a 100 µm thick Kapton tape to increase the thickness. After parylene deposition for water-proofing, the cable was inserted into a ZIF connector mounted on a printed circuit board with soldered pin headers (right).

Alternatively, for the ACF development at Penn State, instead of inserting the cable into a ZIF connector, the ribbon cable can also be ACF-bonded to the printed circuit board with corresponding contact pads matching the pitch dimension of the traces.

3.5 Acoustic testing of the transducer devices

3.5.1 Sample configuration and poling

Two types of samples were made for the acoustic testing: (1) individual transducers arranged in a 1-D array, and (2) individual elements independently accessed with top and bottom leads.

For the 1-D transducer array, 32 single elements were accessed with 32 top contact leads and two shared leads for common ground. Each element had a 1 μm thick PZT layer of 100 μm × 1000 μm in lateral dimension with 400 μm (kerf) spacing between two adjacent elements. Figure 3-12 shows an array sample with cables bonded and connected to a PC board ready for testing.

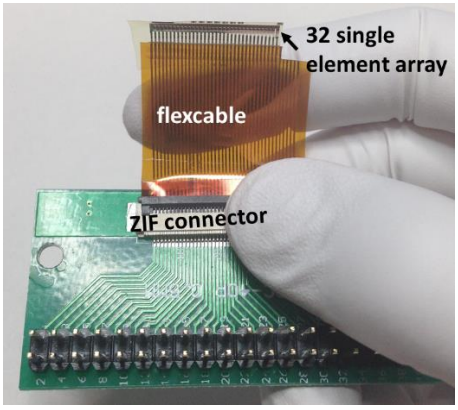

Figure 7-12. A 1-D array of 32 single element PZT thin-film transducers on a 5 μm thick polyimide layer. Each element has 1 μm thick PZT of 100 μm × 1000 μm lateral dimensions. A flexible ribbon cable connects the transducer devices to a printed circuit board.

For the independently leaded single elements, 5 or 10 transducers on one substrate were connected to one PC board. The PZT elements were separated by 1 mm. This arrangement allowed the contact leads to be in a consistent 0.5 mm pitch pattern to match the flexible cable and to comply with the in-lab bonding technology. Arrangements such as $\lambda/2$ spacing to facilitate focusing and steering of the

acoustic beam were not considered here. An example for an individually leaded sample can be found in Figure 3-11. Figure 3-13 explains the arrangement of the contact leads.

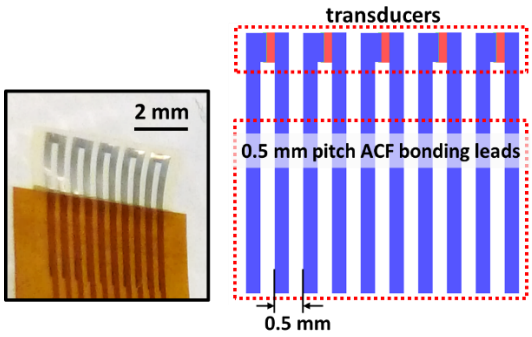

Figure 7-13. Samples containing individually leaded transducer elements have the top and bottom contact leads arranged in parallel and following a 0.5 mm pitch spacing rule. The traces on the flexible cable (left panel) also had a 0.5 mm pitch spacing and therefore could be aligned with the contact leads on the sample.

Samples for acoustic testing were poled at 120°C and $3E_c$ for 15 minutes and cooled under field. Voltages were applied on the PC boards through the ZIF connectors and the flexcables. An average of 17% reduction in the dielectric permittivity was observed for the elements after poling, confirming the poling effectiveness.

3.5.2 Measurements with a bulk commercial transducer

Underwater acoustic testing was conducted at Prof. Sri-Rajesekhar Kothapalli's research laboratory with the help of Dr. Ajay Dangi, who designed and integrated the test setup. Prof. Kothapalli and Dr. Dangi are in the Biomedical Engineering Department at Penn State.

The fabricated flexible transducers were first tested with a bulk commercial transducer in water to confirm the capability of receiving (catching) and transmitting (pitching) acoustic waves. For the pitch mode tests, the fabricated flexible transducers were driven by pulses using a function generator, and the launched signal was then received by the commercial transducer. The catch mode tests were conducted using the fabricated transducers to receive the acoustic pulses generated by the commercial transducer. The setup for both pitch and catch mode testing is illustrated in Figure 3-14.

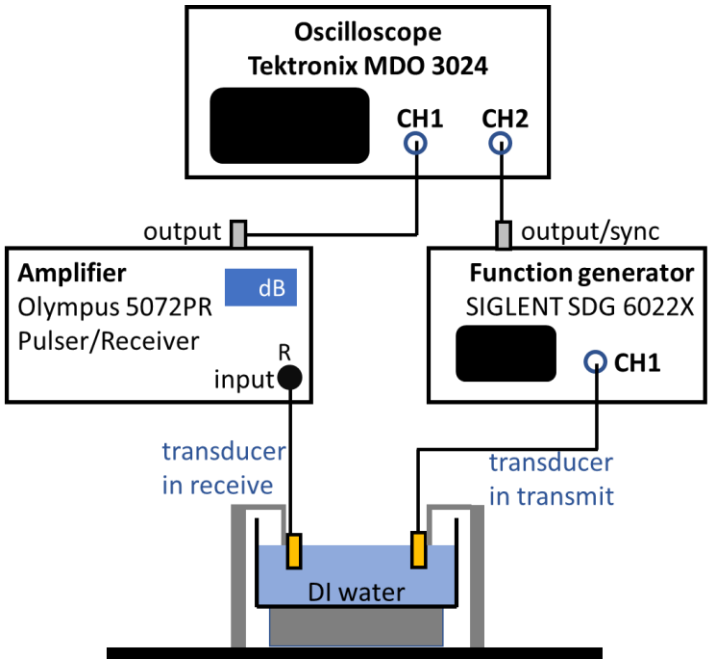

Figure 7-14. The setup for characterization of two elements transmitting and receiving acoustic signals with respect to each other. The transmitting element was driven by a function generator, from which the excitation was output to an oscilloscope. The signal detected by the element in receive was amplified and displayed on the oscilloscope. In the case of a bulk transducer with good sensitivity, amplification was usually omitted.

The fabricated flexible transducer sample and the bulk commercial transducer were mounted to kinematic mirror mounts on posts fixed on an NRT 100 3-axis linear translation stage (Thorlabs, Inc). The kinematic mount allowed adjustment of the orientation of the two transducers about the axes of rotation in the pitch (vertical) and yaw (horizontal) directions, as Figure 3-15 schematically illustrates. The transducers were attached on the movable front plate of the mount, which was driven by rotating the screws on the fixed back plate.

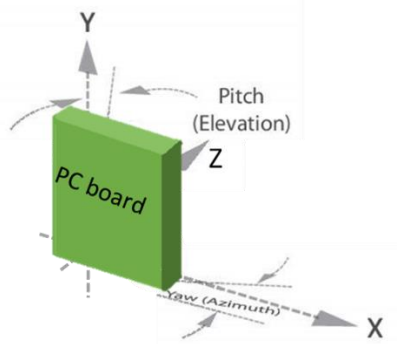

Figure 7-15. The kinematic mount allowed adjustment of the orientation of the two transducers about the axes of rotation in the pitch (vertical) and yaw (horizontal) directions.

As shown in Figure 3-16, the rigid PC board was in contact with the kinematic mount above water while the flexible cable and sample hung off the board so that they could be immersed in water. The commercial transducer was initially rough-aligned perpendicular to the fabricated flexible transducers using the 3-axis stage and the mounts. As the fabricated transducers were on a 5 µm polymer layer, it was not flat and tended to bend when immersed in water. This made the surface of the flexible transducer point at an arbitrary direction, and therefore increased the alignment difficulty with respect to the commercial transducer. The flexibility of the fabricated transducers also partially invalidated the tilt angle adjustment as the tilting of the rigid PC board was likely not fully transferred to the flexible sample in water. Fine-tuning the alignment was performed *in situ*, based on the quality of received acoustic signals when both transducers were in operation.

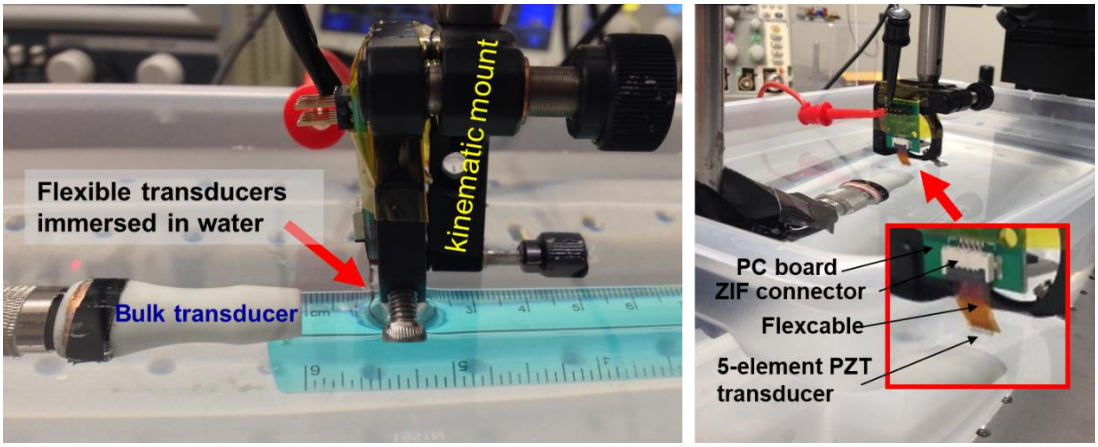

Figure 7-16. Setup for underwater testing in receive and transmit mode with a commercial bulk transducer. The commercial transducer is aligned perpendicular to the five individually leaded single transducer elements on one sample. Each PZT element is 25 μm × 500 μm in lateral dimension and the sample has an overall size of 1 cm × 1 cm. The flexible transducer bends underwater due to its high degree of flexibility.

The transmitting transducer was driven by a SIGLENT SDG 6022X function generator in burst mode. The output signal from the function generator was then recorded by the Tektronix MDO 3024 oscilloscope. As the acoustic signal was launched from the transmitting element and detected by the one in receive, it was amplified by an Olympus 5072 PR ultrasound pulser/receiver. The signal after gain was then recorded by the same oscilloscope. Typically, a 30-39 dB amplification was used for the fabricated flexible bar PZT resonators.

The flexible transducers under test were 25 μm × 500 μm single elements populated on a 1 cm × 1 cm polyimide substrate. The bulk transducer, placed at 1.5 cm distance, had a central frequency of 3.5 MHz. In receive mode tests, the bulk transducer was driven by 2 cycles of 10 V bipolar excitation with an output time delay of 2 μs. The launched signal was detected by a single flexible element and recorded by the oscilloscope after a 30dB gain. Figure 3-17 (a) plots the detected signal before amplification. One of the 25 μm × 500 μm transducer elements received 0.25 mV signal at the 11.5 μs time mark. Subtracting the 2 μs launch signal delay and using the speed of sound in water, the time duration was converted to the distance traveled by the acoustic signal from the transmitting to the receiving element, which was consistent with the 1.5 cm separation distance. In addition, by linearly shifting the flexible transducer with respect to the bulk transducer, the corresponding timing changed self-consistently.

In the pitch mode tests, one of the flexible transducer single elements was driven by 2 cycles of 5 V unipolar signal at 3.5 MHz. The detected signal by the bulk transducer before amplification is plotted in Figure 3-17 (b). The signal with a smaller amplitude immediately following the main signal was suspected to be transmission from multiple neighboring elements due to crosstalk. As the smaller signal appeared to be stretched over a longer time duration, it was perhaps a combination of staggered acoustic signals from the elements mechanically excited by the pitching transducer. Using 2800 m/s as the sound velocity in polyimide [33], the distance travelled one-way was calculated as 2.8 mm, which was

approximately the separation between the pitching transducer (the second element) and the farthest neighbor, as can be seen in Figure 3-13.

The above tests demonstrated that the fabricated PZT bar resonators were able to transmit and receive acoustic signals and could indeed function as transducer devices.

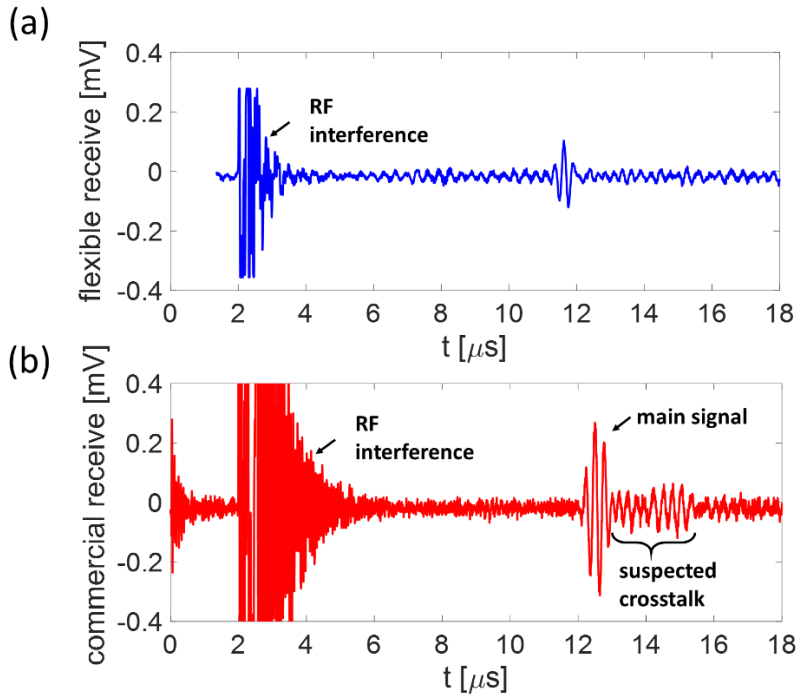

Figure 7-17. Signal detected by (a) the transducer in receive, and by (b) the bulk transducer in receive. These two sets of tests confirmed that the fabricated thin-film PZT bar resonators function as transducers.

3.5.3 Pitch-catch

After confirming the functionality of the fabricated PZT resonators as transducers, pitch-catch testing was performed in water between two neighboring single elements in transmit and receive, respectively. The acoustic waves transmitted by the pitching element were reflected from an aluminum plate placed at 1.5 cm distance and received by the catching element.

The setup of the testing and driving instruments for pitch-catch was the same as that illustrated in Figure 3-14. The positioning of the transducer devices (Figure 3-18 (a) and (b)) was different, however.

Both pitching and catching elements were fabricated flexible transducers on the same substrate, and they were placed parallel to the reflector plate.

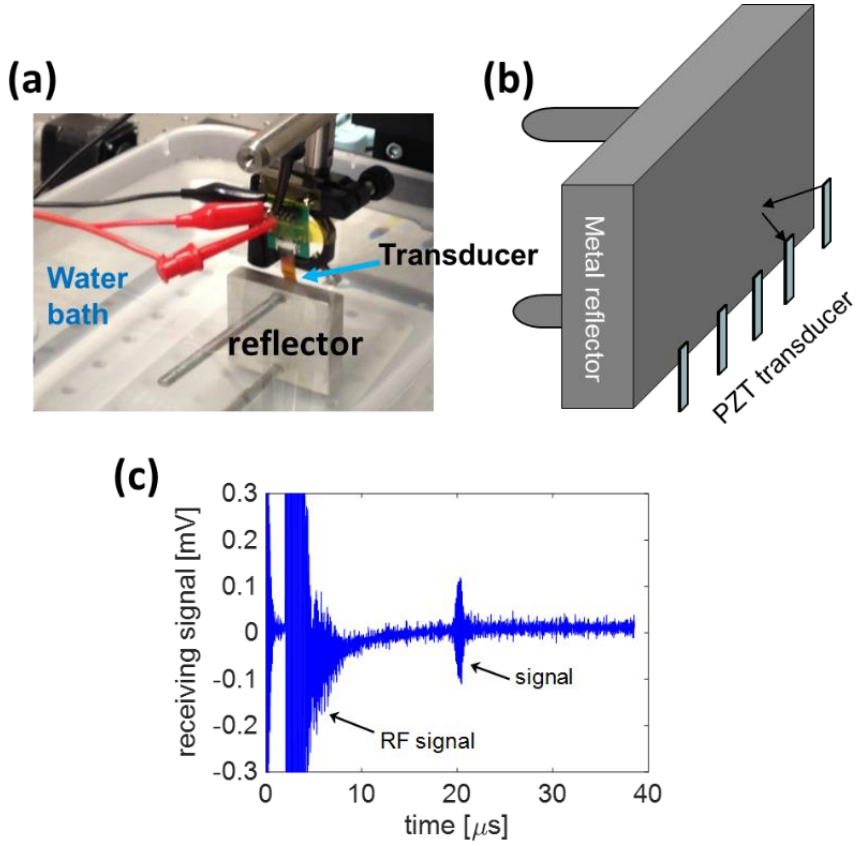

Figure 7-18. (a) and (b) Pitch-catch testing of two neighboring 100 µm × 1000 µm single elements respectively transmitting and receiving against a metal reflector. (c) The transmitting element was driven by a 5 V_p 5-cycle excitation and the receiving element detected a 0.2 mV signal before amplification.

The transmitting element was driven with a unipolar 5-cycle 5 V_p excitation. The reflected sound wave from the metal plate was then detected by the receiving element and measured by an oscilloscope as a 0.2 mV pre-amplified voltage signal shown in Figure 3-18 (c). By sweeping the driving frequency from 3 MHz to 40 MHz, the maximum signal amplitude was observed at 9.5 MHz, which was presumed to be the central frequency for the transducer element.

Using 4300 m/s as the approximate sound velocity [34], the estimated resonance frequency for a 100 µm-wide flexible thin-film PZT resonator is 21.5 MHz. The discrepancy is presumably a result of the

additional mass-loading and/or the frequency response of the test system. Considering the model of a simple harmonic vibration to a first approximation [35], the resonance frequency f_r can be written as

$$f_r = \frac{1}{2\pi}\sqrt{\frac{k}{m}}, \tag{4-2}$$

where *k* is the spring constant, and *m* is the mass. For the fabricated transducer element, the combined mass of the polyimide and the dense Pt contributed to approximately half of the total mass; this would lower the resonance frequency by a factor of ~1.4.

3.5.4 Sound pressure measurement

The sound pressure output and bandwidth were evaluated with a capsule-type hydrophone (HGL-0085, Onda Inc., Sunnyvale, California, USA) placed at 6 mm distance from the transducer elements. With a single element driven with 5 cycles of 5 V peak amplitude unipolar excitation, the hydrophone was able to detect a 1.6 mV signal with only the hydrophone's built-in amplifier (Figure 3-19 (a)). This voltage level corresponds to a 33 kPa sound pressure based on the hydrophone calibration data. Due to the novelty of the polymer substrate-based piezoelectric transducer, studies specifically on pressure output are not readily available in the literature. Comparison is therefore made with rigid substrate-based pMUT transducers, as shown in Table 3-3. The column for the normalized pressure output indicates that the transducers in this work achieved relatively high performance compared with similar devices within the last three years.

Table 7-3 Pressure output compared with rigid substrate-based pMUT devices.

Structure	Frequency	Pressure output	**Pressure output/ 1000 μm^2**	Distance	Driving voltage	source
PZT bar resonator	9.5 MHz	33 kPa	**0.33 kPa**	6 mm	5 V	this work
epitaxial PZT pMUT	8.5 MHz	6.3 kPa	**2.65 kPa**	where max output occurred	5 V	[36]
PZT pMUT	8 MHz	9.5 kPa	**0.16 kPa**	7.5 mm	5 V	[37]
AlN pMUT	20 MHz	25 kPa	**0.12 kPa**	0.8 mm	24 V	[10]

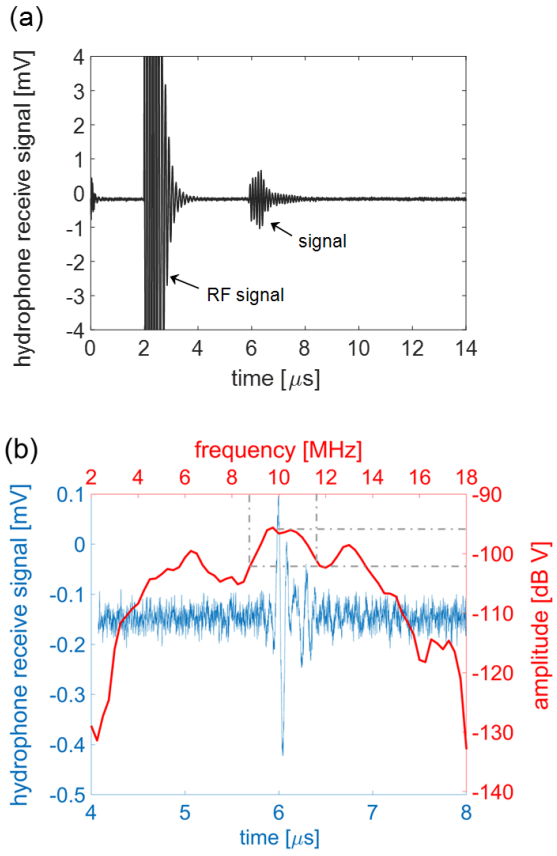

Figure 7-19. Hydrophone characterization of a 100 µm × 1000 µm single element driven with a 5 V_p sinusoidal excitation of positive polarity. (a) Hydrophone detection at 9.5 MHz with 5 cycles of excitation. The detected 1.6 mV corresponds to a 33 kPa sound pressure output. (b) Hydrophone detection of single cycle excitation and FFT calculation superimposed, showing a -6 dB bandwidth of ~32%.

Using the same electrical excitation but with one cycle burst at 9.5 MHz, bandwidth was calculated by converting the hydrophone-detected signal from time to frequency domain using a fast Fourier transform (FFT). Figure 3-19 (b) plots the received signal in both time and frequency domain and based on the latter, the bandwidth at -6 dB was 32%.

3.6 Chapter conclusions

Flexible polyimide substrate based ultrasonic transducers were demonstrated using 1 µm thick 700ºC crystallized lead zirconate titanate (PZT) films. They were single elements of bar resonators

targeted to operate in the width extension mode. The fabrication process employed the sacrificial layer release technique from Chapter 2 with a few additional and modified steps.

Bar resonator type transducers with 100 µm × 1000 µm and 25 µm × 500 µm single elements were initially fabricated on a thermally robust Si substrate with an underlying PEALD ZnO sacrificial layer. Then, upon deposition of the 5 µm spin-cast polyimide film, ZnO was dissolved in acetic acid to release and transfer the transducer devices from Si to polyimide. To prevent degradation in the PZT films caused by the imidization process, the precursor of polyimide was cured in an inert Ar ambient over a 40 nm Al_2O_3 barrier layer. Flexible ribbon cables were fabricated and bonded to the released transducers and inserted into a ZIF connector mounted on a printed circuit board for establishing external electrical connections.

The ability to transmit and receive acoustic signals in water was first confirmed with a 3.5 MHz commercial transducer. Then, pitch-catch was demonstrated with two 100 µm × 1000 µm neighboring elements respectively transmitting and receiving against a reflector at 1.5 cm distance. The element in receive detected a 0.2 mV pre-amplified signal for a driving frequency of 9.5 MHz. Characterization with a hydrophone evaluated a sound pressure output of these devices at 33 kPa and a -6dB bandwidth at 32%.

These are the first high-temperature crystallized thin-film PZT ultrasonic transducers transferred over large areas to flexible polymeric substrates. The development of flexible PZT devices provides a pathway for multiple applications that are not accessible by conventional bulk or rigid substrate thin-film devices.

3.7 Chapter reference

[1] N. G. Pandian, A. Weintraub, S. L. Schwartz, R. Kumar, B. S. Kusay, S. E. Katz, M. Aronovitz, J. Udelson, M. A. Konstam, D. N. Salem, and A. Kreis, "Intravascular and intracardiac ultrasound imaging: current research and future directions," *Echocardiography*, vol.7, no.4, pp. 377-287, 1990

[2] F. L. Degertekin, R. O. Guldiken, and M. Karaman, "Annular-ring CMUT arrays for forward-looking IVUS: Transducer Characterization and Imaging," *IEEE Trans, Ultrason., Ferroelect., Freq. Contr.*, vol. 53, pp.474-482, 2006

[3] X. Zhuang, D. S. Lin, O. Oralkan, "Fabrication of flexible transducer arrays with through-wafer electrical interconnects based on trench refilling with PDMS," *J. Microelectromechanical Sys.*, vol. 17, no. 2, pp. 446 – 452, 2008

[4] J. Schulze-Clewing, M. J. Eberle, and D. N. Stephens, "Miniaturized circular array," in *Proc. IEEE Ultrason. Symp.*, 2004, Montreal, Canada, pp.384-390

[5] W. C. Black and D. N. Stephens, "CMOS Chip for Invasive Ultrasound Imaging," *IEEE J. Solid-State Circuits*, vol. 29, no.11, pp.1381 – 1387, 1994

[6] J. Hashimoto, "Finger vein authentication technology and its future," in *IEEE Symp. VLSI Circuits, Digest of Technical Papers.*, pp. 5-8, 2006

[7] M. Kono, H. Ueki, and S. Uemura, "Near-infrared finger vein patterns for personal identification," *Appl. Optics*, vol. 41, pp. 7429 – 7436, 2002

[8] Y. Lu, H. Tang, S. Fung, Q. Wang, J. M. Tsai, M. Daneman, B. E. Boser, and D. A. Horsley, "Ultrasonic fingerprint sensor using a piezoelectric micromachined ultrasonic transducer array integrated with complementary metal oxide semiconductor electronics," *App. Phys. Lett.* vol. 106, pp. 263503, 2015

[9] Y. Lu, and D. A. Horsley, "Modeling, fabrication, and characterization of piezoelectric micromachined ultrasonic transducer arrays based on cavity SOI wafers," *J. Microelectromech. Sys.*, vol. 24, No. 4, pp 1142 – 1149, 2015

[10] X. Jiang, H-Y. Tang, Y. Lu, E. J. Ng, J. M. Tsai, B. E. Boser, and D. A. Horsley, "Ultrasonic fingerprint sensor with transmit beamforming based on a PMUT array bonded to CMOS circuitry," *IEEE Trans. UFFC*, vol. 64, no. 9, pp. 1401-1408, 2017.

[11] Y. Kato, T. Sekitani, Y. Noguchi, T. Yokota, M. Takamiya, T. Sakurai, and T. Someya, "Large-area flexible ultrasonic imaging system with an organic transistor active matrix," *IEEE Transactions on Electron Devices*, vol. 57, no. 5, pp. 995-1002, 2010.

[12] L. F. Brown and J. L. Mason, "Disposable PVDF ultrasonic transducers for non-destructive testing applications," *IEEE Trans. Ultrason., Ferroelectr., Freq. Contr.*, vol. 43, no. 4, pp. 560–568, 1996.

[13] A. Ambrosy and K. Holdik, "Piezoelectric PVDF films as ultrasonic transducers," *J. Phys. E: Sci. Instrum.* vol.17, no. 10, pp.856-859, 1984

[14] M. D. Sherar and F. S. Foster, "The design and fabrication of high frequency poly(vinyldene fluoride) transducers," *Ultrason. Imag.*, vol. 11, pp. 75-94, 1989.

[15] L. F. Brown, J. L. Mason, D. Khataniar, J. I. Scheinbeim, and B. A. Newman, "Ferroelectric Nylon-7, -11 ultrasonic transducer performance," *IEEE Ultrasonics Symposium*, pp.1255-1258, 1995

[16] P. Marin-Franch, I. Pettigrew, M. Parker, K. J. Kirk, and S. Cochran, "Piezocrystal-polymer composites: New materials for transducers for ultrasonic NDT," *Insight-Non-Destructive Testing and Condition Monitoring*, vol. 46, no. 11, pp. 653–657, 2004.

[17] M. Akhnak, O. Martinez, L. G. Ullate, and F. Montero de Espinosa, "64 Elements two-dimensional piezoelectric array for 3D imaging," *Ultrasonics*, vol. 40, pp. 139-143, 2002

[18] G. Harvey, A. Gachagan, J. W. Mackersie, T. McCunnie, and Robert Banks, "Flexible ultrasonic transducers incorporating piezoelectric fibers," *IEEE Trans. Ultrason., Ferroelectr., Freq. Contr.*, vol. 56, no. 9, pp. 1999-2009, 2009.

[19] N. Bu, N. Ueno, and O. Fukuda, "Monitoring of respiration and heartbeat during sleep using a flexible piezoelectric film sensor and empirical mode decomposition," *Proceedings of the 29th Annual International Conference of the IEEE EMBS*, Lyon, France, pp 1362-1366, 2007

[20] J. N. Kim, "Closed-loop finite element design of array ultrasonic transducers for high frequency applications," Ph.D. thesis, The Pennsylvania State University, University Park, PA 2019

[21] K. Uchino, "Piezoelectric Devices" in *Ferroelectric Devices*, CRC Press, Taylor & Francis Group, Boca Raton, FL, 2010, pp. 161-232

[22] Y. Shibayama, M. Saito, "Influence of water on photochemical reaction of positive-type photoresist," *Japanese Journal of Applied Physics*, vol. 29, no. 10, pp. 2152-2155, 1990

[23] O. P. Lehar, M. A. Spak, S. Meyer, R. R. Dammel, C. J. Brodsky, and C. G. Willson, "Resist rehydration during thick film processing," in *Advances in Resist Technology and Processing XVIII*, vol. 4345, pp. 463-474. International Society for Optics and Photonics, 2001.

[24] K. Kushida-Abdelghafar, H. Miki, K. Torii, and Y. Fujisaki, "Electrode-induced degradation of $Pb(Zr_x,Ti_{1-x})O_3$ (PZT) polarization hysteresis characteristics in Pt/PZT/Pt ferroelectric thin-film capacitors," *Appl. Phys. Lett.*, vol. 69, no.21, pp 3188-3190, 1996

[25] P. D. Maniar, R. Moazzami, R. E. Jones, A. C. Campbell and C. J. Mogab, "Impact of backend processing on integrated ferroelectric capacitor characteristics," in *Mater. Res. Soc. Symp. Proc.*, vol. 310, pp.151-156, 1993

[26] J-M. Koo, T. Kim, and J. Kim, "Hydrogen induced degradation phenomena of PZT ferroelectric capacitors," in *Proceedings of the 2000 12th IEEE International Symposium on Applications of Ferroelectrics*, vol. 2, pp. 591-594, 2000

[27] H. Miki, K. K. Abdelghafar, K. Torii, and Y. Fujisaki, "Hydrogen-related degradation and recovery phenomena in Pb(Zr, Ti)O_3 capacitors with a platinum electrode," *Jpn. J. Appl. Phys.*, vol. 36, no. 3A, pp. 1132, 1997

[28] E. M. Petrie, "Handbook of adhesives and sealants – basic concepts and high tech bonding," McGraw-Hill, 2000, pp. 439-440

[29] J. C. Coburn, and M. T. Pottiger, "Thermal curing in polyimide films and coatings," in *Polyimides Fundamentals and Applications*, M. Ghosh and K. Mittal, Eds., New York, NY, Marcel Dekker Inc., 1996, pp. 207.

[30] S-M. Chang, J-H. Jou, A. Hsieh, T-H Chen, C-Y Chang, Y-H Wang, and C-M Huang, "Characteristic study of anisotropic-conductive film for chip-on-film packaging," *Microelectronics Reliability*, vol. 41, pp. 2001-2009, 2001

[31] N. Takano, T. Fujinawa, and T. Kato, "Film technologies for semiconductor & electronic components," *Hitachi Chemical Technical Report*, vol. 55, no. 5, pp. 20-23, 2013

[32] M. Shiiki, J. Imaizumi, T. Miyata, and A. Chinda, "Materials and components for flat panel display applications," *Hitachi Review*, vol. 55, no. 1, pp. 32-39, 2006

[33] *PI-2600 Series – Low Stress Applications*, HD MicroSystems, Parlin, NJ, USA, 2009

[34] T. Ogawa, "Acoustic wave velocity measurement on piezoelectric ceramics," in *Piezoelectric materials and devices-practice and application*, Intech Open Access Publisher, Croatia, pp. 35-52, 2013

[35] L. E. Kinsler, A. R. Frey, A. B. Coppens, and J. V. Sanders, "Fundamentals of vibration," in *Fundamentals of Acoustics*, John Wiley & Sons, Inc., pp. 2-4, 1982

[36] Z. Liu, S. Yoshida, T. Horie, S. Okamoto, R. Takayama, and S. Tanaka, "Characterization of epitaxial-PZT/Si piezoelectric micromachined ultrasonic transducer (pMUT) and its phased array system," in *International Conference on Solid-State Sensors, Actuators and Microsystems & Eurosensors XXXIII*, pp. 246-249, 2019

[37] C. Y. Cheng, A. Dangi, L. Ren, S. Tiwari, R. R. Benoit, Y. Qiu, H. S. Lay, S. Agrawal, R. Pratap, S-R. Kothapalli, T. E. Mallouk, S. Cochran, and S. Trolier-McKinstry, "Thin film PZT-based PMUT arrays for deterministic particle manipulation," *IEEE Trans. Ultrason., Ferroelectr., Freq. Contr.*, vol. 66, no. 10, pp. 1606-1615, 2019

Chapter 4. d_{33} measurements in released PZT films by DBLI

4.1 Introduction and background

Substrate-clamping is one of the major sources that cause lower piezoelectric and dielectric responses in PZT films relative to their bulk counterparts due to a restricted in-plane deformation and reduced non-180° domain wall motion [1, 2]. There is abundance of reports demonstrating improved domain reorientation and enhanced piezoelectric responses for locally released thin-film PZT structures as a result of reduced substrate-clamping. For example, an increase in the piezoelectric constant was observed for PZT films patterned into islands with lateral dimensions on the same order as the film thickness [3-5]. The increase was also reported for de-clamped PZT films through the use of a diaphragm structure [6]. Wallace *et al.* demonstrated improved piezoelectric responses in locally de-clamped PZT films through quantification of 90° domain reorientation using *in situ* X-ray diffraction. In their work, de-clamping of the PZT film was achieved via creating etch pits to the underlying Si substrate; by changing the spacing between the etch pits on each electrode, the degree of release state was controlled. A systematic increase in the 90° domain reorientation was observed for increasing degree of release; for a 75% locally released state, the volume fraction of reoriented domains approached the values measured in bulk ceramics [7].

Substantially enhanced electrical properties were observed in fully released PZT films on polyimide (Chapter 2), it is intriguing to see how the piezoelectric responses evolve for these films. Understanding both the electrical and piezoelectric responses in the released state is important for the development of flexible piezoelectric devices and piezoelectric-micro-electromechanical-systems (piezoMEMS).

Despite the maturity of instrumentation for measuring the piezoelectric responses of films on a rigid substrate, there is little literature available on how to best quantify the piezoelectric coefficient for films on flexible polymeric substrates. In this work, evaluation of the longitudinal piezoelectric

coefficient, d_{33}, was attempted in PZT thin-films on flexible polyimide substrates using a commercial double-beam laser interferometer (DBLI).

4.1.1 The longitudinal piezoelectric coefficient

The piezoelectric coefficient, *d*, links the applied stress linearly to the induced polarization for the direct piezoelectric effect, or, associates the applied electric field to the proportionally induced strain for the converse piezoelectric effect [8]. This is described in Equations 4-1 and 4-2:

$$D = dT \tag{4-1}$$

$$x = dE \tag{4-2}$$

where *D* is the dielectric displacement (charge per unit area), *T* is the stress, *x* is the strain, and *E* is the electric field. The direct and converse d coefficients are numerically identical for a mechanically free sample.

In order to describe the anisotropy of piezoelectric materials, the above relationships are often represented in a tensor format, as shown in Equations 4-3 and 4-4.

$$D_i = d_{ijk} T_{jk}, \tag{4-3}$$

$$x_{ij} = d_{kij} E_k, \tag{4-4}$$

with *i*, *j*, and *k* =1,2,3.

The notation d_{33} is the reduced tensor representation of d_{333} with the second and the third suffix collapsing to a single "3". For ceramics or oriented films, the 3-direction is defined as the poling direction while 1 and 2 are orthogonal directions in the plane normal to 3. Hence, the "33" of d_{33} indicates that the electrical field (or the generated charge) and the coupled mechanical strain (or the applied stress) are both along the polarization direction. For instance, for films poled in the thickness direction, the "3" direction represents the film normal [9]. For piezoelectric thin-films grown on a rigid substrate, $d_{33,f}$ defines the effective longitudinal piezoelectric coefficient due to the non-zero applied in-plane stress T_1 and T_2 as a

result of substrate-clamping [10]. To derive the expression for $d_{33,f}$ based on the converse piezoelectric effect, one can use the relationship in Equation 4-5 as the change of strain per change of electric field,

$$d_{33} = (\frac{\partial x_3}{\partial E_3})_T, \tag{4-5}$$

where the subscript T indicates that the relationship is valid under the constant stress condition. Combining the electromechanical and the mechanical term and assuming zero for the shear terms, the strain in the 3 direction can be written as [10]:

$$x_3 = d_{33}E_3 + s_{13}^E T_1 + s_{23}^E T_2 + s_{33}^E T_3, \tag{4-6}$$

where s^E is the elastic compliance of PZT under constant electric field and T_3 is the out-of-plane stress. As the film is free to move in the 3 direction, T_3 can be set to 0. And as poled PZT has ∞mm symmetry, $s_{13}^E = s_{23}^E$. Hence, Equation 4-6 can be reduced to:

$$x_3 = d_{33}E_3 + s_{13}^E(T_1 + T_2). \tag{4-7}$$

Bringing Equation 4-7 back to Equation 4-5, the effective $d_{33,f}$ for piezoelectric films is therefore:

$$d_{33,f} = \frac{x_3}{E_3} = d_{33} + s_{13}^E(T_1 + T_2)/E_3. \tag{4-8}$$

In this equation, as s_{13}^E has a negative value, the longitudinal piezoelectric coefficient for films is by default smaller than the bulk counterpart, since the boundary conditions for a bulk material are free in all three directions (T_1=T_2=T_3=0). For PZT films released from Si and transferred onto a thin polyimide substrate, the applied stress term, T_1+T_2, should become lower as the PZT layer experiences a less in-plane clamping force from the rigid substrate. A significant increase is therefore anticipated for the piezoelectric coefficient $d_{33,f}$, and the value should approach d_{33} of a bulk ceramic of the same composition.

4.1.2 A survey of measurement approaches

A variety of testing methods have been developed to evaluate the d_{33} or the $d_{33,f}$ piezoelectric coefficient.

Piezoresponse force microscope (PFM) is a widely employed technique for measuring the piezoelectric coefficient using the converse piezoelectric effect; this method is capable of achieving nanometer-scale lateral resolution and picometer-scale vertical resolution [11-14]. Two modes are generally used by the PFM measurement approach: (1) local excitation and (2) global excitation. In the local excitation mode, a conductive tip contacts the sample surface to apply an alternating voltage and measure the locally induced strain. Because the contact area is extremely small (diameter ~25 nm) and the film is grown on a large-area bottom electrode, the electric field distribution is inhomogeneous. This, combined with the unknown field drop across air gap or moisture contact between the film and the probe tip means that a quantitative measurement is infeasible. In addition, the contact force, as well as the lack of activation of the surrounding material partially clamps the piezoelectric response, causing a ~30% error [14-16]. Some of the inaccuracy is mitigated in the global excitation regime as the probe tip is in contact with a top electrode deposited on the film. The top electrode globally excites a large volume of material with a uniform and known electric field. However, a frequency-dependent, system-inherent transfer function of the scanner system, along with the introduction of sample bending still prevents accurate piezoelectric coefficient measurements [15, 16].

Alternative techniques based on optical interference for d_{33} and $d_{33,f}$ measurements include: (1) homodyne laser interferometry in either a single or a double (DBLI) testing beam configuration [17-20], and (2) heterodyne interferometry, such as laser Doppler vibrometry (LDV) [21, 22].

In a single-beam homodyne laser interferometry system, a laser source is divided into a reference beam and a measurement beam. The measurement beam is reflected from the sample surface, and then interfered with the reference beam. The intensity of the interference pattern is then measured by a photodetector. Any changes in the height of the sample will alter the path length of the measurement beam, thus changing the intensity. The sample displacement under an applied electric excitation is quantified based on the intensity change, as Equation 4-9 shows [17].

$$I = \frac{1}{2}(I_{max} + I_{min}) + \frac{1}{2}(I_{max} - I_{min})\cos\left(2\pi\frac{2\Delta t}{\lambda} + \frac{\pi}{2}\right), \quad (4\text{-}9)$$

where Δt is the sample thickness change, λ is the laser wavelength, and I_{max} and I_{min} are the maximum and minimum intensity of the center value of the interference pattern.

Interference monitoring is also used in the LDV method, where the sample movement is measured based on the Doppler effect, *i.e.* the frequency shift of the measurement beam.

The two interferometry methods described above only probe the thin-film sample with a single laser beam on one of the displaced surfaces, which does not account for the substrate bending contribution in piezoelectric films on a rigid substrate. As a result, large apparent d_{33} values are measured. There are, however, exceptions that result in negligible substrate bending. As finite element analysis (FEA)-simulated and experimentally verified by Pepadatu *et al.*, for 100 nm thick PZT films on 400 µm thick STO substrates, bending was suppressed by using top electrodes with a diameter less than 100 µm [22]. However, Shetty *et al.* demonstrated that bending could be observed even when the top electrode is substantially smaller than the substrate thickness [5]. A more effective way of compensating the bending contribution entails using two laser beams to probe both top and bottom sample surfaces. In a Mach-Zender double-beam interferometer (DBLI), the bending contribution is eliminated as the path length of the two measurement beams cancels each other. Using DBLI to measure electric field induced strains in bulk piezoelectric ceramics was first demonstrated by Zhang *et al.* [24] and in ferroelectric films by Kholkin *et al.* [17]

Although the bending contribution is compensated by the DBLI approach, there is another substrate contribution due to a convoluted in-plane and out-of-plane stresses exerted by the piezoelectric film under excitation. The applied stresses cause a thickness change in the substrate, which is added to the intensity change of the interference pattern, thus making the d_{33} results less accurate [23]. Sivaramakrishnan *et al.* qualitatively demonstrated that the polarity and the magnitude of this contribution are a function of the lateral dimension of the top electrode, and the contribution vanishes when the top electrode has the lateral dimensions equal to the substrate thickness, as the thickness changes from the in-plane and out-of-plane stresses are canceled by each other.

Custom-designed and -modified methods have also been reported. For example, Shetty *et al.* developed a modified Mirau interferometer microscope with a lock-in phase detection regime [5]. The system was able to achieve a ~2 μm spatial resolution and ~5 pm vertical resolution over a frequency range of 2 Hz – 2 kHz for localized $d_{33,f}$ measurements on patterned piezoelectric films.

Techniques based on the direct piezoelectric effect are more commonly used for evaluating d_{33} coefficients of bulk ceramics, such as the Berlincourt method [25]. For thin films, Xu *et al.* designed and constructed a custom pneumatic pressure rig that measured d_{33} and $d_{33,f}$ for bulk and thin-film PZT by monitoring the charges generated by a known stress [26]. Uniform pressure application to the sample was achieved by feeding high-pressure nitrogen gas into two O-ring-sealed cavities above and below the sample. The generated charges were evaluated with a charge integrator. The obtained d_{33} and $d_{33,f}$ values were in good agreement with measurements made with a Berlincourt meter and a DBLI, respectively.

4.1.3 aixACCT DBLI system

The instrument used for the d_{33} measurements in this work is an aixACCT DBLI system (aixACCT GmbH, Aachen, Germany) equipped with a 632.8 nm He-Ne laser. It has a vertical resolution of ~1 pm for a measurement range of 5 pm to ~25 nm.

A simplified schematic of the system is illustrated in Figure 4-1 [27]. The main optical components used to construct the system include an isolator, a photodiode, polarizing beam splitter (PBS), beam splitter (BS), λ/2 wave plates, λ/4 wave plates, a piezo reference mirror, and reflecting mirrors. A polarized laser beam from the source passes through an isolator and is reflected from a mirror to travel through a λ/2 plate. Then, the beam continues to the polarizing beam splitter PBS1, from which the transmitted beam is used as the measurement beam, and the reflected beam is used as a reference beam.

The measurement beam passes the λ/4 plate P2, and impinges on the sample's top surface. The reflected beam from the top surface returns to the beam splitter PBS1, by which is reflected towards

another splitter PBS2. The subsequent beam then travels to probe the bottom surface of the sample and eventually arrives at the beam splitter BS.

The reference beam is reflected towards PBS3 and then a reference mirror (piezo-mirror), which serves to stabilize the working point of the interferometer and performs the calibration. Next, the reference beam passes through PBS3 again and arrives at BS, where it meets the measurement beam of the same polarization and forms an interference pattern.

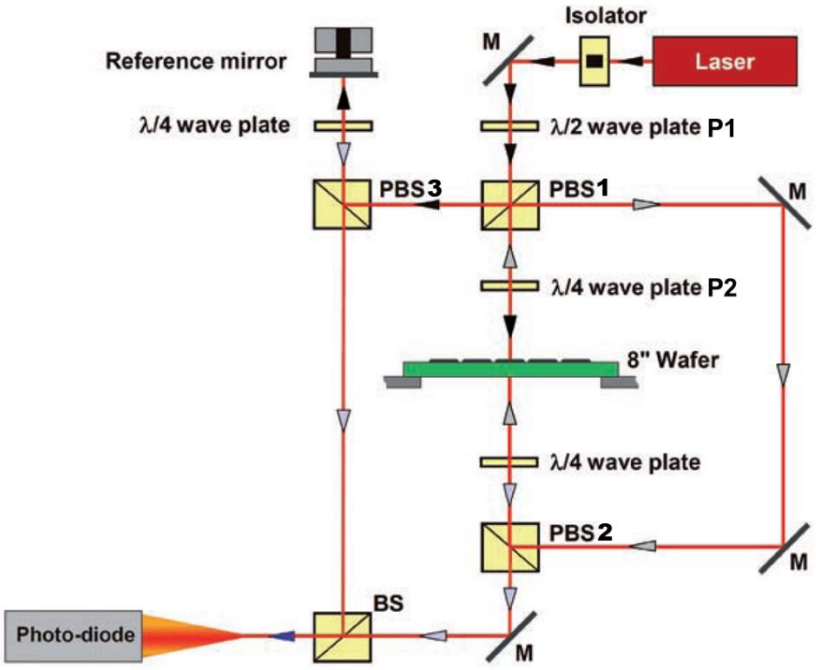

Figure 8-1. A simplified schematic of the aixACCT DBLI system. Figure is reproduced from [27].

The intensity of the interference is a function of the thickness displacement, as described earlier in Equation 4-9. The bending contribution is eliminated by the cancellation of the optical pathlength change of the two beams as shown in Figure 4-2. The dimensions are exaggerated for demonstration purposes. In panel (a), when the sample (thickness = t) is in focus without electrical excitation, the total pathlength for the closed laser loop is $2L_{top} + L_2 + L_3 + L_4 + 2L_{bot}$, where L_{top} and L_{bot} are accounted twice as the beam is reflected from the sample surfaces. Neglecting the thickness change of the substrate, when the sample is driven with an electric field parallel to the polarization direction, as Figure 4-2 (b) shows, it

elongates along the thickness direction by Δt and bends downward by a distance b. In this case, the pathlength for the top beam segment is $2L_{top}+2b$ while for the bottom beam segment is $2L_{bot}-2\Delta t-2b$. Combining with L_2, L_3, and L_4, the total pathlength of the loop is therefore

$$2L_{top} - 2\Delta t + L_2 + L_3 + L_4 + 2L_{bot},$$

where the $+2b$ and $(-2b)$ terms are cancelled, and the change in the pathlength is simply $2\Delta t$.

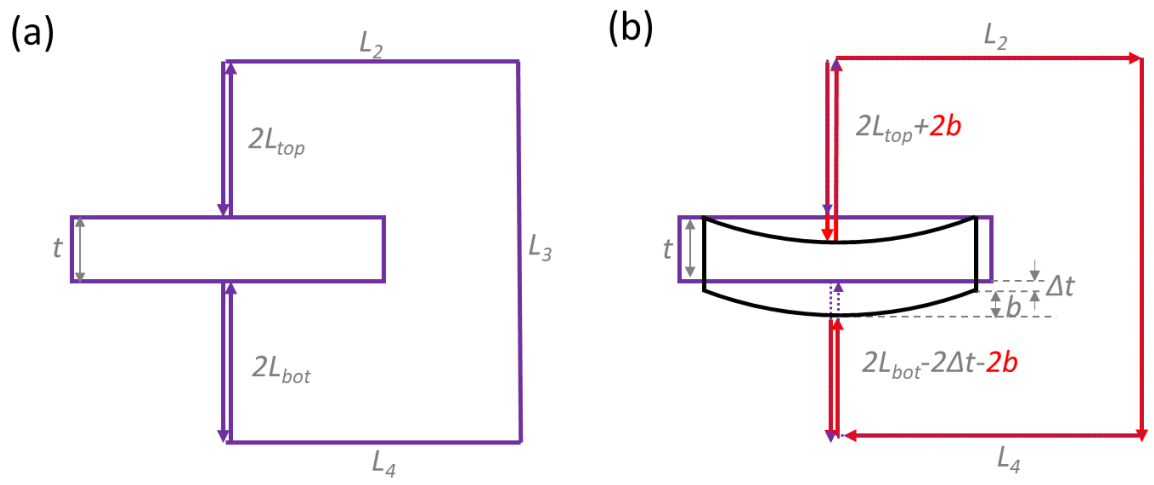

Figure 8-2. (a) The laser pathlength looping from the top to the bottom surface of a static sample with thickness t. (b) Under electrical excitation, the thickness elongates by Δt and the sample bends by a distance of b. The bending term b is cancelled for the total loop pathlength when summing the top and bottom segments with L_2, L_3, and L_4; the pathlength change due to d_{33} is only a function of the thickness displacement Δt.

The aixACCT DBLI system is equipped with a ring chuck and a squared frame chuck to hold the samples so that the bottom surface is exposed for laser-probing. The ring chuck is designed to hold 6'' diameter wafers; the 2.5 cm × 2.5 cm square chuck is for holding small sample pieces. Needle-probes on micromanipulators are employed to make electrical connections with the samples. The laser beam and probe positions are controlled by moving an X-Y linear stage and visualized by a camera.

4.2 Sample testing configuration

4.2.1 Sample design

The test samples adapted the basic PZT-on-polyimide structure described in Chapter 2. They were 1 μm thick blanket $Pb(Zr_{0.52}Ti_{0.48})_{0.98}Nb_{0.02}O_3$ films on 11 μm thick polyimide substrates with a blanket bottom Pt electrode and patterned top Pt electrodes. The polyimide layer was patterned to facilitate direct laser probing on the top and the bottom electrodes. Because the samples were held by the frame-chuck on the DBLI system, the released stack was adhered to a rigid backing for structural support. Self-supporting on the frame-chuck without crumpling and falling through is infeasible for the thin polyimide. Holes were also punched in the backing as well as the adhesive agent to allow the laser beam to pass through. A 1 mm thick polycarbonate was chosen as the backing and the adhesive agent was a double-sided tape. The sample structure is schematically illustrated in Figure 4-3.

The top electrode was patterned into circles of diameters ranging from 400 μm to 800 μm. Most circles were designed with an extension tab, which was originally intended for placing the electrical needle-probe with adequate clearance from the laser spot. It was found that the needle probes could not be used successfully because (1) the released sample would be mechanically deformed and deflect the laser beam to result in loss of optical signal, and (2) the physical contact between the probe and the flexible sample was unreliable, resulting in loss of electrical signal as soon as the sample began to actuate. Thus, the tab was used instead as a make-shift extension bonding pad for attaching flexible ribbon cables. The top electrodes are the red-colored pattern in Figure 4-3 (b). The smaller blue concentric circle indicates the etched polyimide window on the backside of the released structure. The diameter of the circular etch window was either 1/2 or 2/3 of the PZT diameter; the polyimide at the perimeter was intended to support the fragile Pt/PZT/Pt membrane and reduce breakage. Unfortunately, it also introduced added structural asymmetry – a source for undesirable excessive bending. The associated measurement errors are discussed in detail in Section 4.3.3. The electrodes without the blue concentric circles in Figure 4-3 (b) are the ones with the polyimide unetched on the backside, which are reserved for studying the impact of laser-signal acquirement through a non-air medium.

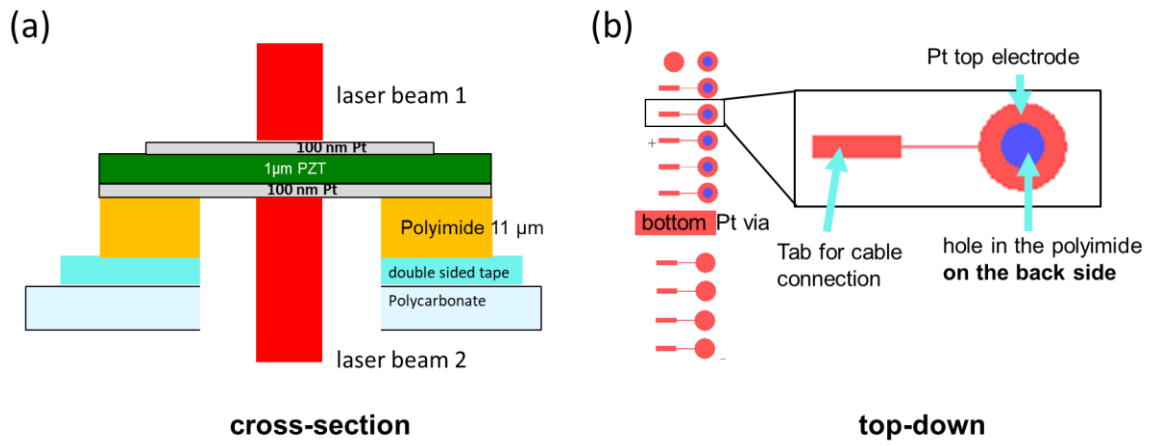

Figure 8-3. (a) Cross-sectional schematic of the testing sample. The two laser beams probe directly the top and bottom Pt electrodes. (b) Top-down view of the sample schematic, where the top electrodes are red circles with extension tabs and the blue concentric circles are the holes etched in the polyimide layer.

The probing position of the laser beam is crucial for obtaining correct measurement results. Two potentially incorrect scenarios are examined below.

For the first incorrect scenario, as illustrated schematically in Figure 4-4 (left), if the polyimide on the bottom of the substrate was unpatterned and metallized at the surface (e.g., Ti) to reflect the bottom laser beam, there would be a significant contribution from the thickness and geometry change of the polyimide layer as a result of PZT actuation, comparable to the effect described by Sivaramakrishnan *et al.* for PZT films on Si. [23].

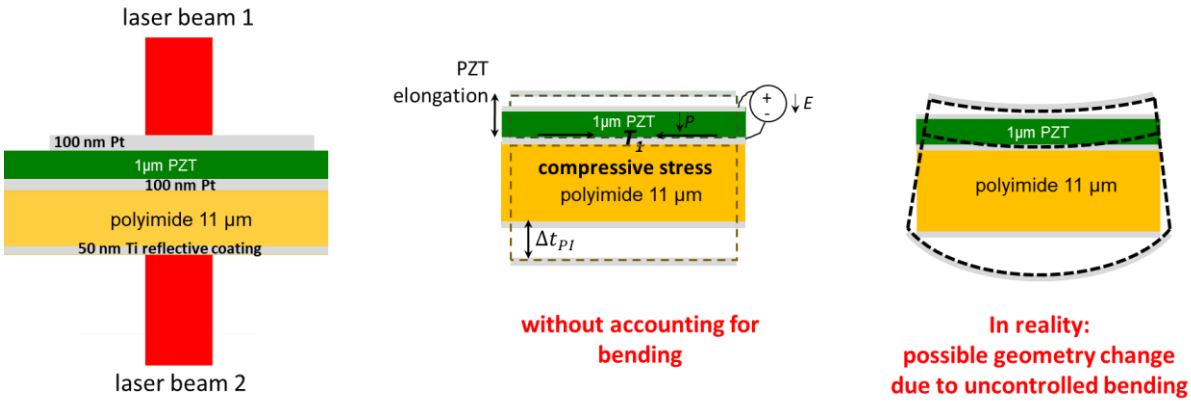

Figure 8-4. If the polyimide is unpatterned and the laser beam is reflected from the metallized polyimide surface, the measured d_{33} will be inaccurate as there is a significant contribution from the thickness combined with an uncontrolled geometry change of the polyimide layer due to PZT actuation.

As an electric field is applied to the PZT along the poling direction, the PZT elongates vertically and shrinks laterally, exerting a compressive stress T_1 to the polyimide near the interface (middle panel of Figure 4-4). The induced strain in the polyimide in the "3" direction can be expressed as:

$$x_3 = \frac{e_{31,f} E_3}{Y_{PI}} \upsilon_{PI}, \tag{4-10}$$

where $e_{31,f}$ is the transverse piezoelectric coefficient, Y_{PI} is the Young's modulus of the polyimide, υ_{PI} is the Poisson's ratio of polyimide. This strain is significant relative to that in the PZT layer as the Young's modulus of polyimide is 10 times lower than PZT (8.5 GPa for PI-2611 [28], and 80-100 GPa for PZT [29]). Using typical values from Table 4-1 for the other parameters in Equation 4-10, the estimated strain in the 3-direction under a 100 kV/cm field gives 0.14% in PZT and 0.3% in polyimide.

Table 8-1. PZT and polyimide properties for strain estimation.

Property	Value	Reference
$d_{33,f}$ of PZT	140 pm/V	[20]
$e_{31,f}$ of PZT	-10 C/m^2	[30]
s_3 of polyimide	0.12×10^{-9} m/N	[28]
Poisson's ratio of polyimide	0.34	[31]

It is to be noted that this estimated strain in polyimide is qualitative and the associated thickness change cannot accurately represent the actual displacement measured by the laser beam. The actual displacement of the polyimide is largely influenced by an uncontrolled bending motion as well as the relative position of the laser incidence on the sample. The degree of bending also varies with factors such as mechanical compliance and top electrode dimensions. A more quantitative and comprehensive geometry analysis would require more sophisticated finite element modeling, as reported by Sivaramakrishnan *et al*. However, it was concluded in the article that for a top electrode larger than the substrate thickness (as for the case in this work), less stiff (lower Young's modulus) substrates will produce a more significant error contribution. That is, the less stiff polyimide is expected to undergo more

thickness elongation than Si and other rigid substrates of similar Young's moduli. For these reasons, the geometry change in the polyimide due to PZT actuation should be closer to what is illustrated in the right-panel schematic in Figure 4-4, and the magnitude of the detected displacement should be larger than the more ideal approximation in the middle-panel schematic. The difficulty in quantifying this change makes error-compensation difficult.

For the second incorrect scenario, if the polyimide substrate remained as a blanket layer, as shown in Figure 4-5, there would be a significant false contribution to the pathlength change of the measurement beam resulting from the difference in the refractive index of polyimide from air. When the laser arm passes through the polyimide and is reflected from the bottom Pt, it experiences a reduction in its wavelength as it travels from air (n≈1.0) into the polymeric medium with a higher refractive index (*n*≈1.7 [32]). The smaller wavelength will cause the laser beam to have a longer pathlength within the polyimide layer as opposed to propagating through air. This inflation cannot be directly compensated by the measurement system as it is a non-static contribution due to uncontrolled geometry change of the polyimide and the uncertain laser incidence position, as discussed in the previous section and presented as *p(t)* in the right-panel schematic of Figure 4-5. But it is certain that the uncompensated pathlength error would result in inflated displacement detection and subsequently, erroneous d_{33} values.

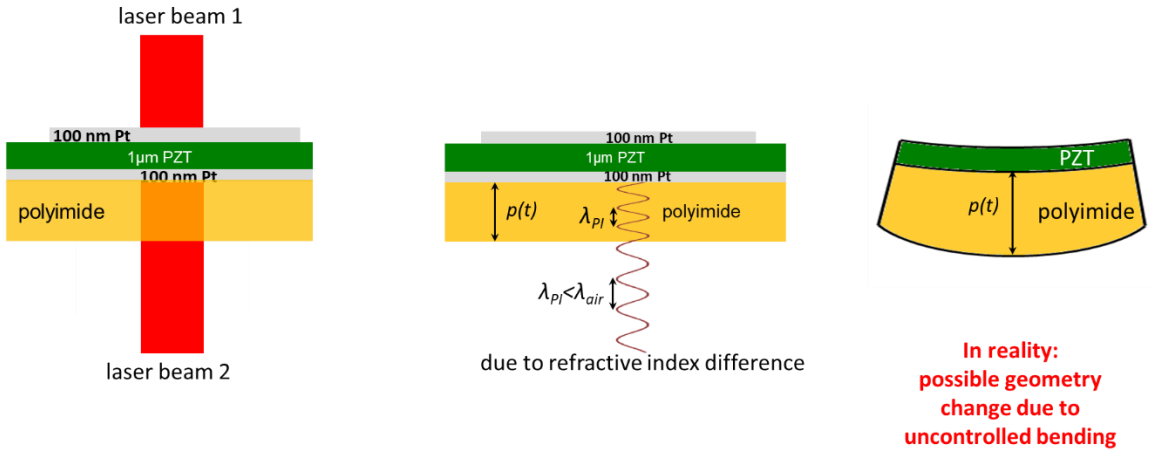

Figure 8-5. If the backside polyimide is unpatterned and the optical signal is acquired through the polyimide, an incorrect pathlength contribution is resulted from the refractive index difference between air and polyimide.

This error may have contributed to the large apparent d_{33} values measured on released thin film $(1-x)Pb(Mg_{1/3}Nb_{2/3})O_3$-$xPbTiO_3$ (PMN-PT) on blanket polydimethylsiloxane (PDMS) substrates using the DBLI approach [33]. After transferring PMN-PT films from Si to a PDMS layer while being supported by glass (Figure 4-6 (a)), the d_{33} coefficient was reported with a dramatic increase from ~11 pm/V to ~1000 pm/V at 100 kV/cm for a PMN-0.6PT film, as shown in panel (b). While there is expected to be a finite improvement in the piezoelectric response on release, it is also possible that the effect is artificially inflated as a result of the time-variant pathlength change as the laser beam propagated through the geometry-varying PDMS.

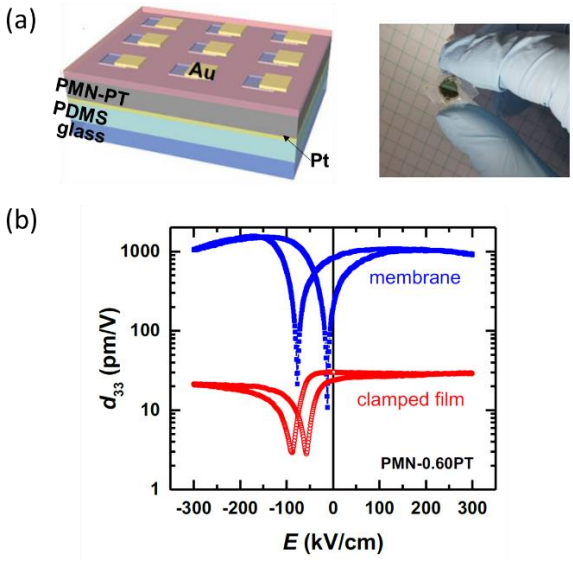

Figure 8-6. (a) Schematic of the PMN-PT structure released on PDMS (left) and an actual image of the sample (right). (b) 100 times higher d_{33} was observed for the PMN-PT films on PDMS using a DBLI system. The large apparent coefficient is due to the incorrect assumption that the pathlength is unaltered as it propagates through the glass and PDMS and partially reflected from the interfaces of glass/PDMS and air/glass. Figure adapted from [33].

4.2.2 Sample fabrication

The processing techniques used in fabricating the DBLI testing samples, such as ACF bonding, photolithography, polyimide substrate integration, release, along with all the deposition methods, are discussed in greater details in Chapter 2 and 3. The processing steps in this chapter are therefore described in a summary manner.

On a clean 100 mm Si wafer with a 10,000 Å thick thermal oxide layer, a 100 nm thick ZnO sacrificial layer and a 10 nm thick Al_2O_3 diffusion barrier layer were deposited in a custom-built PEALD system at 200°C. The metalorganic precursors used for growing the oxide layers were DEZ for ZnO and TMA for Al_2O_3; the oxidant gases were N_2O for ZnO and CO_2 for Al_2O_3. Next, a 100 nm thick Pt layer was deposited on the Al_2O_3 at room temperature in a DC magnetron sputtering system and patterned lithographically by lift-off to form the first electrode layer, which would become the top electrode upon release. This layer adopted the pattern shown in Figure 4-3 (b), consisting of circles from 400 µm to 800 µm in diameter and the extension tabs for cable-bonding.

PZT thin-films with a composition at the morphotropic phase boundary with 2% Nb doping were deposited over the patterned platinum electrodes via a sol-gel route. 15wt% Mitsubishi E1 PZT solution (Mitsubishi Materials Corporation, Japan) was statically dispensed onto the substrate and spin cast at 2750 RPM for 40 seconds followed by a hotplate bake at 100ºC for 1 minute to remove the carrier solvent, before a hotplate pyrolysis at 300ºC for 4 minutes. It was then crystallized in the AccuThermo AW 810 rapid thermal annealing (RTA) system at 700ºC for 1 minute in air. As a single deposition layer yields a thickness of ~90 nm, these steps were repeated 12 times to reach a desired thickness of ~1 µm. A 0.08M PbO capping layer was applied after 12 layers of PZT coating to convert any surface pyrochlore on the PZT film to perovskite. A blanket Pt layer was then sputter-deposited on the PZT at room temperature to serve as the second electrode layer.

A 30 nm thick Al_2O_3 barrier layer was deposited on the blanket Pt bottom electrode by PEALD to prevent PZT degradation resulting from poly(amic acid) imidization. The full wafer was diced into quarters before processing the polyimide layer so that the sample could fit inside the tube furnace for imidizaiton.

PI-2611 poly(amic acid) precursor was dispensed statically on the Al_2O_3-protected Pt and spun at 2000 RPM for 40 seconds. The film was hotplate-baked in air at 100°C and transferred to a tube furnace for imidization at 305°C in Ar for 75 minutes. A single coat produced a ~5.5 µm thick polyimide layer; the cast-and-cure process was repeated once to produce an 11 µm thick film. The doubled thickness was

intended for increasing the rigidity of the polymeric substrate, so that the released structure could be flat and robust. This reduced the likelihood of damaging the diaphragm structure due to handling, and more importantly, decreased the susceptibility of undesired laser beam deflection from wrinkled surfaces. The PI-2611 data sheet recommended an intermediate soft-bake at 170°C for the underlying polyimide prior to processing the subsequent layer to achieve a seamless interface between the two coats [28]. However, processing on half-cured polyimide led to a smaller combined thickness due to inter-layer solvent mixing. In this work, stacking two fully imidized polyimide layers did not result in any layer separation after release.

Windows were etched in the polyimide layer to expose the bottom Pt electrode through reactive ion etching in a parallel-plate-configured system (PlasmaTherm 720). The use of two different gas chemistries was explored: (1) a combination of CF_4 and O_2 and (2) pure O_2. A 50 nm thick of Al layer served as the hard etch-mask, as the etch rate of Al in fluorine-containing plasma is negligible due to the low vapor pressure of AlF_3 [34]. The Al layer was deposited in an RF magnetron sputtering system (Kurt J. Lesker CMS-18) with the sputtering parameters listed in Table 4-2.

Table 8-2. Processing parameters for sputtering aluminum etch mask.

Parameter	**Value**
Target composition	Al
Target size	3''
Throw distance	136 mm
RF power density	8.8 W/cm^2
Processing temperature	room temperature
Sputtering gas	Ar
Process pressure	5.0 mTorr
Deposition rate	1 Å/s

Next, the Al etch mask pattern was lithographically defined and wet-etched in diluted tetramethylammonium hydroxide (TMAH). To accomplish this, after a substrate-dehydration bake at 120°C for 10 minutes, SPR3012 was spun on the Al layer at 4000 RPM and baked at 95°C for 1.5 minutes on a hotplate in air. UV exposure was carried out on a Gen 4 MA/BA6 broadband aligner for a

dose of 54 mJ/cm^2. Then, the sample was immersed in a MICROPOSIT^{TM} CD-26 developer bath for 1 minute to form the exposed pattern in the photoresist. As the active ingredient of CD-26, TMAH, readily etches Al, the sample was left in the bath after the photoresist developing to continue with wet-etching for an extra 75 seconds. The remaining photoresist was stripped with an acetone and an IPA rinse for one minute each. The sample was rinsed with DI water and blown dry with N_2 gas.

In the PT720 RIE system, a 20% CF_4 and 80% O_2 gas mixture was admitted to the process chamber to etch the polyimide at 100 V self-bias and 100 mTorr pressure. Though removal of polyimide can be achieved in pure oxygen glow discharge, addition of a small amount of CF_4 is reported to enhance the etch rate by increasing the surface etching sites [35-37]. Measuring the polyimide thickness on a contact profilometer after 5 minutes of etching, a 0.2 µm/min etch rate was evaluated. No abnormality was observed on either the polyimide or the Al surface. However, as the etching progressed for 15 more minutes, significant roughening was observed on the polyimide surface. As Figure 4-7 shows, the roughness in the circular etching window yielded a cloudy finish visible by naked eye (panel (a)); through an optical microscope, it appeared as a black circle due to light-scattering (Figure 4-7 (b)). When all 11 µm of polyimide was etched and a subsequent 70% over-etch was performed, the roughened polymer layer was could not be cleared. The rough substance was suspected to be a nonvolatile fluorocarbon layer with CF_2 type structures passivating the polyimide surface and impeding the etching process [38-39]. Panel (c) is a cross-sectional schematic of the sample with the rough residue layer inside the polyimide etch window.

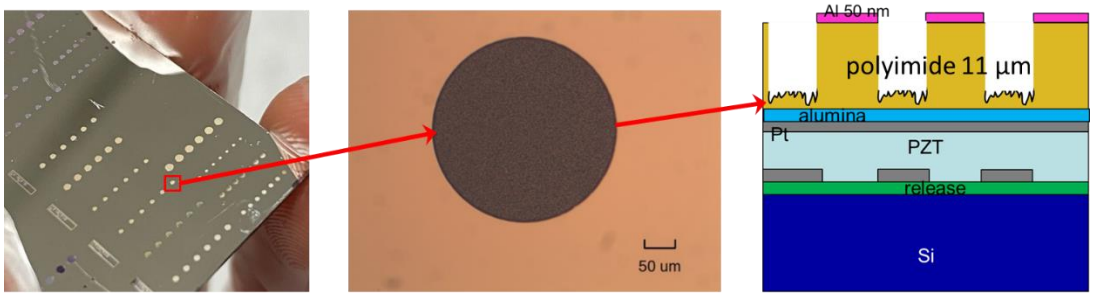

Figure 8-7. Etching the polyimide in 20% CF_4 and 80% O_2 resulted in a rough nonvolatile layer that passivated the polyimide surface. (a) The polyimide surface appeared to have a matte finish observable by naked eye. (b) An optical microscope image of the rough polymeric residue. (c) A cross-sectional schematic of the sample showing the roughness inside the polyimide window.

By eliminating fluorine from the etching gas, the rough residue layer was fully removed using pure oxygen plasma. The etching was conducted at a 150 V substrate self-bias and a 200 mTorr pressure until the residue layer cleared. The residue-free etch window is shown in Figure 4-8.

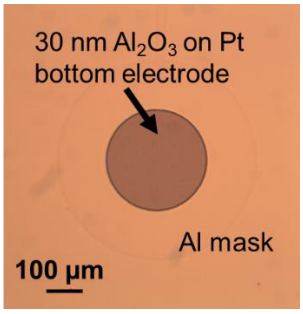

Figure 8-8. The fluorocarbon residue was fully cleared in the polyimide etch window region.

After polyimide patterning, the Al etch mask was removed in a CD-26 bath for 2 minutes. The sample was then rinsed with DI water and dried with clean compressed air before being transferred to a 50°C, 50% acetic acid bath for release.

It was found that more than half of the structures collapsed either during the release process or post-release handling due to excessive flexing. For the remaining intact electrodes, a flexible cable was designed and attached to the tabs via ACF bonding. The other end of the cable was bonded to a printed circuit board with pin-headers soldered. The electrodes were therefore electrically accessible through the circuit board. Poling was performed at 13 V ($3E_c$) at room temperature for 20 minutes.

The sample was held by a frame-like chuck on the DBLI system so that both top and bottom surfaces were accessible by the two laser beams. The flexible released samples cannot be self-supported on the frame chuck without crumpling and falling through. A rigid carrier with cavities was therefore implemented using a polycarbonate sheet with a trench-like opening punched through, as shown in Figure 4-9. The sample was adhered on the polycarbonate using a thin double-sided tape (LUCIACS® CS986,

Nitto). The tape was attached on the polycarbonate first, and a trench-like opening was formed by punching multiple 2 mm-diameter circles overlapping each other. The small circles in 4-9 (b) are the holes etched in the polyimide substrate; inside these circles are the Pt bottom electrode. The cross-sectional view of the sample structure is illustrated in panel (c).

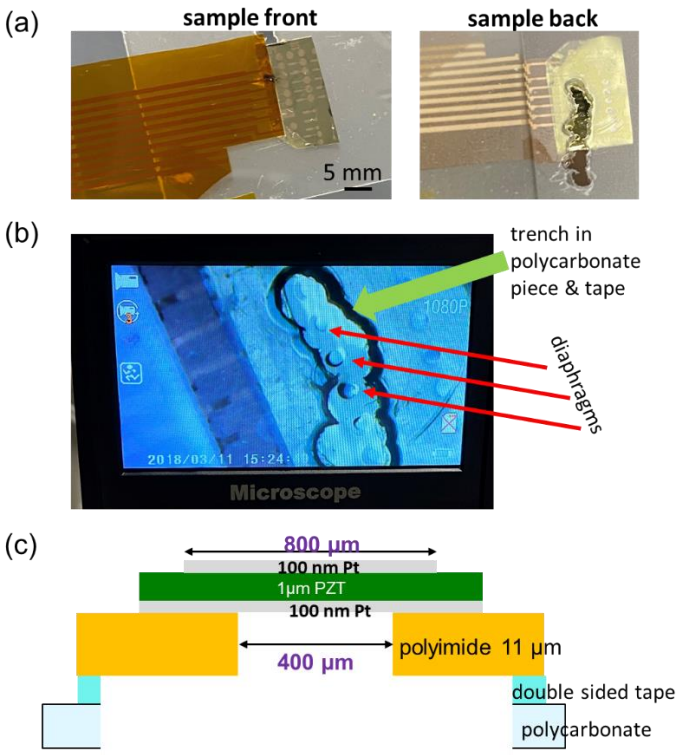

Figure 8-9. (a) The front and back view of the testing sample attached on a piece of polycarbonate rigid backing with a trench-like opening to expose the bottom Pt. (b) A zoomed-in view of the bottom electrodes through the opening in the polycarbonate. The small circles are the holes etched in the polyimide substrate. (c) The cross-sectional schematic of the fabricated sample attached on the polycarbonate backing with a double-sided tape.

4.3 Measurements by aixACCT DBLI

4.3.1 Experimental setup

The sample was loaded on the DBLI system with the polycarbonate backing vacuum-held by the smaller frame-chuck, as shown in Figure 4-10. The frame-chuck was a part of a mobile stage that could travel linearly in the *x*- and *y*- direction. The circuit board was affixed on the stage so that the ribbon cable

did not undergo mechanical strain when the sample was in motion. The system's control electronics were connected to the test electrodes via the pin-headers on the circuit board.

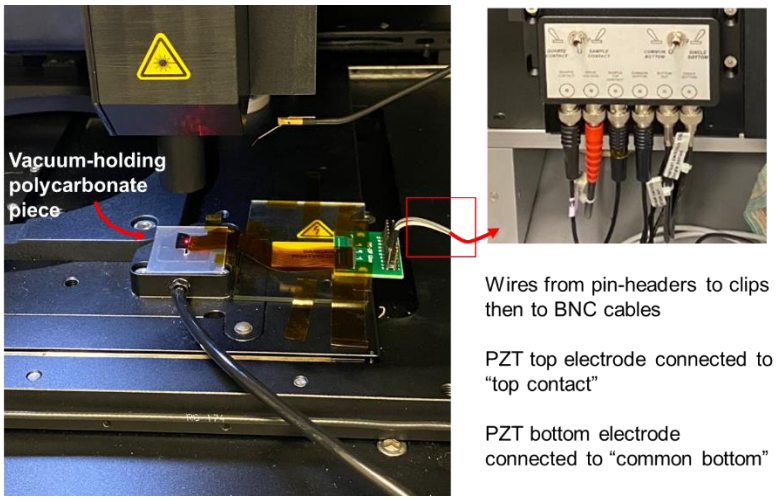

Figure 8-10. The testing setup on the aixACCT DBLI system. The polycarbonate backing is vacuum-held by the frame chuck. The pin-headers connected to the top and bottom electrodes are wired to the system's electronics with BNC cables.

The lateral position of the sample was adjusted to rough-align the center of the top electrode to the incident laser. The top surface of the sample was visualized by a camera and the stage movement was controlled by a joystick. The bottom laser beam was aligned to the top beam as a default setting of the instrument. Figure 4-11 shows the camera view of the testing electrode with the top laser beam activated.

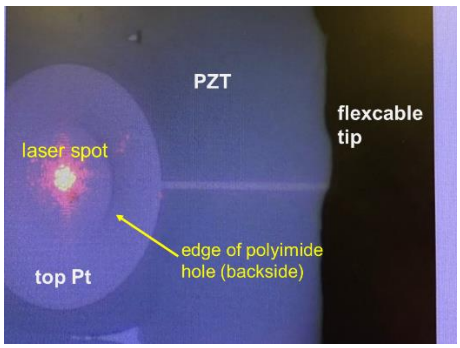

Figure 8-11. The top surface of the testing sample viewed by the system's camera. The top laser incident is centered on the top electrode circle. Judging by the faintly visible outline of the polyimide hole on the backside, the bottom laser beam should be probing directly on the bottom Pt electrode.

4.3.2 Laser interferometry measurement

Two types of electrical excitation signals were used to drive the testing electrodes: (1) large ac signal without DC bias, and (2) small ac signal with a large DC bias. The denotation "large" is for electric fields with the amplitude comparable with, or larger than the coercive field of the piezoelectric (e.g., $1E_c$, $2E_c$ etc.) while the term "small" is for fields well below the coercive field level (e.g., $0.1E_c$, $0.01E_c$ etc.). Throughout this section, the two excitation signals will be referred as "large signal" and "small signal", respectively.

After sample-processing, only a small number of electrodes were usable for the DBLI measurements as a large fraction of the fabricated electrodes were damaged during either the release or the post-release handling process (compounded by the low-throughput pattern design). As a result, the measurement results reported in this section are data obtained from two 800 μm diameter electrodes. The polyimide hole on the backside was a circle of 400 μm diameter.

4.3.2.1 Measurements with laser probing on top and bottom Pt

For the large signal measurement, the top electrode was driven with an 8 V triangular ac excitation at 100 Hz without DC bias. Polarization and displacement in the 3-direction were measured by the DBLI system and the data are presented in Figure 4-12 (a) with respect to the ac voltage amplitude.

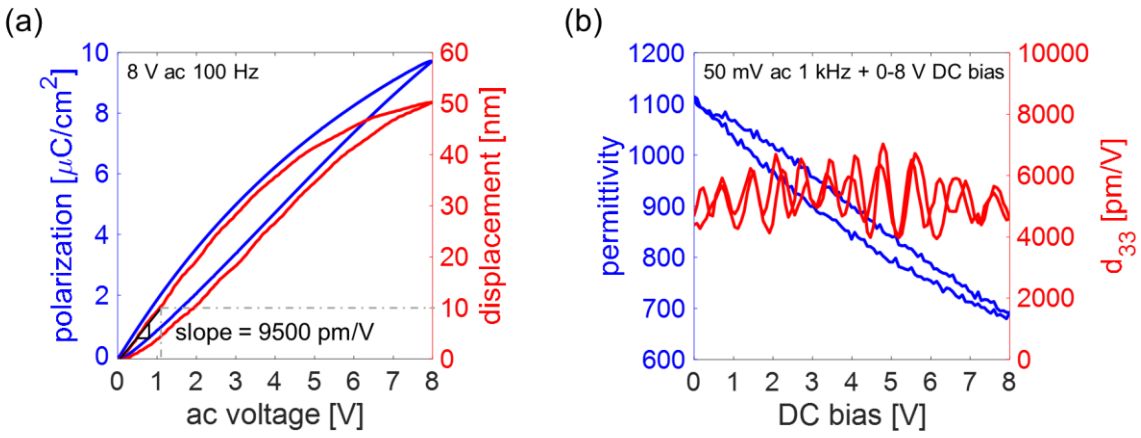

Figure 8-12. (a) Large signal measurement with 8 V ac excitation at 100 Hz. The slope of the displacement curve fitted linearly between 0 and 1 V gave an implausibly large d_{33} of 9500 pm/V. (b) Small signal measurement with 50 mV ac excitation at 1 kHz superimposed on a DC bias from 0 to 8 V. The measured d_{33} values are on the same order of magnitude as the large signal measurement.

While the polarization results are within the correct range, the detected displacement reached 50 nm, indicating a 5% strain level – five times larger than the reported strain limit for many PZT thin films. From the slope of the decreasing field displacement curve between 0 to 1 V, the d_{33} was evaluated as an erroneous 9500 pm/V. The data was then compared with small signal measurements, in which the electrode was driven with a 0.05 V ac signal at 1 kHz superimposed on a DC bias sweeping between 0 to 8 V. The small-signal results are shown in Figure 4-12 (b) as permittivity and d_{33} plotted against the DC bias voltage. While the permittivity showed the correct trend and values, the d_{33} was oscillating between implausibly large values of 4000 pm/V and 7000 pm/V. These results strongly suggested that artifacts existed in the measurement regime, which were not being accounted for by the DBLI system. As correct electrical properties were verified, the errors were presumably a result of the optical signal.

4.3.2.2 Verification with single-beam interferometer

Single-beam interferometry was used to cross-check the displacement level. The same DBLI system is equipped with a single-beam interferometry function.

With the laser beam impinging on the top electrode in the center, a 5 V peak triangular ac signal was applied at 100 Hz to excite the PZT. The measured displacement along the thickness direction and the polarization are shown in Figure 4-13 as a function of the ac voltage signal. The interferometry revealed an even larger top surface displacement of 1.5 μm with the sign reversed from the double-beam experiments. As the transverse d_{31} coefficient bears the opposite sign, the negative-signed single-beam result implies that bending was the dominating contribution in the out-of-plane response. This extremely large displacement moves the system out of the calibrated range for quantitative measurements.

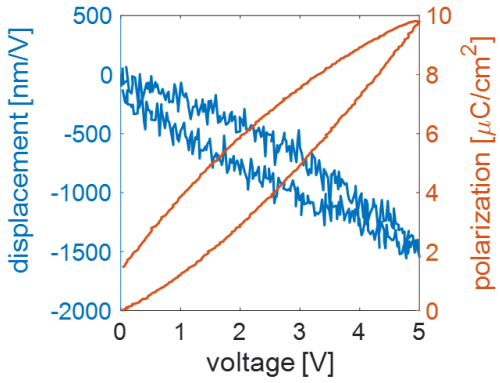

Figure 8-13. The single-beam laser interferometry detected minus-signed, larger displacements from probing the top Pt electrode driven between 0 and 5 V at 100 Hz. This implies that there is significant bending in the system that is not being compensated by the instrument.

Though the double-beam approach is expected to compensate the bending contribution by default, extensive bending in the structure could potentially introduce phase shift in one laser beam and/or cause misalignment between the two measurement beams, resulting in inflated pathlength difference uncorrectable by the DBLI system.

The phase shift contribution can be explained by the schematics in Figure 4-14. The curvature of the sample is approximated as a tilt within the laser spot. If the laser beam is a sum of infinitely subdivided sinusoidal light waves, the tilting sample surface introduces multiple phase shifts between these waves, thus reducing the overall intensity contrast.

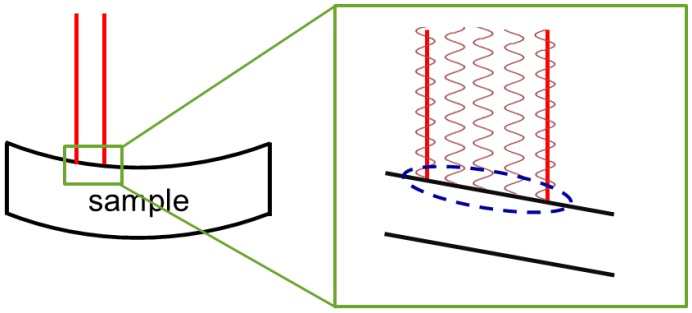

Figure 8-14. Within the laser incidence, the sample tilt results the light waves to be out-of-phase, thus reducing the overall intensity contrast.

In another scenario, as shown in Figure 4-15 (a), the curvature of the sample slightly converges the top laser beam as it reflects off the top sample surface, resulting in a narrower beam incident on the bottom surface. The mismatch of the beam spot size would cause a lateral offset between the subdivided

top and bottom wave segments, as indicated by the green dashed enclosure in panel (b). This offset will give rise to an erroneous contribution (panel (c)), e, which is a function of the lateral laser beam shift Δa and the local tilt angle of the sample θ in the form of $e = \Delta a \cdot tan\theta$. The geometry change of the structure under excitation was unknown and would be complex to quantify; the difference in beam spot sizes was also unknown. But as a rough estimation, by using the single-beam interferometer result, where a 1.5 μm vertical displacement was measured for an 800 μm diameter electrode, the tilt angle is therefore approximately $tan^{-1}\left(\frac{1.5}{400}\right)$ =0.21°. Using this angle and a possible lateral beam shift as small as 2 μm, a displacement error of $2000 \times tan0.21°$=7.3 nm can result; this error contribution is already comparable to a 10 nm PZT thickness change assuming a 1% strain in a 1 μm thick film.

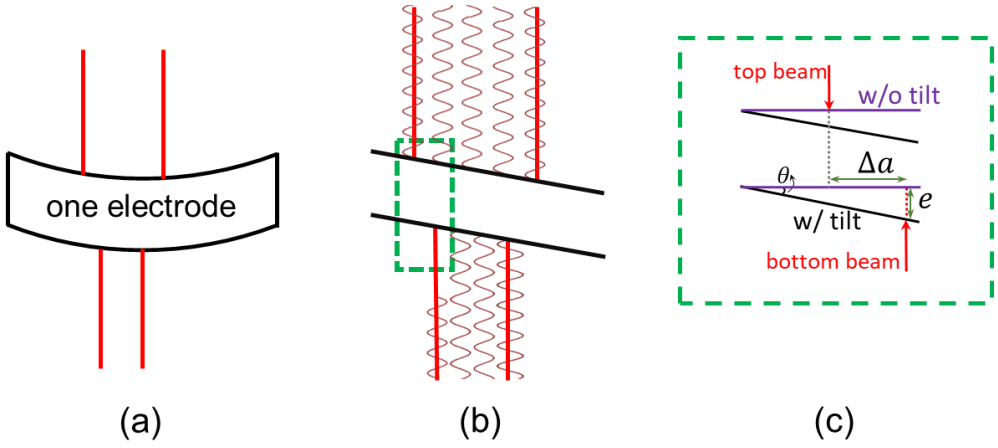

Figure 8-15. (a) The sample curvature results in a beam width mismatch between the top and the bottom measurement laser beams. (b) The difference in spot size introduces a lateral offset between the top and bottom light segments. (c) The offset gives rise to an error contribution term, e, which is a function of the lateral laser beam shift Δa and the local tilt angle of the sample θ in the form of $e = \Delta a \cdot tan\theta$.

Another possible source of error comes from the laser beam deflection due to the sample tilt/curvature. As schematically illustrated in Figure 4-16, the curvature of the sample deflects the laser beam, producing a phase shift in the reflected beam and possibly reducing the intensity as only a portion of the beam reaches the photodetector. Both the phase shift and the intensity reduction would make the measurements inaccurate.

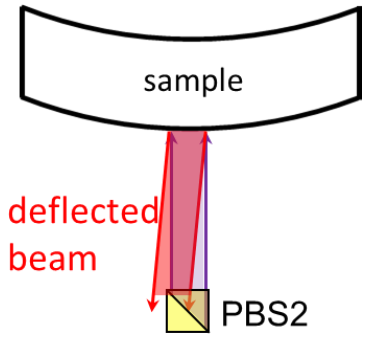

Figure 8-16. The tilt/curvature in the sample deflects the measurement laser beams and causes a phase shift and an intensity reduction in the reflected beams, thus making the measurements inaccurate.

The substantial bending is likely a result of asymmetry in the sample structure and the continuous PZT layer. As the polyimide underneath the top electrode was not fully removed on the backside, as shown in Figure 4-17 (a), the remaining polymer material presumably served as a passive layer that shifted the neutral axis away from the PZT. This asymmetry, along with the flexible characteristic of the polyimide, resulted in bending of large magnitude. The continuous PZT layer further deteriorates the situation as the entire sample was probably globally actuated by the activated PZT area under the testing electrode. Thus, two modifications to the sample structure are expected to reduce or suppress the excess bending. First, the etched window in the polyimide should be no smaller than the top electrode so that the activated structure does not bear any asymmetry. Second, patterning the PZT into islands could isolate or reduce the global actuation. In addition, the flexible sample will be fixed on glass instead of polycarbonate. The higher rigidity in glass should be able to suppress the flexible structure from bending more effectively. The proposed the structure is shown schematically in Figure 4-17 (b).

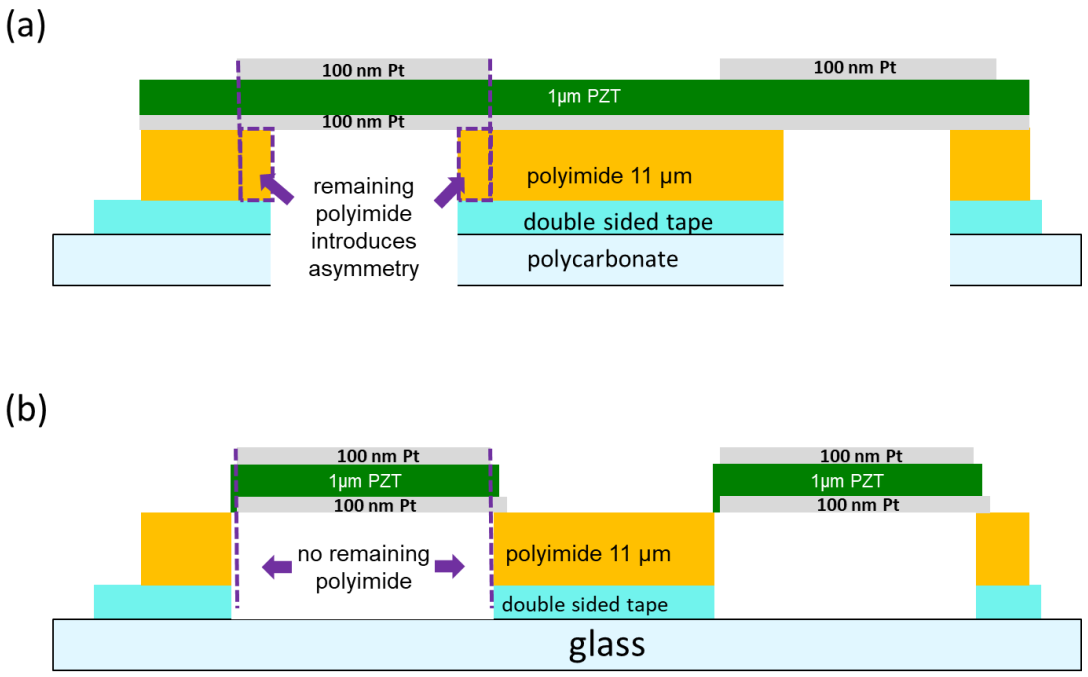

Figure 8-17. (a) The remaining polyimide below the top electrode introduced asymmetry in the structure, which, combined with the continuous configuration of the PZT, resulted in large global bending in the sample. (b) The proposed modifications are removing the extra polyimide, patterning the PZT, and fixing the flexible structure on a more rigid backing - glass.

4.3.2.3 Small-electric-field excitation

In order to curtail the bending in the flexible structure and prevent the associated laser-beam misalignment, measurements were attempted with significantly reduced driving fields. Unipolar ac signals of 1.0 V ($0.25E_c$), 0.5 V ($0.125E_c$) and 0.3 V ($0.075E_c$) were applied to the same electrodes at 100 Hz. Figure 4-18 shows the polarization and displacement data as a function of the ac voltage amplitude for a maximum 1.0 V in panel (a), 0.5 V in panel (b), and 0.3 V in panel (c). Through calculating the slope of the linear-fit of each displacement curve, the d_{33} values were ~4500 pm/V for the 1.0 V case, ~4300 pm/V for the 0.5 V case and ~3600 pm/V for the 0.3 V case.

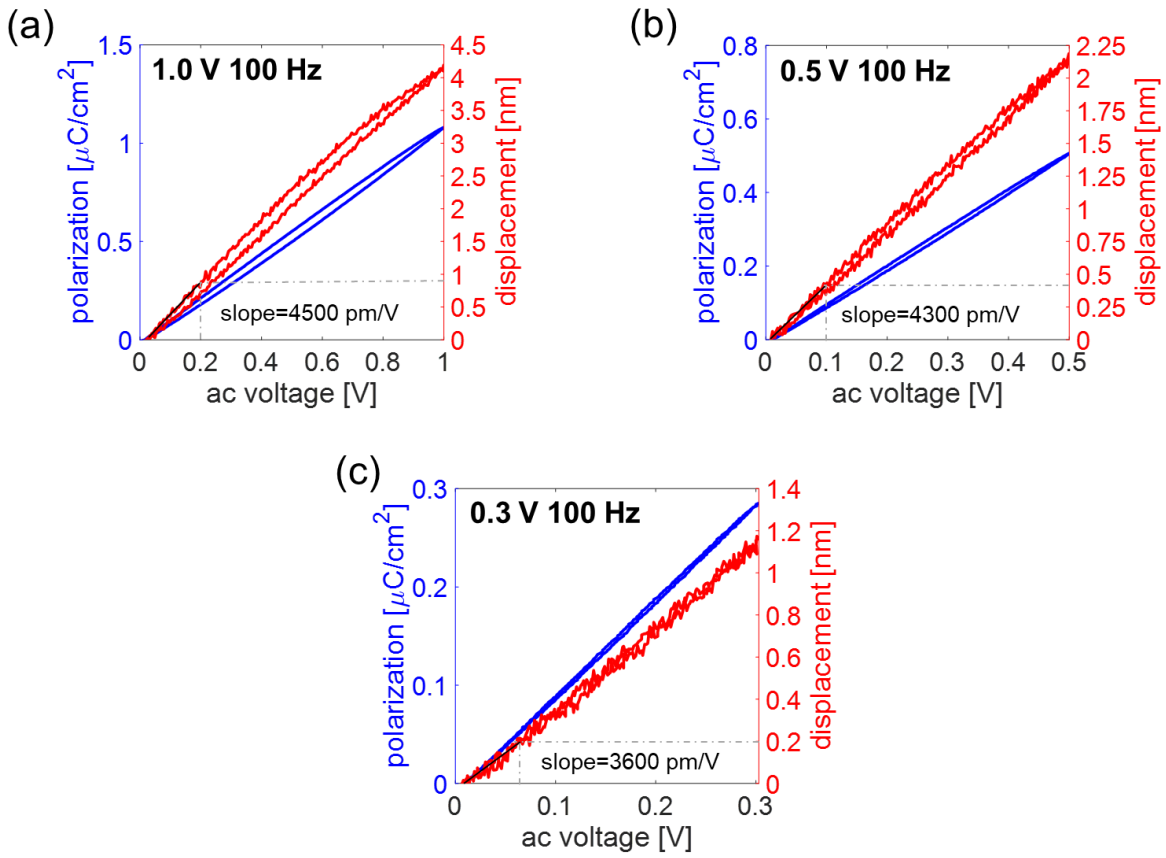

Figure 8-18. (a) With maximum of 1.0 V ac triangular excitation at 100 Hz, the d_{33} is measured to be 4500 pm/V (b) With maximum of 0.5 V ac triangular excitation at 100 Hz, the d_{33} is measured to be 4300 pm/V. (b) With 0.3 V ac triangular excitation at 100 Hz, the d_{33} is measured to be 3600 pm/V.

With decreasing excitation level, the measured d_{33} was shifting towards a lower value and presumably in the direction approaching the correct piezoelectric coefficient. But the sample deflection was still far outside of the range for the two measurement beams to stay aligned and the artifacts to be compensated.

4.4 Conclusions

Attempts were made to measure the unclamped longitudinal piezoelectric coefficient, d_{33}, of a 1 μm thick randomly-oriented $Pb(Zr_{0.52}Ti_{0.48})_{0.98}Nb_{0.02}O_3$ film on a 11 μm thick polyimide substrate with a commercial DBLI system. Holes were etched in the polyimide layer to expose the bottom Pt, so that the laser beams could probe directly on the top and the bottom Pt electrodes.

The test electrodes were circles of 800 μm in diameter on a blanket PZT film. The holes in the polyimide were concentric circles of 400 μm in diameter. Measurements were conducted with two types of electrical signals for comparison: (1) 8 V ac signal at 100 Hz without DC bias and (2) 0.05 V ac excitation at 1 kHz superimposed on an 8 V DC bias. Both approaches measured d_{33} an order of magnitude larger than the maximum physically plausible value (for 1% out-of-plane strain). The error source was suspected to be the misalignment between the top and bottom laser beams as a result of significant bending in the device system. The bending was presumably caused by the asymmetry in the device structure as an annulus of the polyimide remained on the backside within the top electrode coverage. The continuous PZT configuration probably also encouraged the large-magnitude bending.

As a measure to reduce bending and improve the setup to achieve correct d_{33} measurements, the sample structure is proposed to have a patterned PZT layer and windows etched in the polyimide that match the lateral dimensions of the top electrode outline. Other suggestions for possible improvements in the measurement setup for bending-suppression are proposed in the future work section in Chapter 6.

Even though correct evaluation of released d_{33} could not be achieved, the experiments conducted in this chapter identified critical artifacts in the sample that can produce inaccurate DBLI measurements for fully released piezoelectric systems. The inflated displacement as a result of beam-misalignment may have been mistaken as enhanced piezoelectric responses in some reports in the literature [33].

4.5 Chapter references

[1] A. L. Kholkin, "Non-linear piezoelectric response in lead zirconate titanate (PZT) films," *Ferroelectrics,* vol. 238, pp. 235-243, 2011

[2] N. Bassiri-Gharb, I. Fujii, E. Hong, S. Trolier-McKinstry, "Domain wall contributions to the properties of piezoelectric thin films," *J. Electroceram.,* vol. 19, pp. 47-65, 2007

[3] S. Buhlmann, B. Dwir, J. Baborowski, and P. Muralt, "Size effect in mesoscopic epitaxial ferroelectric structures: Increase of piezoelectric response with decreasing feature size," *Appl. Phys. Lett.*, vol. 80, pp. 3195-3197, 2002

[4] V. Nagarajan, A. Stanishevsky, L. Chen, T. Zhao, B-T. Liu, J. Melngailis, A. L. Roytburd, R. Ramesh, J. Finder, Z. Yu, R. Droopad, and K. Eisenbeiser, "Realizing intrinsic piezoresponse in epitaxial submicron lead zirconate titanate capacitors on Si," *Appl. Phys. Lett.*, vol. 81, pp. 4215-4217, 2002

[5] S. Shetty, J. I. Yang, J. Stitt, and S. Trolier-McKinstry, "Quantitative and high spatial resolution d_{33} measurement of piezoelectric bulk and thin films," *J. Appl. Phys.*, vol. 118, pp. 174104, 2015

[6] F. Griggio, S. Jesse, A. Kumar, O. Ovchinnikov, H. Kim, T. N. Jackson, D. Damjanovic, S. V. Kalinin, and S. Trolier-McKinstry, "Substrate clamping effects on irreversible domain wall dynamics in lead zirconate titanate thin films," *Phys. Rev. Lett.*, vol. 108, pp.157604, 2012

[7] M. Wallace, R. L. Johnson-Wilke, G. Esteves, C. M. Fancher, R. H. T. Wilke, J. L. Jones, and S. Trolier-McKinstry, "*In situ* measurement of increased ferroelectric/ferroelastic domain wall motion in clamped tetragonal lead zirconate titanate thin films," *J. Appl. Phys.*, vol. 117, pp. 054103, 2015

[8] B. Jaffe, W. R. Cook Jr., and H. Jaffe, *Piezoelectric Ceramics*, Academic Press London and New York, 1971, pp.7-20

[9] K. Uchino, "Piezoelectric Devices," in *Ferroelectric Devices*, CRC Press, Taylor & Francis Group, Boca Raton, FL, 2010, pp. 25-41

[10] K. Lefki and G. J. M. Dormans, "Measurement of piezoelectric coefficients of ferroelectric thin films," *J. Appl. Phys.*, vol. 79, pp. 1764-1767, 1994

[11] B. J. Rodriguez, D-J. Kim, A. I. Kingon, and R. J. Nemanich, "Measurement of the effective piezoelectric constant of nitride thin films and heterostructures using scanning force microscopy," in *Mat. Res. Soc. Symp. Proc.*, 2002, Materials Research Society, vol. 693, pp. I9.9

[12] H-N. Lin, S-H. Chen, S-T. Ho, P-R. Chen, and I-N. Lin, "Comparative measurements of the piezoelectric coefficient of a lead zirconate titanate film by piezoresponse force microscopy using electrically characterized tips," *J. Vac. Sci. Technol. B*, vol. 21, no. 2, pp. 916-918, 2003

[13] S. V. Kalinin, B. J. Rodriguez, S-H. Kim, S-K. Hong, A. Gruverman, and E. A. Eliseev, "Imaging mechanism of piezoresponse force microscopy in capacitor structures," *Appl. Phys. Lett.*, vol. 92, pp. 152909, 2008

[14] G. Zavala, J. H. Fendler, and S. Trolier-McKinstry, "Characterization of ferroelectric lead zirconate titanate films by scanning force microscopy," *J. Appl. Phys.*, vol. 81, no. 11, pp.7480-7491, 1997

[15] T. Jungk, A. Hoffmann, and E. Soergel, "Quantitative analysis of ferroelectric domain imaging with piezoresponse force microscopy," *Appl. Phys. Lett.*, vol. 89, pp. 163507, 2006

[16] T. Jungk, A. Hoffmann, and E. Soergel, "Challenges for the determination of piezoelectric constants with piezoresponse force microscopy," *Appl. Phys. Lett.*, vol. 91, pp. 253511, 2007

[17] A. L. Kholkin, C. Wutchrich, D. V. Taylor, and N. Setter, "Interferometric measurements of electric field-induced displacements in piezoelectric thin films," *Rev. Sci. Instrum.*, vol. 67, no. 5, pp. 1935-1941, 1996

[18] T. Haccart, E. Cattan, D. Lohse, C. Kugeler, S. Tiedke, U. Bottger, and R. Waser, "Evaluation of niobium effects on the longitudinal piezoelectric coefficients of Pb(Zr, Ti)O_3 thin films," *Rev. Sci. Instrum.*, vol. 76, pp. 3292, 2000

[19] P. Gerber, A. Roelofs, O. Lohse, C. Kugeler, S. Tiedke, U. Bottger, and R. Waser, "Short-time piezoelectric measurements in ferroelectric thin films using a double-beam laser interferometer," *Rev. Sci. Instrum.*, vol. 74, pp 2613, 2003

[20] V. Kovacova, N. Vaxelaire, G. Le Rhun, P. Gergaud, T. Schmitz-Kempen, and E. Defay, "Correlation between electric field induced phase transition and piezoelectricity in PZT films," *Physical Review B,* vol. 90, pp. 140101R, 2014

[21] R. Herdier, D. Jenkins, E Dogheche, and D. Remiens, and M. Sulc, "Laser Doppler vibrometry for evaluating the piezoelectric coefficient d_{33} on thin film," *Rev. Sci. Instrum.*, vol. 77, pp. 093905, 2006

[22] S. Lepadatu, M. Stewart, and M. G. Cain, "Quantification of electromechanical coupling measured with piezoresponse force microscopy," *J. Appl. Phys.*, vol. 116, pp. 066806, 2014

[23] Q. M. Zhang, S. J. Jang, and L.E. Cross, "High-frequency strain response in ferroelectrics and its measurement using a modified Mach-Zehnder interferometer," *J. Appl. Phys*. vol. 65, pp. 2807, 1989

[24] S. Sivaramakrishnan, P. Mardilovich, A. Mason, A. Roelofs, T. Schmitz-Kempen, and S. Tiedke, "Electrode size dependence of piezoelectric response of lead zirconate titanate thin films measured by double beam laser interferometry," *Appl. Phys. Lett.*, vol. 103, pp. 132904, 2013

[25] M. Stewart, and M. G. Cain, "Direct piezoelectric measurement: The Berlincourt method," in *Characterisation of Ferroelectric Bulk Materials and Thin Films*, Springer, Dordrecht, 2014, pp. 37-64.

[26] F. Xu, F. Chu, and S. Trolier-McKinstry, "Longitudinal piezoelectric coefficient measurement for bulk ceramics and thin films using pneumatic pressure rig," *J. Appl. Phys.*, vol. 86, no. 1, pp. 588-594, 1999

[27] K. Prume, S. Tiedke, and T. Schmitz-Kempen, "Double-beam and four-point: Piezoelectric thin-film characterization for MEMS applications," *Mikroniek,* no. 4, pp. 31-35, 2010

[28] *PI-2600 Series – Low Stress Applications,* HD MicroSystems, Parlin, NJ, USA, 2009

[29] F. Casset, A. Devos, S. Sadtler, A. L. Louarn, P. Emery, and G. L. Rhun, P. Ancey, S. Fanget, and E. Defay, "Young's modulus and Poisson ratio of PZT thin film by picosecond ultrasonics," In *IEEE International Ultrasonics Symposium,* 2012, IEEE, pp. 2180-2183

[30] H. Yeo and S. Trolier-McKinstry, "{001} Oriented piezoelectric films prepared by chemical solution deposition on Ni foils," *J. Appl. Phys.*, vol. 116, pp. 14105, 2014.

[31] C. L. Bauer, and R. J. Farris, "Determination of Poisson's ratio for polyimide films," *Polymer Engineering and Science*, vol. 29, no. 16, pp. 1107-1110, 1989

[32] C. Lee, J. Seo, Y. Shul, and H. Han, "Optical properties of polyimide thin films – effect of chemical structure and morphology," *Polymer Journal*, vol. 35, no. 7, pp. 578-585, 2003

[33] J. C. Frederick, "Structure-property relations in sputter deposited epitaxial (1-*x*)$Pb(Mg_{1/3}Nb_{2/3})O_3$-*x*$PbTiO_3$ thin films," Ph.D. Dissertation, Department of Materials Science and Engineering, University of Wisconsin-Madison, 2017, pp. 94-117

[34] D. W. Hess, "Plasma etch chemistry of aluminum and aluminum alloy films," *Plasma Chemistry and Plasma Processing*, vol. 2, no. 2, pp. 141-155, 1982

[35] G. Turban and M. Rapeaux, "Dry etching of polyimide in O_2-CF_4 and O_2-SF_6 plasmas," *Journal of The Electrochemical Society*, vol. 130, pp. 2231-2236, 1983

[36] R. d'Agostino, F. Cramarossa, and S. D. Benedictis, "Diagnostics and decomposition mechanism in radio-frequency discharges of fluorocarbons utilized for plasma etching or polymerization," *Plasma Chemistry and Plasma Processing*, vol. 2, no. 3, pp. 213-231,1982

[37] F. D. Egitto, F. Emmi, R. S. Horwath, and V. Vukanovic, "Plasma etching of organic materials. I. polyimide in O_2-CF_4," *Journal of Vacuum Science & Technology B: Microelectronics Processing and Phenomena*, vol. 3, pp. 893 – 904, 1985

[38] R. Loffler, M. Fleischer, and D. P. Kern, "An anisotropic dry etch process with fluorine chemistry to create well-defined titanium surfaces for biomedical studies," *Microelectronic Engineering*, vol. 97, pp. 361-264, 2012

Chapter 5. Piezoelectrically Adjustable X-ray Mirror

5.1 Introduction

This chapter discusses adjustable mirror technology proposed for use in the Lynx mission, the next-generation X-ray observatory in preparation for the 2020 Decadal Survey. The *Lynx* mission aims to significantly improve the sensitivity over the previous generation telescope, *Chandra*, permitting detection of supermassive black holes at their formation and increasing our understanding of galactic evolution [1-2].

The sensitivity of X-ray telescopes is determined by the effective telescope collecting area and angular resolution. While keeping a 0.5 arcsecond half-power diameter (HPD) resolution of *Chandra*, the Lynx's collecting area (2 m^2) is expected to increase by 20-30 times. This can be realized by nesting large numbers of grazing-angle X-ray mirror segments, bringing X-rays in the 0.1 keV to 10 keV energy range to focus. In order to achieve this, it will be imperative for the mirror segments to be thin and light-weight, while simultaneously maintaining a high geometric throughput at grazing incidence and outstanding optical figure. However, thin optics are inherently more flexible and thus much more prone to stress-induced figure distortion during manufacturing, assembly and potentially, in-orbit operation [3-4].

One of the proposed approaches to address the figure distortion is to employ piezoelectrically adjustable mirror segments prepared from either glass or Si. As has been demonstrated previously, thin-film piezoelectric actuator cells deposited on the backside of the mirror can correct figure errors using the converse piezoelectric effect: under an applied voltage, the piezoelectric layer deforms and induces strain in the mirror in a deterministic manner. Thin-film lead zirconate titanate (PZT) was chosen for this application as its high piezoelectric coefficient allows large induced strains at lower driving voltages [5]. This study is an on-going collaborative effort joined by Penn State and the Smithsonian Astrophysical Observatory (SAO).

5.2 Piezoelectrically adjustable X-ray optics at PSU and SAO

The adjustable mirror prototypes used in this study employed 400 μm thick, Eagle XG borosilicate glass substrates thermally slumped to a radius of curvature of 220 mm along one axis (for cylindrical and pseudo-conical mirrors), corresponding to an intermediate *Lynx* shell [6-7]. The slumped glass substrates were then laser-cut into 101.6 mm × 101.6 mm pieces in order to fit inside most processing tools at Penn State. The uncorrected angular resolution of the substrates was measured to be in the range of 5-10 arcseconds. Finite element analysis (FEA) simulation predicted an improvement to a 0.5 arcsecond resolution after figure correction using the thin-film PZT on the backside of the mirror. This correction level requires vertical displacements in the PZT film in the 0.5 to 1.0 μm range [8].

5.3 Prototype HFDFC cylindrical optics

The proof-of-concept for the adjustable X-ray mirror has been previously demonstrated with two iterations on flat and curved parts with successful influence function results measured on a noncontact profilometer and a wavefront sensor [9-10]. This section reports part of the study of the succeeding generation, denoted as the High Fidelity Deterministic Figure Control (HFDFC) series using cylindrical mirrors.

The prototype mirror consisted of six thin-film layers, with four on the actuator side (convex) and the other two on the X-ray side (concave) of the mirror. Figure 5-1 is a schematic of the layers. The actuator side had a blanket layer of PZT film sandwiched between the top and bottom electrodes. The bottom electrode was a blanket layer of Ti/ Pt and the top electrode consisted of a pixelated array of patterned Pt squares (or rectangles). These layers were deposited prior to the depositions of the Cr and Ir reflective coatings on the X-ray side. This processing sequence was followed to prevent changes in the stress-state induced by thermal cycling and to preserve the pristine physical state of the X-ray coatings.

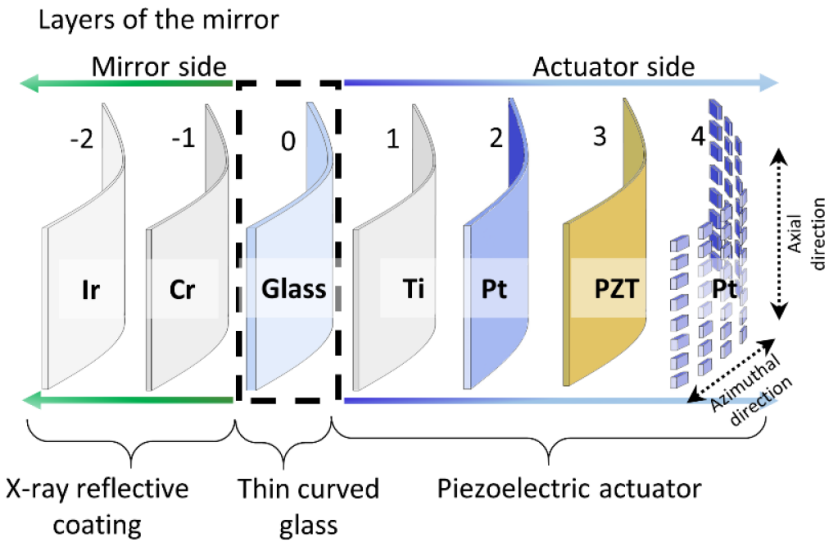

Figure 9-1. A schematic of the HFDFC mirror separated into individual layers. Starting from the "0" level as the curved glass substrate, the Cr and Ir X-ray reflective coatings are on the concave side of the mirror labeled as "-1" and "-2" while the actuator layers are on the convex side of the mirror denoted as layers "1" through "4". Figure reproduced from Walker et al. [11].

5.3.1 Layer and pattern design for HFDFC mirrors

The PZT actuator was divided into individual cells so that figure correction could be localized to a specific pixel on the mirror. The cells were defined by patterning the top Pt electrodes over the blanket PZT film into 5 mm (axial) × 10 mm (azimuthal) rectangles. When a voltage is applied to a specific electrode, only the PZT volume under the electrode will be actuated. For HFDFC studies, a total of 112 cells were arranged in 16 rows and 7 columns separated by 1 mm. Traces connecting the cells ran through the alley ways and terminated at the flat (optical) edges of the mirror to form two columns of contact pads for bonding flexible ribbon cables. The anisotropic conductive film (ACF) bonding technology, detailed in Chapter 3, was employed to realize the cable attachment. The arrangement of the pixels and the bonding are illustrated in Figure 5-2 (a).

The top Pt was patterned using photolithography. Since the photoresists was spin-coated on curved substrates and the photomask (Great Lakes Engineering, Maple Grove, MN, USA) was a sheet of Mylar taped on the mirror for contact, the feature dimensions were designed to allow extra tolerance.

Therefore, the minimum line width and gap were chosen to be 80 μm and 190 μm, respectively. This dimension allowed a maximum of 3 traces to pass through the alley way between pixels. The ACF contact pads were 3 mm long, 0.75 mm wide, and arranged in a 1-mm-pitch 1-D array. They were bundled into six clusters with four containing 21 pads and two containing 14. Each pad-cluster had a total length under 2.5 cm so that it did not exceed the length of the ACF bonder thermode (length = 2.5 cm). Above the two columns of the ACF bonding pads were two rectangles reserved for bottom Pt electrodes, which were the Ti/Pt regions masked by Kapton tapes prior to PZT sputter-deposition. Small windows were opened on the four corners and the two edges of the mask to coarsely center it over the mirror.

The patterns were designed using L-Edit (Tanner EDA, Inc) and plotted with reversed polarity on Mylar films to produce a dark-field mask for the lift-off process. Figure 5-2 (b) shows a picture of the finished photomask product.

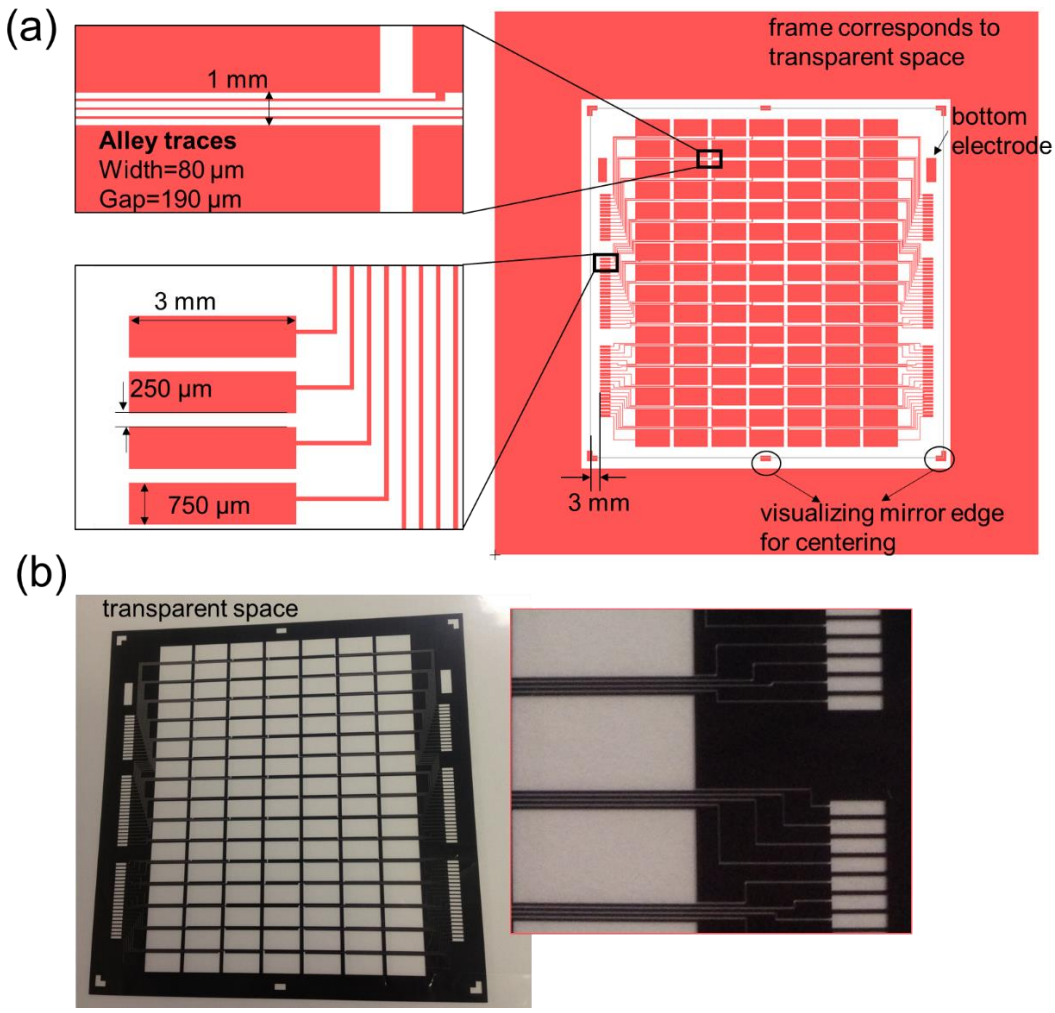

Figure 9-2. (a) A schematic of the top Pt electrode pattern drawn with the L-Edit software. The HFDFC prototype had 112 actuator cells of 10 mm × 5 mm rectangles arranged in 17 columns and 6 rows with a 1 mm gap. These features are plotted on (b) a piece of Mylar film to be used as a flexible photolithography mask for the curved glass substrate.

5.3.2 Fabrication for HFDFC3

Several pieces of glass were slumped at SAO. The glass substrate with the best pre-processing figure was selected as the main subject of study. It was named "HFDFC3".

Prior to deposition, the glass substrate of HFDFC3 was cleaned using a five-step process. This process was optimized through trial with other glass samples [12]. The substrate was first immersed and sonicated for 5 minutes in a bath filled with *KleanAR* (Avantor Perf Mat-Macron Lab), a commercial

solution containing sulfuric acid and chromic acid. It was then rinsed with DI water for 3 minutes and sonicated in an acetone bath for 5 minutes followed by an isopropanol bath for 5 minutes. The substrate was then removed from the isopropanol bath and rinsed by DI water for 3 minutes. After being blown dry with compressed nitrogen gas, the glass substrate was treated with oxygen plasma to remove residual organic contamination in an M4L RF Gas Plasma system (PVA, TePla) for 2 minutes at 550 mTorr, 200 W power, 150 sccm oxygen, and 50 sccm helium.

The first two layers deposited on the actuator side were 20 nm Ti and100 nm Pt, making up the bottom electrode for the PZT actuator. Ti served as an adhesion layer between the glass and Pt due to it readily oxidizes and forms a strong bond with glass. This oxidizing characteristic of Ti required the two metals to be deposited without breaking the vacuum. The deposition apparatus was a direct current (DC) magnetron sputtering system (Kurt J. Lesker CMS-18) with a sputter-up configuration. Inside the cylindrical process chamber, the sputter target was offset by 82.5 mm and tilted by 15° from the central axis of the substrate. The substrate rotated at 10 RPM during the deposition. Table 5-1 summarizes the sputtering conditions for the thin-film layers on the actuator side of the HFDFC prototype mirrors.

Table 9-1. Sputtering conditions for the thin-film layers on the actuator side

Parameter	**Value**		
Target composition	Ti	Pt	PNZT (105/1/52/48)
Target size	3''	3''	3''
Throw distance	136 mm	136 mm	136 mm
RF power density	4.4 W/cm^2	4.4 W/cm^2	4.4 W/cm^2
Processing temperature	room temperature	room temperature	room temperature
Sputtering gas	Ar	Ar	Ar
Process pressure	2.0 mTorr	2.5 mTorr	4-5 mTorr
Deposition rate	0.9 Å/s	2.40 Å/s	12500 seconds for 0.5 µm

The Pt had nanometer scale microstructure and a predominantly (111) orientation, observed from the XRD pattern [11], making it suitable for subsequent deposition and crystallization of high quality PZT films.

The 1.5 μm piezoelectric PZT film was sputter-deposited on Pt in a three-layer step with crystallization occurring after each layer of 0.5 μm thick. Growing the film in multiple layers was critical for maintaining high yield as it offset the defects in each layer and prevented them from percolating through the entire film. The 0.5μm single-layer thickness was chosen to allow the excess PbO to volatize without cracking the film. The PZT film was sputtered in a radio frequency (RF) magnetron sputtering system (Kurt J. Lesker CMS-18) with the same chamber configurations as for the metal sputtering but in a different system to prevent Pb contamination. The sputtering conditions for PZT can be found in Table 5-1. Each crystallization was carried out in a rapid thermal annealing (RTA) furnace at 650°C for 1 minute in air.

The characterization results of the PZT films are reported in detail by Walker et al. [11], and a brief summary is described here. The resulting PZT films had a random crystallographic orientation with a perovskite structure free of secondary phases. The average grain size was ~375 nm determined by the line intercept method (ASTM E 112). There were no visible pores on the film surface. The root mean squared (RMS) surface roughness was measured to be 4.6 nm with a peak to valley roughness of 29 nm using atomic force microscopy (AFM) with an Asylum Research instrument.

To achieve the division of the blanket PZT layer into independently controllable actuator cells, the top Pt electrode was sputter-deposited and lithographically patterned by lift-off. This lithography process followed the same procedure as described in Chapter 2 but used two different photoresist layers. Polydimethylglutarimide-based LOR1A (MicroChem Corp., Newton, MA) was used for the first (bottom) layer and SPR3012 (MicroChem Corp., Newton, MA) for the second (top) layer.

A customized carrier holder (Figure 5-3) was designed and crafted by Julian Walker [12] to hold the curved glass substrate during spin-coating. The holder had a 6'' Si wafer base on top of which four plastic stoppers were attached and arranged into a frame-like structure to tightly enclose the mirror. The height of the stoppers was ~5 mm higher than the highest point of the mirror to prevent the substrate from sliding off during spinning. The stoppers were glued onto the Si wafer with cyanoacrylate-based super glue (LOCITITE 420) and secured further with Kapton tape. This apparatus greatly improved the curved

lithography development, as it held the mirror segment securely during spin-coating at 4000 RPM. The high spin-speed reduced the resist edge-bead and improved the thickness uniformity. Previously, samples were secured on a carrier wafer with tape alone, allowing a maximum spin-speed of 900 RPM. [9].

LOR1A was initially spray-coated on the curved substrate using a Prism 500 system (Ultrasonic Systems, Inc). The deposition conditions were programmed with a head height of 70 mm, speed of 120 cm/min, flow rate of 4 ml/min and an air pressure of 20 Psi. The sample was then immediately transferred to the carrier holder, and spun at 2000 RPM for 45 seconds. Spray-coating was later replaced by pipette-dispense for a simpler and more efficient process. The sample was baked at 180°C for 5 minutes on a curved aluminum mandrel placed on a contact hotplate to drive away the solvent. The radius of curvature of the mandrel was the same as that of the mirror. The 180°C baking temperature was measured on the mandrel surface prior to baking. After the sample cooled to room temperature, a positive-tone photoresist, SPR3012, was dispensed statically over the sample in full-area coverage and spun at 4000 RPM for 45 seconds. The sample was then baked on the preheated mandrel at 90°C for 2.5 minutes.

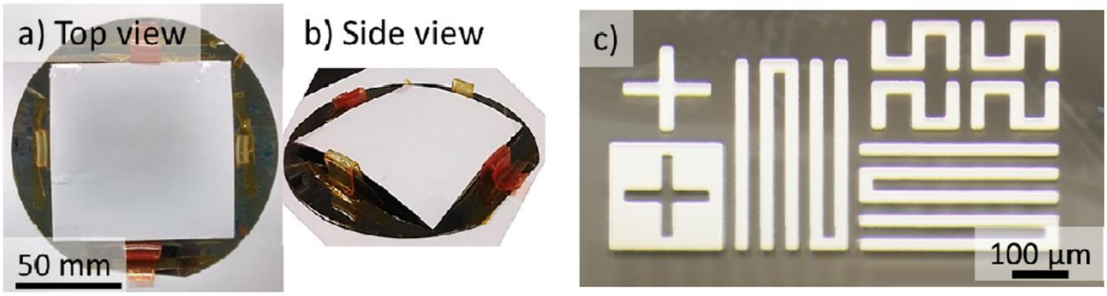

Figure 9-3. (a), (b) show the custom carrier holder developed for accommodating the curved glass mirror during photoresist spin-coating, which was a 6'' Si wafer base with four plastic stoppers securely attached. With the stoppers preventing the glass substrate from flying off the carrier, the spin speed could reach 3000 or 4000 RPM, resulting in significantly improved resist uniformity and minimizing the edge bead. (c) shows the achieved feature sizes of 25 µm line width and 25 µm line gap due to the improved spin-coating process. Figure reproduced from Walker et al. [11].

To expose the photoresist with the intended pattern, the flexible Mylar photolithography mask was manually centered and taped onto the mirror sample with Kapton tape. The top 3012 photoresist layer was then exposed using a Karl-Süss MA/BA 6 Gen 2 broadband contact aligner with 64 mJ/cm^2 UV dose

in the "lamp test" mode. Due to the curved geometry of the mirror, the contact aligner was used solely as a UV lamp source bypassing the aligning and the contact printing steps. The mirror sample along with the Mylar mask was placed on the substrate chuck right below the UV lamp, which was turned on and off by manually pressing the "lamp test" softkey. As the Gen 2 aligner uses time as the controlling parameter, the exposure duration was calculated by dividing the total UV dose by the lamp power. Regular calibrations were performed to correct for variations in the lamp power with time. At the time of HFDFC3 development, the power was 8 mW/cm^2 for the aligner used, which corresponded to an 8 second exposure time.

The exposed mirror sample was immersion-developed at room temperature for 70 seconds in a *MF CD 26 Developer* (Dow Chemical Co., Midland, MI) bath. The sample was rinsed with DI water for 1 minute and blown dry with compressed nitrogen gas.

A plasma ashing step was performed with the *M4L* system using the same conditions as mentioned earlier. Immediately following the plasma cleaning, the sample was loaded into the sputter system with the chamber pumped down to vacuum to minimize surface re-contamination. 100 nm thick Pt top electrodes were sputtered using the same system and conditions as the bottom electrode (excluding the Ti).

The metal lift-off was carried out with the mirror sample immersed in a ~50°C acetone bath; it was removed from the bath after the electrode pattern was completely formed. As LOR resists are not soluble in acetone, the sample was then placed in a second bath of ~50°C N-Methyl-2-pyrrolidone (NMP) for 10 minutes for LOR1A removal. The mirror with patterned Pt was rinsed with DI water and blown dry with compressed N_2 gas. NMP is commercially available as the solvent itself but can also be accessed as the active ingredient in resist strippers such as PRS 3000 (J. T. Baker) and Remover PG (MicroChem).

5.3.3 Bonding flexible ribbon cables using ACF

External electrical connections were established by bonding flexible ribbon cables to the mirror using anisotropic conductive films (ACFs). Detailed explanation of this process can be found in Chapter 3 along with descriptions of cable fabrication.

The Cu traces on the ribbon cables were designed to match the pattern of the bonding pads on the mirror. The shape and dimension of each cable was designed based on the geographical arrangement of the mirror with respect to the ZIF connectors on the mounting fixture. The mounting fixture was developed at SAO and the dimension guidelines were provided to PSU. A total of six cables were prepared for the six bonding-pad clusters. Although both the bonding pads and the cable traces had a 1 mm pitch, the line width on the mirror side was designed to be 0.5 mm as opposed to the 0.75 mm. The narrower design on the cable side was intended for easier alignment if the contacts on the lower level (mirror) could be seen. The cables for the two 14-pad clusters were designed with seven extra Cu traces in order to include the bottom electrodes 5 mm away from the top pad.

A curved vacuum mandrel was designed to support the glass substrate during ACF bonding and drawn with the Solidworks software as shown Figure 5-4 (a). The mandrel was consisted of a curved section with matching 220 mm ROC to vacuum-hold the mirror and a flat section to hold the flexible cables with a separate vacuum plumbing. The two sections were joined with the flat portion 0.4 mm higher than the edge of the curved side. As this step-height matched the substrate thickness, the bonding region near the edge of the mirror was approximately in the same continuous plane as the flat part of the mandrel, permitting the cables to lay flat on the mirror while being held by vacuum on the flat mandrel side. Another important design specification was that the zenith of the curved portion was at a 4 mm lateral distance from the flat side. This was to match the 4 mm distance between the center of the ACF bonding pads and the mirror edge so that the ACF bonding pads could land on the zenith of the curvature and be perpendicular to the bonder's thermode for optimal pressure application. The mandrel was made from Glass-filled ULTEM® (polyetherimide) for its thermal stability, heat retention, and machinability to a smooth surface finish (preventing from scratching the mirror).

The mandrel was produced by the machine shop at Penn State, and the final product is shown in Figure 5-4 (b). Vacuum was created by pumping the mandrel with a Medo USA linear system vacuum pump (VP0140-V1006-D3-1053). The small vacuum holes at the surface were connected to the vacuum pathways running inside the mandrel body, which were terminated on the side of the mandrel as 8 large holes. Two of these holes were used as pumping ports and the rest were plugged with plastic fittings.

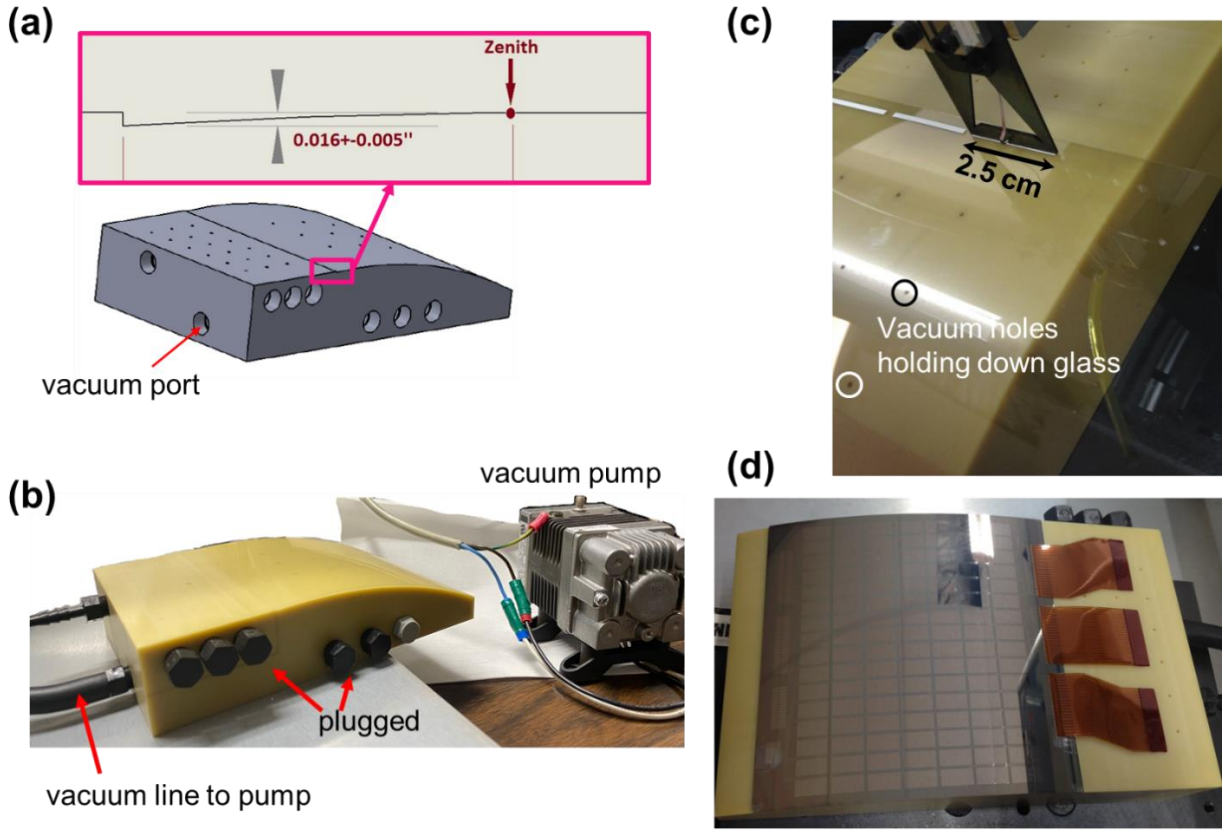

Figure 9-4. The mandrel for supporting, vacuum-holding, and orienting the mirror during ACF bonding. (a) The Solidworks drawing of the designed mandrel consisting a flat part for holding the cables and a curved part for holding the mirror. The vacuum holes at the surface were connected to the pathways in the body which were evacuated by a vacuum pump. (b) The mandrel was machined by the Penn State machine shop using glass-filled ULTEM® as the material. (c) The ACF tacking being performed on a bare curved glass on the mandrel for practice purposes. (d) An HFDFC candidate mirror having the ribbon cables finished bonding on one side.

With the mandrel supporting and orienting the curved mirror, ACF bonding was feasible as for flat substrates. The ACF strip was cut to the width of the ribbon cable and tacked onto the bonding pads on the mirror at 90°C for 10 seconds with 1 MPa pressure. Then, with the cable aligned to the bonding

pads, the thermode applied 1 MPa pressure at 190°C to cure the ACF and compress the conductive particles to facilitate the final bonding. Figure 5-4(c) shows the tacking process of the ACF on a piece of curved glass for practice purposes. The thermode could cover a maximum 2.5 cm bonding width in a single operation. Figure 5-4(d) shows an HFDFC mirror being held on the mandrel with one side completed for cable bonding.

5.3.5 Electrical property measurement and the defect-burnout treatment

The average permittivity and loss tangent of all 112 PZT cells were measured as 1270 and 0.047 using an LCR meter (Hewlett Packard 4284A) with 30 mV small signal excitation at 1 kHz [12]. 100% yield was achieved after applying the defect-burnout technique (mentioned below) to a few PZT cells with high loss tangents or shorted characteristics.

The defect-burnout technique is a procedure that runs high levels of current (10 mA-1 A) between the shorted contacts and vaporizes the conductive defects in the PZT along with the local electrodes via Joule heating [13]. The outcome is an insulating region surrounded by undamaged PZT. For HFDFC3, this was achieved by connecting the top and bottom Pt electrodes to four 1.5 V D-cell batteries in series for 5-10 seconds. The absence of current-limiting circuitry in these batteries could supply high levels of current to generate Joule heating. The post-treatment capacitance values were remeasured and compared with the nominal values to rule out large-area electrode damage.

5.3.6 Optical Characterization for HFDFC3

After actuator-side processing, HFDFC3 was taken to collaborators at SAO for mounting and optical characterization. During testing, the mirror was held vertically in the axial (flat) direction by seven flexure supports and one fixed support, as shown in Figure 5-5. The supports were part of an exterior housing, which also accommodated six small circuit boards with zero insertion force (ZIF) connectors. The flexible ribbon cables were inserted in to the ZIF connectors. The circuit boards were the interface

between the mirror and the control electronics: a custom 128 channel DAC electronics board capable of outputting voltages ± 15V DC. They were controlled by an Arduino and a Python interface [14].

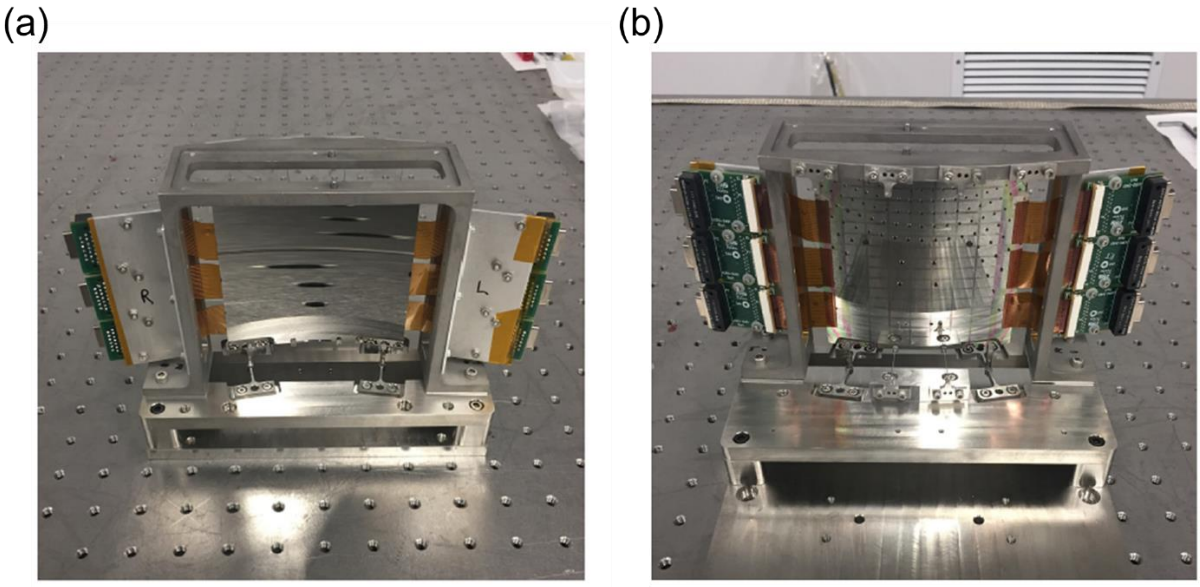

Figure 9-5. The fabricated HFDFC3 mirror piece on the mounting fixture showing (a) the concave side with Cr/Ir X-ray coating, and (b) the convex actuator side. The flexible ribbon cables are inserted into ZIF connectors on six circuit boards, which are to be connected to the control electronics. The figure is reproduced from DeRoo et al. [14].

The optical characterization setup was a cylindrical wavefront sensing system consisting of a Shack-Hartmann wavefront sensor (WFS) and a computer-generated hologram (CGH) [15-16]. A 635 nm laser source was collimated before arriving at the concave side of the adjustable mirror. The reflected plane wave detected by the WFS measured the absolute and relative figure change (influence function calibration) for the HFDFC3 part.

To assess the induced figure distortions after each step of thermal slumping, actuator layer processing, ribbon cable bonding, and flexure mounting, the absolute figure was measured on the WFS system by referencing an optical quality cylinder. As seen in Figure 5-6, the layer processing and mounting induced significant distortions that fell outside of the adjustable range of the PZT actuator cells, making it infeasible to correct the absolute figure for HFDFC3.

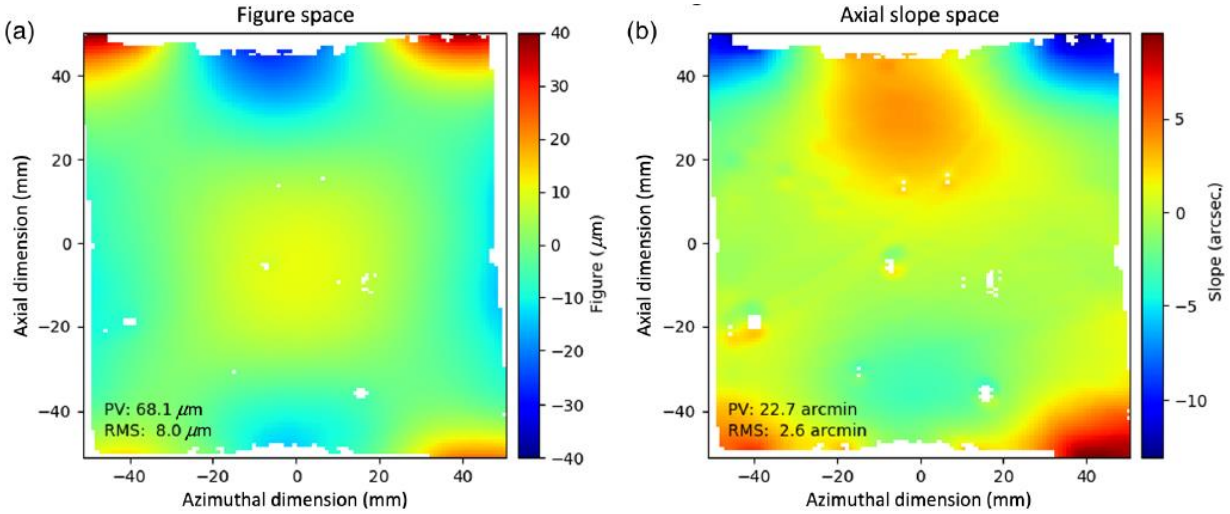

Figure 9-6. The absolute figure achieved in (a) magnitude and (b) axial slope, which was outside of the dynamic range of the PZT actuators. The figure is reproduced from DeRoo et al. [14].

The large distortions were addressed in the next generations of adjustable X-ray mirror prototypes, with a description found in Section 4.4.

Despite being outside the adjustable range for the absolute figure correction, the influence function (IF) data of HFDFC3 was used to demonstrate the ability to piezoelectrically induce figure corrections to an X-ray optic in a deterministic manner. The influence function was the difference of the wavefront measurements before and after activation of a PZT actuator. Prior to the measurement, each PZT cell was poled at 10 V ($2.2\times E_c$) at room temperature for 40 minutes using the control electronics. The poling increased the dynamic range for the actuators. The influence function calibration was carried out by measuring the relative figure change induced by actuating each PZT cell at 10 V and taking an average of 10 data points. Over 112 cells, the IF demonstrated an average figure change of ~1 μm peak to valley (PV) induced by activating each cell at 10 V DC. An example of the IF showing the response of a single cell is plotted in Figure 5-7.

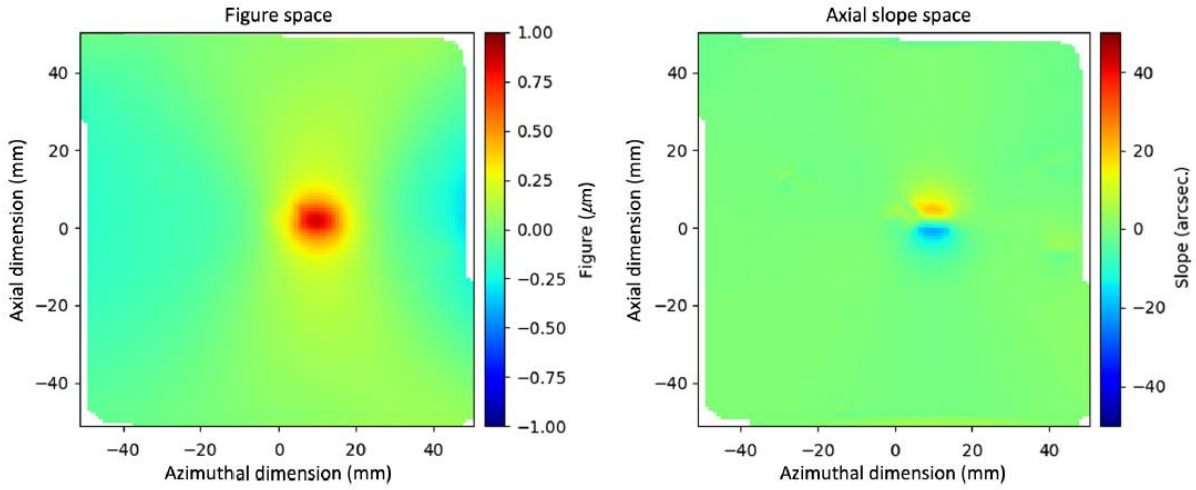

Figure 9-7. The amplitude (left) and shape (right) of the influence function upon actuation of the cell in Row 8 Column 5 (Row 1 Column 1 as the upper left cell). Figure reproduced from DeRoo et al. [14].

The calibrated IFs were used to simulate the correctability for 7 to 10 arcsec HPD. A 1 to 3 arcsec half-power diameter (HPD) simulated performance was achieved after applying the correction algorithm, demonstrating the ability to piezoelectrically induce figure corrections to an X-ray optic in a deterministic manner.

5.3.7 Cr/Ir X-ray coating

Upon completing the actuator device processing, 20 nm thick Cr and 400 nm thick Ir were sputtered on the front side of the mirror to serve as the X-ray reflective coating. The two metal layers were deposited in the sputter system used for Ti/Pt deposition without breaking the vacuum. The process pressure was 7.5 mTorr for Cr and 11 mTorr for Ir.

5.4 Reducing process-related figure distortion

Figure distortions due to mounting and processing in HFDFC3 exceeded the correctable range of the piezoelectric adjusters. To prepare the next generations of X-ray prototype mirrors with reduced distortions, modifications were made to the PZT crystallization conditions to achieve a lower integrated

stress, a stress-balancing coating was applied to correct the radius of curvature, and a new low stress mirror mount was developed to mitigate the mounting impact. A summary of these three measures follows; a detailed version of the content can be found in [14].

Subsequent investigation revealed that the nonuniformity of the distortion was caused by a large temperature gradient ($\Delta T>80°C$) during PZT crystallization in the RTA system. As a solution, a box furnace with a significantly lower temperature gradient ($\Delta T<10°C$) was used to crystallize the PZT films. The amplitude of the total integrated stress was reduced by decreasing the PZT crystallization temperature to 550 °C and decreasing the bottom Pt thickness to 50 nm.

The second approach to further correct the process-induced distortions was to counteract the integrated stress on the convex side of the mirror by producing same stress in the Cr/Ir X-ray coating on the concave side, as shown in Figure 8. Both films are under tensile stress.

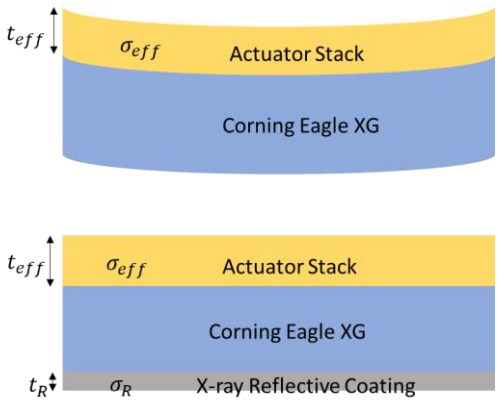

Figure 9-8. To correct the curvature change of the mirror due to the integrated stress in the actuator stack, an X-ray reflective coating of the same stress state can be applied on the opposite side of the mirror (image courtesy of Nathan Bishop at Penn State).

Using the notations in Figure 5-8, the stress balancing equation can be written as $t_{eff}\sigma_{eff} - t_R\sigma_R = 0$, where t and σ are the thickness and the residual stress, respectively. The integrated stress experienced by the film can be calculated using the Stoney equation (Equation 5-1).

$$t_f\sigma_f = \frac{E_s t_s^2}{6R(1-\vartheta_s)} \tag{5-1}$$

where $t_f\sigma_f$ is the film thickness × film stress, E_s is the Young's Modulus, t_s is the substrate thickness, R is the change of radius of curvature, and ϑ_s is the Poisson's ratio of the substrate.

The stress of the metal film can be scaled by adjusting the film thickness and the process pressure during sputter deposition [17-19]. As Cr was under 5 nm, the stress of the Ir layer was regulated.

A curved mirror piece with a 135 MPa integrated stress from actuator stack processing was used to demonstrate stress-balancing. The experimental stress profile of the sputtered Ir film per micron as a function of process pressure is plotted in Figure 9. The data points were collected on Ir films deposited on 0.4 mm thick, 100 mm × 100 mm flat Corning XG glass substrates. Use of flat substrates allowed use of a contact profilometer to measure the radius of curvature change.

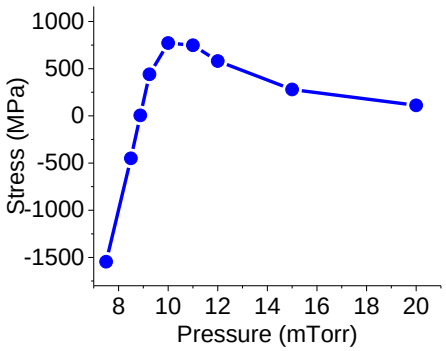

Figure 9-9. Experimental stress profile of the sputtered Ir film per micron as a function of process pressure (experienced by the glass substrate). The stress experienced by the Ir film takes the opposite sign (image courtesy of Nathan Bishop at Penn State).

According to Figure 5-9, the stress balancing layer for compensating the 135 MPa·μm tensile stress was therefore a 50 nm thick Ir at 5 mTorr process pressure using the same sputter system for Pt and Ti deposition. The actual stress induced by the Cr/Ir stack was 147 MPa·μm, within 9% of the target integrated stress.

Besides the improvements made at the processing front, the collaborators at SAO developed a low stress mirror mount to reduce the mounting-induced impacts on mirror figure [20]. This new

apparatus contains four lateral (along the azimuthal direction) supports connected to a stiff frame by means of four clip-flexure structures.

5.5 Prototype C1S pseudo-conical optics

The succeeding generation of the HFDFC series was a set of mirrors having pseudo-conical geometry with a Wolter profile. The mirrors were thermally formed on a conical mandrel and had figure errors inside the correction range of the actuators.

5.5.1 New pattern design and two-level metallization

To increase the active surface and the resolution of figure correction, the actuator cells were reduced to 5 mm × 5mm squares separated by a 0.2 mm alley way distance. The finer cell division yielded a matrix of 288 cells; they were re-arranged in 18 rows by 16 columns. They were connected to two identical columns of ACF bonding pads on either axial (flat) mirror edge. The bonding pads were bundled into eight clusters, separated by a distance reserved for the mounting clips. The ACF bonding pads were arranged at a finer 0.5 mm pitch to accommodate the larger cell number. C1S mirrors retained a single ACF pad column on both edges.

Due to the reduced alley way distance and increased PZT actuator density, the curved-substrate photolithography resolution no longer permitted the metal traces to route through the gaps between pixels to reach the ACF bonding pads. As a result, a two-level metallization was employed to accommodate the denser cell arrangement (Figure 5-10).

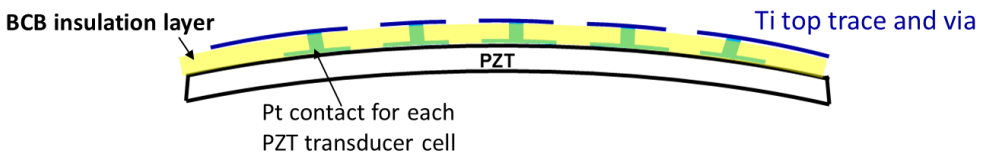

Figure 9-10. Schematics of two-layer metal contact regime. Ti is connected to the Pt contacts through the insulating layer BCB.

In this process, an insulation interlayer was deposited and patterned over the 288 Pt top electrodes, then a second metal layer was deposited to access the Pt through the insulation. The second metal layer was patterned and routed to the ACF bonding pads over the insulation layer. ~1 μm photo-patternable benzylcyclobutene (BCB) was chosen as the insulation layer for its low stress profile and its compatibility with PZT and ZnO thin-film transistor (TFT) processing (for future prototype development) [21-22]. Contact profilometer measurements were conducted on a 1.1 μm thick BCB film formed on a 100 mm × 100 mm × 0.4 mm Eagle EG substrate to assess the resulting stress level. As shown in Figure 11, the BCB layer produced a uniform tensile stress level of 12.8 MPa.

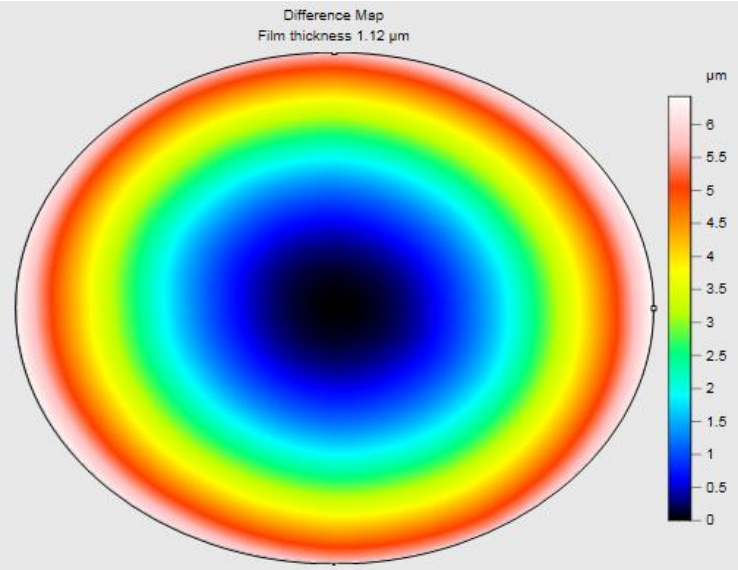

Figure 9-11. Profilometry shows small, uniform stress introduced to the glass substrate after a 1.1 μm thick BCB was formed on a flat 100 mm × 100 mm × 0.4 mm Eagle EG substrate.

The two-layer metallization required a set of three lithography mask layers with each aligned to the preceding layer. The masks were made with flexible Mylar films and were taped onto the mirror during exposure. Figure 5-12 shows the L-Edit design of each mask layer and their role in forming one actuator cell:

(1) Pt top electrodes defining the independent pixels of 5 mm × 5 mm squares with 0.2 mm gap arranged in 18 rows and 16 columns; the actual mask had a dark-field polarity for lift-off.

(2) Vias through the BCB layer, indicated by the black square of 1 mm × 1 mm centered within the pixel; the actual mask had a bright-field polarity due to the negative tone of BCB.

(3) The top level Ti metal layer accessing the Pt in Layer 1 through the BCB vias of Layer 2; the top level traces were fanned out to the mirror edges to form contact pads for cable bonding. To facilitate lift-off, this was also dark-field.

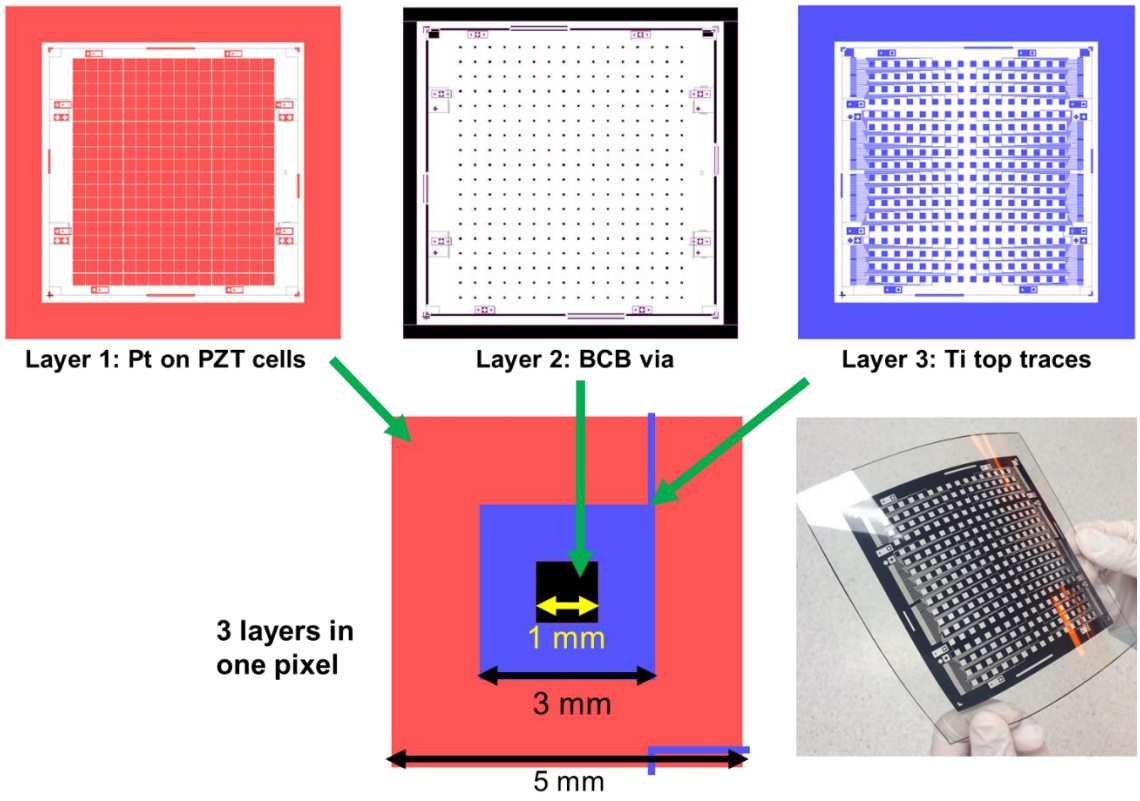

Figure 9-12. The photolithography mask set comprising three layers for defining the pattern of (1) Pt top electrodes on PZT, (2) vias in the BCB insulation layer, and (3) Ti second metal layer for fanning out the Pt contacts to the cable bonding pads.

The full stack with three layers superimposed is illustrated in Figure 5-13. The columns are parallel to the optical axis (flat edges) and the rows are parallel to the azimuthal axis (curved edges). The smaller ROC of the pseudo-cylinder is located at the top azimuthal edge. Two rectangles near the smaller ROC corners are reserved as bottom electrodes. Kapton tape masked the platinum bottom layer prior to the PZT sputter deposition to gain access to the bottom electrodes. Eight clusters of ACF bonding contacts are located at the two axial edges; these were attached to eight flexible ribbon cables. The Ti

bonding pads connect to all 288 actuator cells and the two bottom electrodes through the BCB insulation layer. The pitch dimension for the bonding pads (and for the ribbon cable traces) was reduced from 1 mm to 0.5 mm in order to accommodate the increased number of pixels. Alignment markers are situated at 8 places near the edges of the mirror; the ones between the bonding pad clusters use the space reserved for mounting clips. Patterns facilitating rough alignment of the mask to the substrate were placed at all edges and corners; these consisted of clear polygons to facilitate visualization through the mask and locate the overall frame of the mirror underneath. The minimum features were 150 μm for line gap and 100 μm for line width.

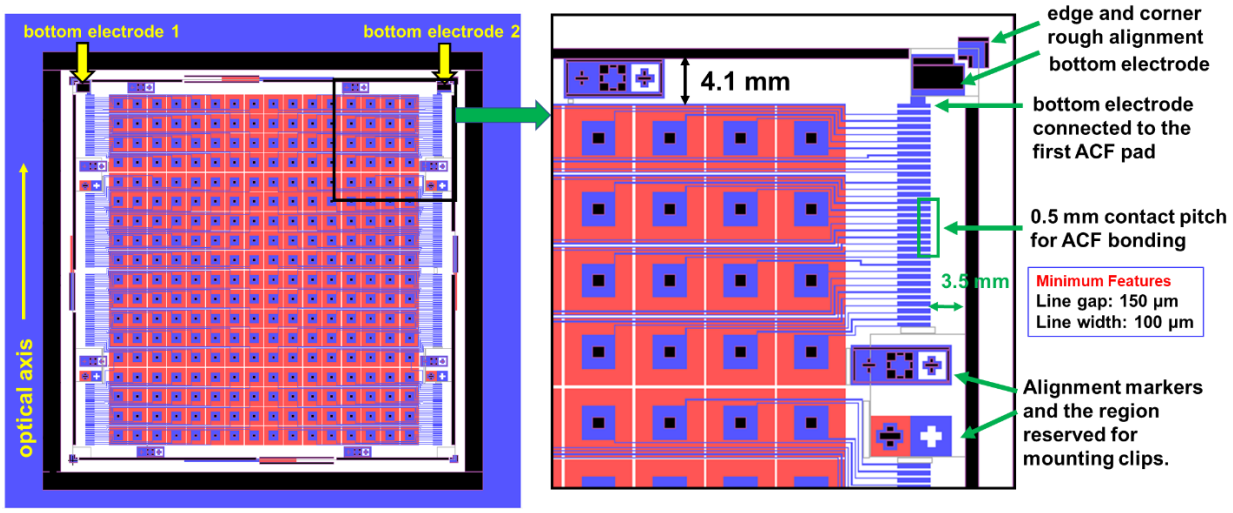

Figure 9-13. An overall view of the actuator pattern with all three device layers superimposed. Important design features are labeled and explained with the close-up view at a region near one mask corner.

As can be seen in the schematic of a single pixel in Figure 5-12, fitting a 1 mm × 1 mm square inside a 5 mm × 5 mm square tolerates large alignment error. The mask-substrate alignment was therefore achievable by naked-eye visualization and barehand manipulation. The alignment mechanism was upgraded for the mirror prototypes developed after June 2019 when a customized Hybrid Technology Group (HTG) aligner was introduced to the study to process the TFTs. The custom aligner was able to achieve the flexible mask-to-mirror alignment with proximity contact and UV-exposure with vacuum

contact. The aligner was developed by Mohit Tendulkar in the Jackson's research group at Penn State. Alignment error of less than 10 µm across the entire substrate was achieved [23].

5.5.2 C1S04 Fabrication

The conical mirror developed for X-ray testing in this work is named "C1S04".

C1S04 fabrication began with the cleaning procedures described in Section 4.3. A 2 nm thick Ti adhesion layer and a 50 nm thick Pt layer sputter-deposited without breaking vacuum made up the bottom contact. The sputter-deposition of the PZT layer was performed by Nathan Bishop at Penn State and the process is detailed in section 4.3. Each 0.5 µm thick PZT layer was sputtered at room temperature and crystallized in a box furnace with a temperature gradient less than 10°C. The temperature of the furnace was increased from ambient to 550°C at a 10°C/min rate, then held at 550°C (set as 578°C) for 1080 minutes. For this step, the mirror piece was placed inside a quartz sleeve to minimize particle contamination. The sputter/crystallization step was repeated for 3 times until a film thickness of 1.5 µm was achieved. Despite having less thermal gradient, the box furnace use had two major drawbacks. First, compared to the RTA crystallization, the process was much more time-consuming. Second, as the box furnace was unsuitable to be placed in a cleanroom environment due to the insulation material, the PZT film was more susceptible to particle contamination during crystallization and being transferred in and out of the cleanroom after sputtering.

After the top electrode formation on the PZT layer, capacitance and dielectric loss were measured on each pixel using a Hewlett Packard 4284A LCR meter with a 30 mV ac excitation at 1 kHz. 99% device yield was achieved as 3 out of the 288 PZT capacitors showed high dielectric loss (>10%).

Photo-patternable BCB, CYCLOTENE 4022-35 (Dow Chemical) was diluted with mesitylene (Sigma Aldrich) at a ratio of 1.7:1 (one part mesitylene) to tune the film thickness upon spin-coating. The diluted solution was dispensed statically over the mirror sample in full surface coverage and spun at 3000 RPM for 40 seconds using the custom holder. The mirror piece was then transferred to a 65°C preheated aluminum mandrel on a hotplate for a 3 min soft-bake. Next, the flexible mask was taped onto the mirror

and the BCB was exposed on a MA/BA 6 (SÜSS MicroTec) broad band aligner for 10 seconds (a total of 80 mJ/cm^2 UV dose). The mirror underwent a post-exposure bake at 65°C on a preheated mandrel for 5 minutes immediately before immersion-developing in a DS3000 developer bath at 40°C for 8-10 minutes. It is to be noted that the developing time recommended by the manufacture is 2-4 minutes [24]. The prolonged developing time in this work was used to make up for the lack of vacuum contact between the mask and mirror during exposure. As BCB is a negative-acting photo-patternable polymer, light bled through the gap under a dark pattern on the mask and exposed the BCB around the edges inside the printed pattern. The exposed region was crosslinked and developed into a residue layer, as shown in Figure 5-14.

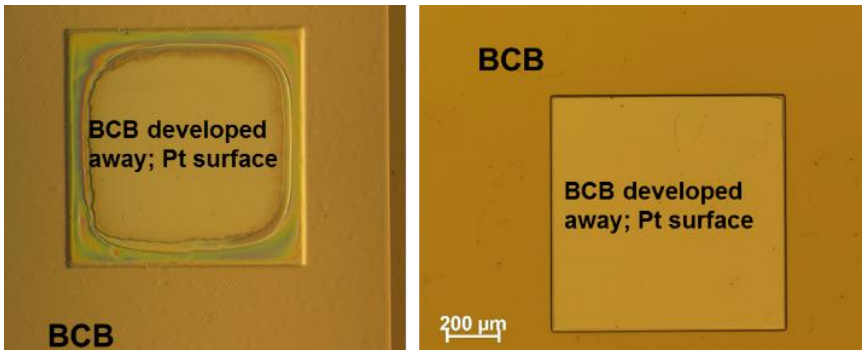

Figure 9-14. Due to the non-vacuum contact between flexible mask and curved substrate during exposure, UV light bled through the gap under a dark pattern and crosslinked the BCB at the edges inside the via, leaving a residue layer (left). 3× longer develop time and higher developer bath temperature mitigated the residue issue (right).

After developing, the mirror sample was transferred to a fresh DS3000 developer bath at room temperature and rinsed with fresh DS 3000 from a polypropylene squirt bottle. Without using other solvents or water, the DS 3000-wetted sample was blown dry with N_2 gas. BCB curing was carried out in a vacuum oven at 230 °C for 10 hours; a small amount of N_2 gas was bled continuously into the oven. The film should not be exposed to oxygen above 150 °C as oxygen interferes with the curing process [24]. The vacuum level was maintained at a pressure of -15 mmHg.

After the BCB layer was fully cured, a descum etch was performed to remove the BCB residue inside the via region. This residue layer, formed as a result of reactions in the developing process, is an

inherent feature of the CYCLOTENE 4022-35 BCB and thus unrelated to UV-crosslinking [24]. The etch was performed in a PT720 RIE system at -100V DC bias, 50 mTorr process pressure, and 36 W power with 80% O_2 and 20% CF_4 gas for 30 seconds. The silicon backbone in BCB was removed with fluorine [25]. The removal was confirmed by ellipsometry. Generally, this residue layer should be no thicker than 15 nm [24]. The final BCB layer thickness was around 1 μm.

Electrical properties were measured prior to the Ti deposition and the yield remained as near-perfect. The unchanged yield indicated that no degradation occurred to the PZT cells during the BCB layer development.

The top 100 nm thick Ti layer was deposited by DC magnetron sputtering in a Kurt J. Lesker CMS-18 system using the parameters listed in Table 4-1. The layer was patterned by the lift-off process following the details in Section 4.3.2. The top Ti layer connected the Pt contacts through the BCB and over the PZT actuator cells. The Ti traces were routed to the mirror edges to form contact pads for ribbon cable bonding.

5.6 C1S04 rework and recover

Before attaching the flexible ribbon cables to C1S04, capacitance and dielectric loss were measured for each pixel to assess the actuator yield using a Hewlett Packard 4284A LCR meter with a 30 mV ac excitation at 1 kHz. Testing on a probe station, with one probe contacting the Ti/Pt top contact inside the via window while the other probed the ground electrode, 85% of the cells showed a dielectric loss tangent larger than 10%. The 15% appallingly low yield was the result even after a defect-burnout treatment (section 4.3.3) with 6 V D-cell batteries. This yield is substantially lower than results achieved without the Ti traces.

Since the PZT devices had a near-perfect yield before the BCB processing, the point of failure likely occurred during the subsequent Ti step. In order to understand the failure mechanism and to

develop a pathway to rework the mirror piece, C1S04 was reprocessed to remove the Ti traces and the BCB, so that only the patterned top Pt contacts on the PZT actuator layer remained.

5.6.1 Ti and BCB removal

For the first rework step, the top Ti layer was removed by reactive ion etching in the PT 720 RIE system (PlasmaTherm) in a mixed Ar, O_2, and CF_4 glow discharge. Fluorine radicals react with Ti and form volatile etching products such as TiF_3 and TiF_4 [26]. Oxygen was added to the gas mixture to enhance the atomic fluorine production [26-27], since the atomic fluorine is an effective etching agent of Ti and its native oxide [28-29]. Ar gas was added to increase physical bombardment in the etching process. As the Ar, O_2, and CF_4 plasma combination also attacks BCB, the etching parameters were pushed towards a chemical etch-dominant mode to avoid roughening or grossly etching the BCB layer. The chemical etch-dominance was achieved by keeping the physical bombardment low (e.g. by using only a small amount of Ar) and the process pressure high, to increase gas-phase scattering. The etching conditions are summarized in Table 5-2.

Table 9-2. Ti dry-etch parameters in the PT720 RIE system.

	Ar: O_2: CF_4 gas flow ratio	Pressure [mTorr]	DC bias [V]	Resulting Power [W]	Etch rate
Value	1:1:4	150	65	60	≈60 Å/min

After Ti was completely removed, around 400 nm thick BCB remained. As the optical microscope images show in Figure 5-15, there were no signs of roughening or damage to the BCB or the glass. The capacitance and loss tangent were measured on the LCR meter at 30 mV at 1 kHz. All the shorted pixels returned to the pre-BCB low-loss, functional state, which suggested that most of the conductive defects existed in the BCB layer and shorted the Ti to the underlying Pt contacts.

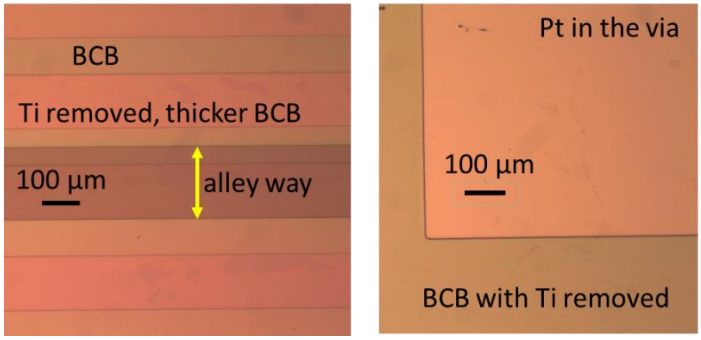

Figure 9-15. Besides thickness reduction, no signs of roughening or physical damages to the BCB were observed after removing the top Ti layer.

Two theories were proposed to explain the cause of the pinholes in the BCB layer. The first one related the defects on the flexible mask, which propagated into the BCB due to the negative tone of the photo-patternable polymer. As the regions protected from the UV will be developed away while the exposed region will crosslink and remain, non-transparent defects on the mask will result in the removal of the masked BCB, leaving a hole in the insulation layer, as schematically illustrated in the left panel of Figure 5-16. The Mylar masks were prone to have opaque defects from printing, handling, and repeated use (right panel of Figure 5-16) due to the lack of mechanical robustness. They were also difficult to clean due to the lack of chemical robustness. As a result, the BCB layer presumably developed a large number of lithography-induced pinholes across the curved substrate. The second theory hypothesizes that the BCB layer was attracting dust and particles upon spin-coating due to the tackiness of the uncured film surface. The contamination particles were then embedded in the BCB layer after curing. In addition, being handled by humans (more particle-generating than robots) and processed in university-level laboratories made it more susceptible to particle contamination.

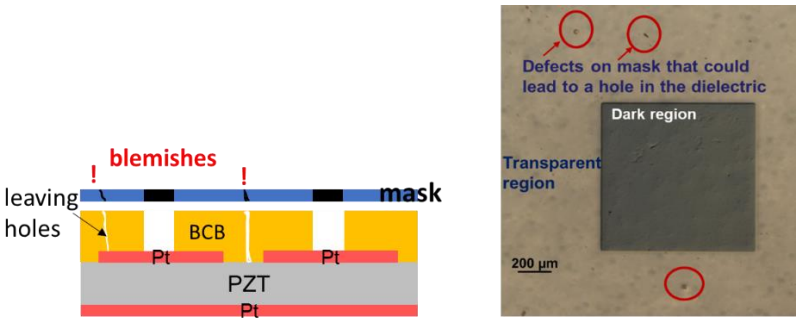

Figure 9-16. Non-transparent defects on the Mylar masks, such as imperfections from printing and wear from use, likely resulted in a large number of pinholes in the BCB layer.

After discovering the cause of the low yield, the remaining BCB was removed and a different insulation layer was considered.

An RIE dry-etch process was employed to remove the BCB film without damaging the actuators in the PT720 RIE system, using the conditions listed in Table 5-3. As previously explained for the BCB descum etch step, a fluorine-based plasma is necessary to remove the silicon in the BCB layer and keep the etch rate fast. It is especially critical to keep a fast etch rate here as the goal is to remove the entire BCB layer. Etching in pure oxygen plasma will hinder the etch process as it results in a nonvolatile silicon oxide layer [30].

Table 9-3. BCB etch conditions.

	O_2: CF_4 gas flow ratio	Pressure [mTorr]	DC bias [V]	Power [W]	Etch rate
Value	4:1	150	100	67	≈1200 Å/min

The capacitance and loss tangents were measured after all the BCB was removed. No damage to the PZT actuator properties was found.

5.6.2 Three individually cured BCB layers

To offset the defects and pinholes, three layers of BCB were formed on mirror C1S04 with each layer individually patterned and cured, as schematically shown in Figure 5-17. Using extended descum etching, the final thickness of the three-coat BCB measured 1.8-2 microns on a contact profilometer. The mirror was supported by a curved aluminum mandrel during the stylus scan. Because a mandrel that tilted and elevated the mirror was unavailable, the stylus of the profilometer was unable to scan the mirror along the curved axis direction near the flat edges. Therefore, BCB thickness data were obtained within the central 6 columns of the mirror.

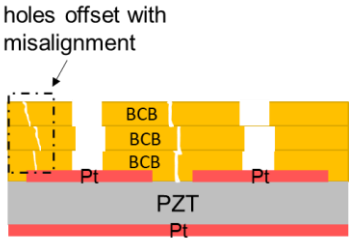

Figure 9-17. The single-coat BCB was replaced with three individually patterned and cured BCB layers to use the unintentional but desirable misalignment to offset lithography-induced pinholes.

A 100 nm Ti was subsequently sputtered and patterned over the BCB, completing C1S04 fabrication for the second time. Figure 5-18 shows the mirror upon fabrication. Pattern details of an individual pixel are found in panel (a), where the offset feature of the squares is a result of patterning three BCB layers using a single mask without proper alignment markers. The inadvertent misalignment was, in fact, a desirable feature for offsetting the defects and pinholes. Figure 5-18 (b) is an optical microscope image showing the details of the area outside of the pixel. An overall view of a complete C1S04 is shown in panel (c).

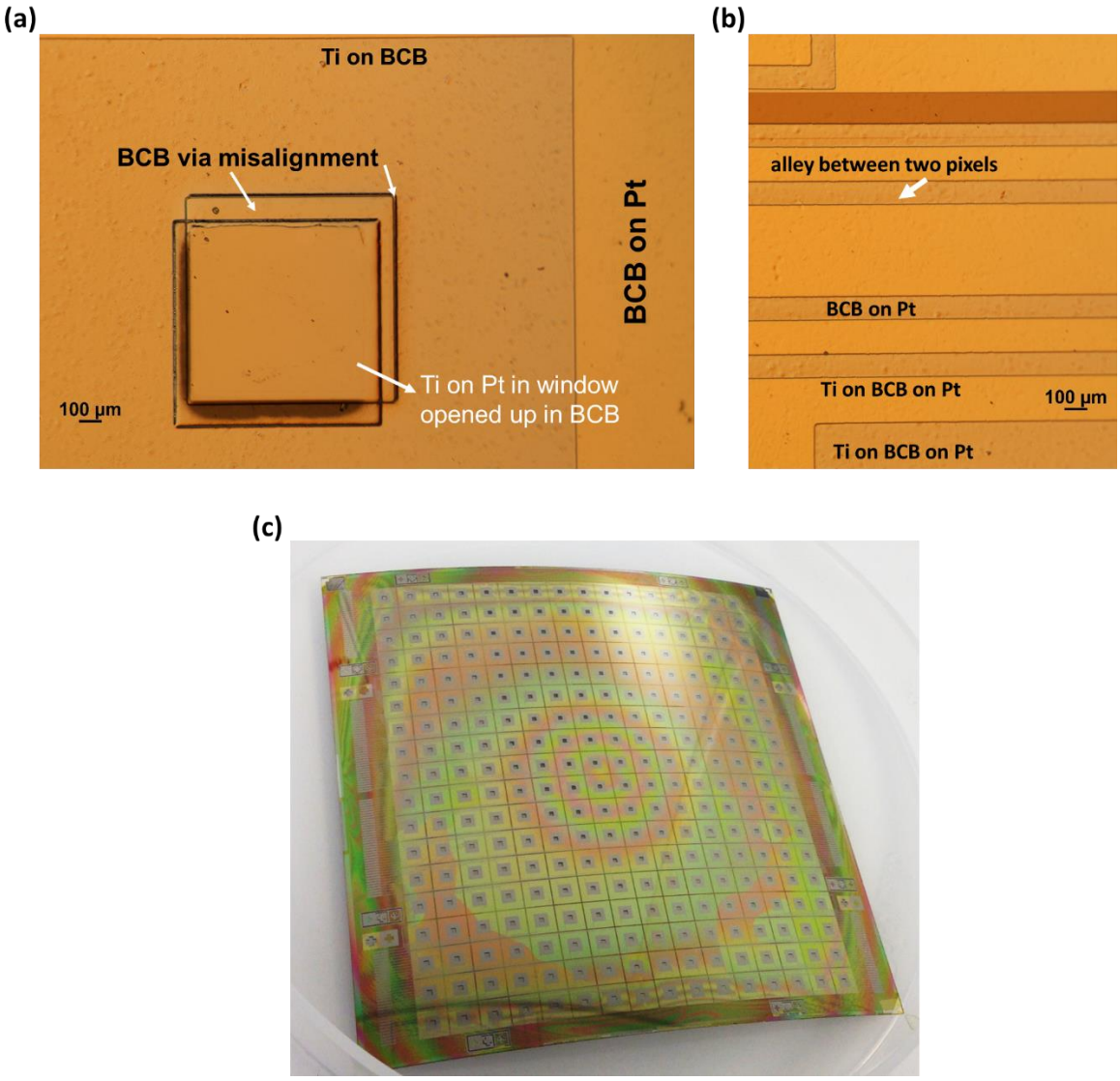

Figure 9-18. Pseudo-conical prototype mirror "C1S04" upon completion of the second fabrication attempt. (a) details around a pixel, including the offset of the BCB via from three lithography processes for each BCB layer deposition. (b) details outside of a pixel, showing the Ti traces routing through the alley ways. (c) an overall view of the C1S04 mirror prior to cable attachment.

5.6.3 Improved yield – 77%

With the multi-layered BCB as the insulation, the capacitance and dielectric loss tangent of the PZT actuator cells on C1S04 were measured on an LCR meter with 1 kHz, 30 mV sinusoidal excitation. A few of the shorted cells were healed when connected to 6 V batteries (defect-burnout technique), and the yield for C1S04 was increased to 77%, a drastic improvement compared with the 15% yield of the

previous iteration with a single coat of BCB. The yield map is shown in Figure 5-19 as a table of 18 rows and 16 columns with each cell mapping to the corresponding actuator cell. The table is oriented in the same manner as the design schematic in Figure 5-13, where row 1 is the row closest to the bottom electrode positions. Each cell in the table presents the measured data in the format of [capacitance (nF), dielectric loss tangent]. Those having a loss tangent higher than 9% are considered as a shorted cell and are highlighted in yellow. Among the shorted cells, some have the loss tangent recorded as "s" instead of an exact value. Pixels with a dead short showed unmeasurable loss tangents and incorrect capacitance values, which are then labeled as "short". The high-loss cells did not congregate in a particular region of the mirror, but the distribution was not completely erratic. They existed as clusters connecting two to eleven cells, and many cells exhibited a doubled, or nearly doubled capacitance value. This was an important piece of information that impacted the decision-making for the subsequent burnout treatment.

columns -->	1	2	3	4	5	6	7	8	9	10	11	12	13	14	15	16
rows 1	183,0.04	175, 0.04	169, 0.04	164, 0.04	160,0.04	157, 0.03	156,0.06	155,0.04	155,0.04	163, 0.04	260, 0.35	260, 0.35	162, 0.04	165,0.05	172, 0.04	180,0.05
2	180, 0.03	285,0.7	166,0.03	162,0.03	189,0.5	184,0.4	153, 0.04	152,0.03	152,0.03	153,0.03	154,0.03	short	159, 0.04	164,0.04	short	176, 0.04
3	178,0.02	201,0.3	158,0.03	158,0.03	155,0.03	153,0.045	151,0.03	167,0.3	150,0.03	151,0.02	151,0.02	154,0.02	157,0.03	260,0.4	167,0.035	275,0.4
4	175,0.03	167,0.03	161,0.03	156,0.04	153,0.03	150,0.03	176,0.3	148,0.03	158,0.05	148,0.03	149,0.03	151,0.03	154,0.03	160,0.03	165,0.03	172,0.03
5	195,0.2	165,0.03	251,0.4	250,0.5	151,0.04	148,0.04	147,0.3	146,0.03	147,0.03	235,0.5	177,0.3	291,0.3	305,0.2	157,0.03	164,0.03	170,0.03
6	171,0.03	164,0.04	157,0.03	153,0.03	149,0.036	174,0.3	146,0.03	227,0.4	145,0.035	247,0.3	145,0.03	150,0.025	151,0.03	157,0.03	162,0.03	169,0.03
7	199,0.2	158,0.8	286,0.3	151,0.03	148,0.03	231,0.4	263,0.5	202,0.6	143,0.03	143,0.02	146,0.035	247,0.3	150,0.02	155,0.03	161,0.025	168,0.03
8	175,0.04	167,0.05	161,0.04	short	153,0.04	290,s	149,0.04	short	218,0.4	218,0.38	144,0.04	146,0.03	150,0.03	190,0.3	160,0.03	167,0.03
9	300,s	294,s	165,0.04	155,0.04	154,0.04	191,s	194,0.05	222, s	142,0.03	142,0.03	146,0.03	146,0.03	151,0.025	188,0.3	159,0.03	178,0.03
10	167,0.03	173,0.05	117,7.0	225,s	274,s	155,0.06	154,0.06	146,0.04	177,s	142,0.03	145,0.024	146,0.03	149,0.025	155,0.05	159,0.03	166,0.03
11	175,0.04	187,0.27	162,0.04	165,0.04	152,0.04	157,0.05	148,0.04	174,s	148,0.03	189,0.5	202,0.5	146,0.02	149,0.03	155,0.03	159,0.02	193,0.4
12	177,0.05	169,0.045	163,0.045	157,0.045	154,0.045	151,0.045	150,0.04	158,0.05	150,0.04	148,0.04	144,0.03	144,0.03	150,0.03	156,0.04	159,0.045	178,0.03
13	183,0.05	171,0.045	172,0.04	159,0.04	155,0.04	151,0.04	150,0.04	155,0.04	238,0.36	148,0.80	145,0.03	147,0.02	152,0.03	155,0.03	160,0.03	168,0.03
14	181,0.04	173,0.04	166,0.04	161,0.045	157,0.03	155,0.035	152,0.04	160,0.04	210,0.4	152,0.04	146,0.03	148,0.03	153,0.03	158,0.03	163,0.03	169,0.03
15	176,0.02	168,0.03	161,0.04	156,0.03	152,0.02	150,0.04	148,0.03	153,0.2	193,0.43	147,0.03	180,0.4	153,0.03	154,0.03	158,0.03	372,0.3	325,0.4
16	178,0.03	170,0.02	164,0.04	159,0.02	155,0.02	150,0.02	150,0.02	150,0.03	150,0.02	150,0.03	245,0.4	153,0.025	154,0.02	184,0.3	166,0.03	187,0.034
17	301,0.3	173,0.02	288,0.35	162,0.03	158,0.03	155,0.02	153,0.03	152,0.03	191,0.37	152,0.02	153,0.03	165,0.04	159,0.03	163,0.03	168,0.03	175,0.055
18	short	176,0.02	169,0.02	164,0.02	160,0.02	286,0.3	371,0.4	210,0.5	154,0.02	154,0.03	166,0.03*	324,0.2	325,0.2	206,0.3	171,0.02	179,0.03

Figure 9-19. The yield map of the C1S04 PZT actuator cells upon re-fabrication with a three-layer BCB insulation. Each cell in the table maps to the corresponding actuator cell on the mirror based on the row-column coordination. The measured data is presented as [capacitance in nF, dielectric loss tangent]. The highlighted cells have the loss tangent >9% and the rest are considered as well-functioning cells. The yield is 77%.

5.6.4 Inter-pixel shorting

The current-voltage (I-V) characteristics at DC were measured using a *hp* 4156B semiconductor parameter analyzer to assess the leakage current level in the PZT capacitors. The measurement was initially conducted between the top and bottom electrodes, and the results were compared between high-loss and low-loss cells. While the low leakage current levels in the range of 10^{-7} A to 10^{-6} A for low-loss

cells was expected, strangely, a similar current level was also measured for many high-loss cells. This observation implied that a conducting path was perhaps not between the top and bottom electrodes on the PZT. Referencing the capacitance values provided the hint: as many high-loss cells showed a doubled, or nearly doubled capacitance, and this capacitance matched that of another cell, these top electrodes were likely shorted to each other. This hypothesis prompted measurement of the I-V characteristic between neighboring cells that showed matching high capacitance. A high current level was observed as predicted, which indicated that many of the high-loss cells were in fact shorted to each other either in pairs or in larger sized-clusters. In other words, a conducting path existed between the top electrodes of the shorted cells, presumably through the BCB.

The origin of the high measured loss tangents was revealed when the properties were tested as a function of frequency. Figure 5-20 contains four plots of the capacitance and loss tangent evaluated between 20 Hz and 10 kHz for randomly selected two pairs of shorted PZT cells. The data werre collected by Nathan Bishop at Penn State. As can be seen in all four graphs, at ~1 kHz, an RC time constant roll-off occurs; high apparent losses appeared when this roll-off matched the frequency at which loss tangents were collected for the data table in Figure 19. The RC time constant is a function of the device capacitance, the defect resistance, and the resistance of the Ti trace between the top contact and the defect. As these contributors vary from pair to pair, it explains the minor deviation of the curves from cell to cell. Testing at 20 Hz on the LCR meter (below the relaxation frequency) yielded an average loss tangent of 3-4% for the cells that were lossy at 1 kHz but had low leakage current with respect to the bottom contact.

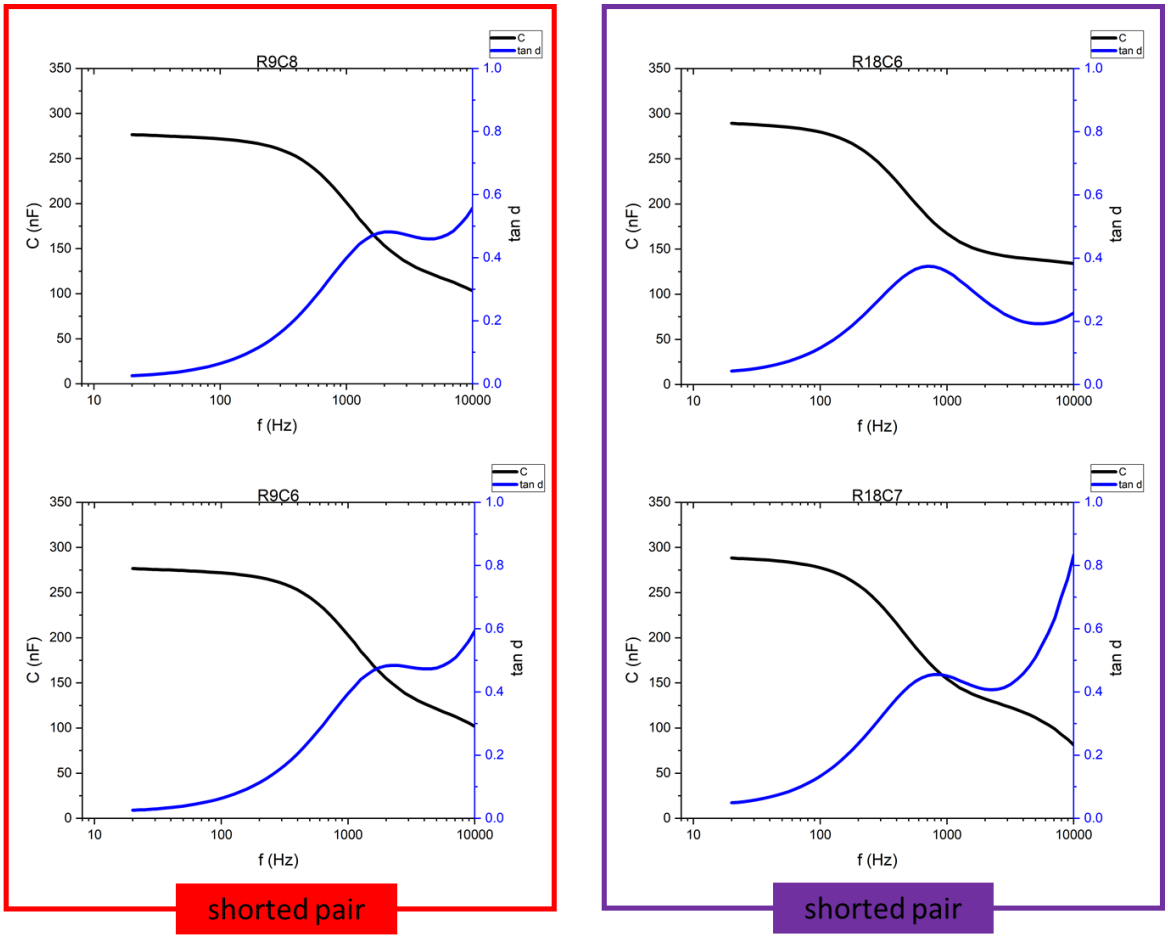

Figure 9-20. Capacitance and loss tangents of two pairs of shorted PZT cells (Row 9 Column 8 and Row 9 Column 6, Row 18 Column 6 and Row 18 Column 7) measured as a function of frequency from 10 Hz to 10 kHz. The plots reveal that the frequency roll-off point is near 1 kHz, the frequency at which the data were collected for determining the device yield (image courtesy of Nathan Bishop).

The I-V characteristic was not only a measurement for evaluating the shorting paths, but also a means to apply a DC voltage across the two shorted electrodes to induce high currents for burning out the conducting filaments (which was done with end-point monitoring). The maximum current compliance for the *hp* 4156B parameter analyzer was 100 mA, sufficient to cause most of the defects to vaporize. In general, the burnout treatment began by surveying the cell map and the data table to locate the shorted cell pairs or clusters. For a high-loss, double-capacitance cell, "A", suspected of inter-cell shorting with cell "B", the cell map was initially surveyed in the vicinity of "A" to identify the possible "B" suspects, which were its immediate neighbors in the adjacent rows and columns, or any of the underlying cells

overlapped with the trace routed from "A". The data table was then examined among the "B" suspects to recognize the ones that possess a similar capacitance value and a high loss tangent at 1 kHz. The I-V characteristic measurement was then performed between "A" and the "B" suspects to confirm the electrical short and vaporize the conducting filaments.

An example of separating the cell at Row 6, Column 10 from its shorted counterpart is described in Figure 5-21. Based on the cell map in Figure 5-21 (a), the cell at Row 6, Column 10 is likely to be shorted to its four immediate neighbors at Column 9 and 10 in the same row, and the ones at Row 5 and 7 in the same column. It is also possible to be shorted to cells from Columns 10 through 16 in the lower row as the Ti trace is routed over the Pt top contacts of these cells. By examining the capacitance and loss tangent values in the data table in panel (b), its shorted counterpart can be identified at Row 7, Column 12, for which an identical capacitance – 247 nF was observed. The current characteristics under applied 0-10 V DC excitation confirmed the presumed connection between the two cells. As seen in the left plot of Figure 21 (c), a linear current characteristic in the 10^{-3} A level is observed between 0 to ~4 V, which clearly indicates that a shorting defect exists between the two cells, presumably between the Ti trace of cell Row 6, Column 10 and the Pt top electrode of cell Row 7, Column 12 through the BCB interlayer. The current plummeted after ~4 V was applied, when the conducting defect vaporized, and the two shorted cells became electrically isolated. The separation was further confirmed by a 10^{-7} A current level measured after burnout, as shown in plot (ii) of panel (c). Plot (iii) confirmed the low leakage current with respect to ground after burnout. Both cells showed a 10^{-7} A current level.

(a)

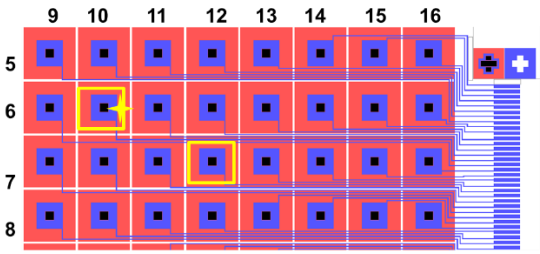

(b)

row \ col.	9	10	11	12	13	14	15	16
5	147,0.03	149,0.03	150,0.03	151,0.03	159,0.03	157,0.03	164,0.03	170,0.03
6	145,0.04	247, 0.3	145,0.03	150,0.03	159,0.03	157,0.03	164,0.03	170,0.03
7	143,0.03	143,0.03	146,0.03	247,0.3	150,0.02	155,0.03	161,0.03	169,0.03
8	218,0.4	218,0.4	144,0.04	146,0.03	150,0.03	190,0.03	160,0.03	168,0.03

(c)

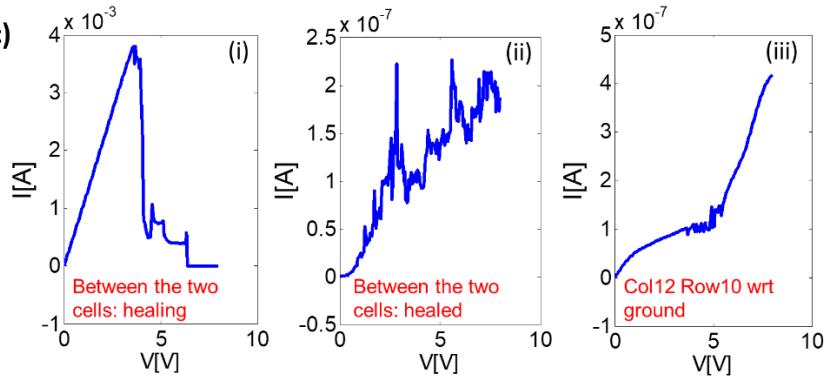

Figure 9-21. For separating the actuator cell at Row 6, Column 10 from its unknown shorted counterpart, the cell map in (a) was surveyed to first locate the possible candidates, followed by the survey of the data table of (b) to pinpoint the cell based on capacitance and loss. (c)(i) The DC current-voltage characterization was used to confirm the existence of the shorting path as well as to burn out the defect. The drastic current drop at ~4 V indicates the successful vaporization of the conducting defect. (c)(ii) The current level between the two cells after burnout is in the low 10^{-7} A level, similar to (c)(iii), the leakage current level of the cells with respect to ground.

The probes for applying voltage and measuring current were placed on the top Ti/Pt contacts inside the BCB vias as opposed to the ACF pads; this kept the contact resistance between the two pixels low (assuming the defect(s) exist(s) in the BCB layer in the region above the top Pt electrode). Keeping a lower contact resistance would enable a higher current to be supplied to the defect(s) for a more effective vaporization.

Being able to monitor the electrical current level during the burnout treatment provided useful information on the characteristics and the state of the conducting defect. An example in the next section

demonstrates how such information can contribute to the decision-making for effective defect elimination.

5.6.5 Laser-cutting for bridging-metal removal

While surveying the cell map and data table, neighboring cells at Row 1, Col 12 and Row 1, Col 11 showed identical, large capacitance values. Under an applied DC voltage sweep from 0 to 15 V, the leakage current between the two cells exhibited a metal-like linear characteristic with high amplitude and low resistance (Figure 5-22 (a)). This result suggested that vaporization by Joule heating would likely be ineffective. Therefore, the mirror was carefully inspected through an optical microscope in the vicinity of the two cells. Figure 5-22 (b) revealed that a piece of Ti had failed to lift off during the patterning step and bridged the two Ti traces of the two shorted cells.

Instead of inducing Joule heating, a Nd:YAG laser was used to vaporize the bridging Ti piece. The laser-cutter tool (New Wave Research) produced a pulsed laser beam with ~50 μm spot size, about half of the Ti trace gap. This dimension left ample clearance for the laser beam to act upon the bridging metal without damaging the Ti traces. Only 50 nm of the BCB layer underneath the targeted Ti was removed at the same time. During the cutting procedure, the mirror was placed on a curved aluminum mandrel on a stage that moved linearly in the *x* and *y* direction. The laser beam was visualized using a microscope (Figure 5-22 (c)). As shown in the top image of panel (c), the laser incident started on the left edge of the bridging piece and in the middle of the trace gap. Then, it gradually moved to the right-hand side (*y* direction) parallel to the two Ti traces in a step size about half of the laser spot diameter. The laser terminated outside the right edge of the bridging piece. With the Ti bridge showing a burnt-like appearance (panel (c), bottom), the laser had vaporized the bulk of the undesired metal and left the Ti traces elsewhere intact. A follow-up I-V measurement confirmed the isolation of the two cells.

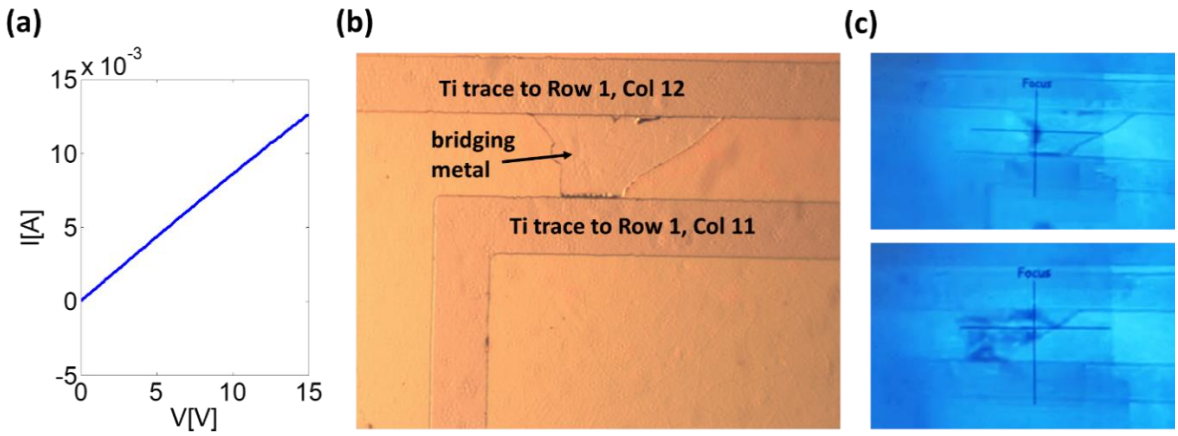

Figure 9-22. (a) The DC leakage current profile between the two shorted cells under investigation showed a linear characteristic and high amplitude. (b) Through microscope observation, the shorting defect was discovered as a Ti piece bridging the two Ti traces connected to the two cells of interest. The bridge was a result of lift-off failure. (c) The starting point of the laser-cutting process for the bridge removal (top), and the process upon completion (bottom). The laser impacted area showed a burnt-like appearance.

Five more pairs of actuator cells were found to be shorted as a result of bridging Ti pieces due to lift-off failure. These shorted cells were all successfully separated by vaporizing the bridging metal with the laser-cutter. Had the leakage current profile been unknown, none of the twelve cells could have received effective burnout treatment for electrical isolation.

5.6.6 Pogo pins

The effectiveness of the burnout treatment plateaued out as several pairs of shorted pixels could not be recovered by the parameter analyzer despite reaching the maximum current compliance. To circumvent this problem, the micromanipulator probes were changed. The probes mentioned here refer to the needle-like structures held by micromanipulators connected to testing instruments at a testing probe station.

Two types of probes were used in the parameter analyzer measurements and burnout procedures: tungsten needle probes with 0.5 μm tip radius and spring-loaded pogo pin probes with 100 μm tip radius. Switching from the tungsten probes to the pogo pins was game-changing for the defect burnout process. The large contact area between the pogo pin tip and the actuator electrode allowed higher current to pass,

thus vaporizing the defects more effectively. Multiple shorting defects that were unhealable by the tungsten probes were all vaporized when pogo pins were used. Figure 5-23 shows the scale of the pogo pins in reference to patterns on the mirror and a worm-like defect cluster along a segment of the Ti trace.

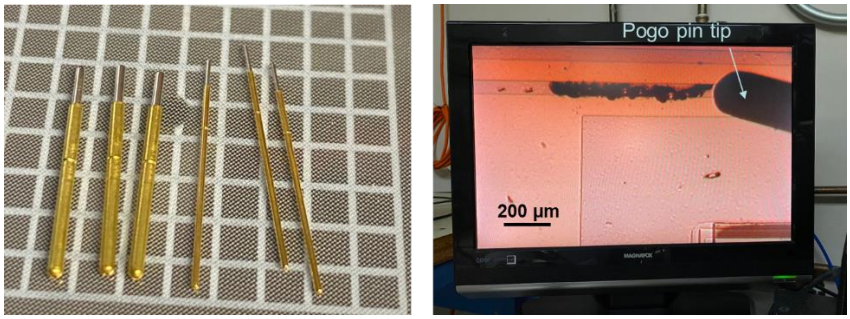

Figure 9-23. The spring-loaded pogo pins (left panel) form large contact area with the actuator electrode, facilitating higher electrical current to heat up the conducting defects. The image on the right shows the scale of the tip in reference to a worm-like defect along a segment of the Ti trace.

5.6.7 Final yield and the next stage for C1S04

Using pogo pins to contact the electrodes, a parameter analyzer to investigate and burnout the shorting paths, and a laser-cutter to vaporize bridging metal, 62 actuator cells were repaired after the second-round of fabrication of C1S04. The repair had brought the actuator yield to 99%. The four remaining unrepairable cells were shorted between the top and bottom contacts, and are distributed near the edges of the mirror, away from the critical area. They were cells in Column 1 and 12 at Row 18, Column 9 at Row 17, and Column 15 at Row 2.

For making electrical connections with control instruments, eight flexible ribbon cables were designed, fabricated, and bonded to the mirror using anisotropic conductive films (ACFs). No stress balancing X-ray reflective coating was used on C1S04 for various reasons.

As of February 2020, SAO is in possession of the mirror and will be conducting mounting and further optical characterizations. Figure 5-24 shows a picture of the mirror C1S04 in its very last moment with the author, with 284 functioning PZT actuators connected to eight flexible ribbon cables.

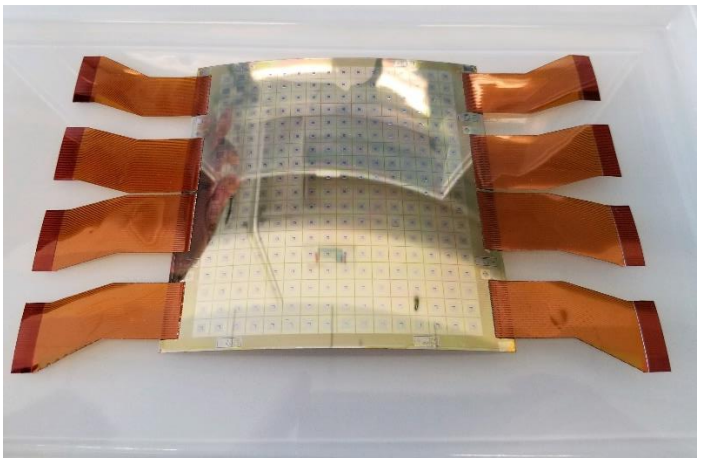

Figure 9-24. The pseudo-conical prototype mirror "C1S04" as fabricated, repaired, and attached with ribbon cables.

5.7 Chapter conclusions

Two generations of piezoelectrically adjustable X-ray mirror prototypes are reported in this chapter using individually addressable thin-film PZT actuators to locally induce strain in the optic to achieve deterministic figure correction. The mirror parts were 0.4 mm thick curved Corning Eagle XG glass substrates thermally formed on mandrels to result in a ROC of 220 mm. The earlier generation was a cylindrical optic (HFDFC3) with 112 actuator cells and the later generation (C1S04) was a pseudo-conical mirror with 288 actuator cells routed through an insulation layer using two-level metallization.

For the actuator device stack development, HFDFC3 had a 1.5 μm thick PZT film sputtered at room-temperature and crystallized in an RTA at 650°C on a 100 nm thick blanket Ti/Pt bottom electrode. The individual actuator cells were defined by patterning the Pt top electrodes into 0.5 mm (axial) × 1 mm (azimuthal) rectangles separated by 1 mm alley way distance. The Pt pattern also included the traces that wired the cells to the contact pads at the axial edges for ribbon cable bonding. The cables were bonded to the mirror using anisotropic conductive film (ACF) technology with a custom support mandrel and custom fabricated cables. 100% PZT yield was achieved for HFDFC3.

However, upon fabrication and mounting, the processing-resulted impact to the mirror figure exceeded the dynamic range of the PZT adjusters, and thus absolute figure correction could not be

realized. However, HFDFC3 provided empirical influence function data that, through FEA simulations, proved the feasibility of figure correction by the integrated PZT actuators.

In order to maintain the mirror figure within the correctable range of the PZT adjusters, modifications were made to the PZT crystallization conditions to achieve a lower integrated stress, a stress-balancing coating was applied to correct the radius of curvature, and a new low stress mirror mount was developed to mitigate the mounting impact. These improvements were verified on a pseudo-conical mirror testing piece.

For the fabrication of C1S04, the thickness of the bottom Pt electrode was halved to 50 nm to reduce the stress. The PZT layers were crystallized in a box furnace using a slower ramping rate (10°C/min) and a longer duration (18 hours) to achieve a lower and more uniform integrated stress. The number of top Pt electrodes was increased to 288 while the dimensions of a single pixel and the alley way gap were reduced to 5 mm × 5 mm and 0.2 mm in order to improve the correction resolution. A two-level metallization regime was therefore employed to accommodate the densified actuator population. To achieve this, a polymeric BCB insulation layer was deposited and patterned over the Pt top electrodes followed by deposition of a secondary Ti metal layer through and over the BCB to fanout the electrodes for ribbon cable bonding.

The two-level metallization development took two iterations. The initial attempt resulted in a large number of shorted pixels and a low yield of 15% due to densely populated defects in the 1 μm BCB layer. A rework was carefully planned and carried out to remove the Ti and BCB layers by reactive ion etching without harming the PZT actuators. A new insulation layer was then applied using three individually patterned and cured BCB coatings (2 μm in total thickness) to offset the defects. After the re-deposition of Ti, C1S04 reached an improved 77% yield. And this number was further increased to 99% as 62 out of the 66 shorted actuator cells were repaired by vaporizing the conducting defects either by electrical current induced Joule heating or laser-cutting.

At the time of completing this chapter, C1S04 is at its best condition possible and is in the possession of Smithsonian Astrophysical Observatory in preparation for mounting and future testing.

5.8 Chapter reference

[1] J. A. Gaskin, R. Allured, S. R. Bandlerc, S. Basso, M. W. Bautz, M. F. Baysinger, M. P. Biskach, T. M. Boswell, P. D. Capizzo, K-W. Chan, M. M. Civitani, L. M. Cohen, V. Cotroneo, J. M. Davis, C.T.DeRoo, M. J. DiPirro, A. Dominguez, L. L. Fabisinski, A. D. Falcone, E. Figueroa-Feliciano, J. C. Garcia, K. E. Gelmis, R. K. Heilmann, R. C. Hopkins, T. Jackson, K. Kilaru, R. P. Kraft, T. Liu, R. S. McClelland, R. L. McEntaffer, K. S. McCarley, J. A. Mulqueen, F. Özel, G. Pareschi, P. B. Reid, R. E. Riveros, M. A. Rodriguez, J. W. Rowe, T. T. Saha, M. L. Schattenburg, A. R. Schnell, D. A. Schwartz, P. M. Solly, R. M. Suggs, S. G. Sutherlin, D. A. Swartz, S. Trolier-McKinstry, J. H. Tutt, A. Vikhlinin, J. Walker, W. Yoon, and W. W. Zhang, "Lynx observatory and mission concept status," *Proc. SPIE*, vol. 10397, no. 103970S, 2017

[2] A. Vikhlinin, F. Ozel, and J. Gaskin, "Lynx X-ray observatory concept study report," Accessed: March 29, 2020. [Online]. Available: http:// wwwastro.msfc.nasa.gov/lynx

[3] D. A. Schwartz, T. L. Aldcroft, J. A. Bookbinder, V. Cotroneo, W. N. Davis, W. R. Forman, M. D. Freeman, S. McMuldroch, P. Reid, H. Tananbaum, A. Vikhlinin, S. Trolier-McKinstry, D. Wilke, and R. L. Johnson-Wilke, "The square meter arcsecond resolution X-ray telescope: SMART-X," in *Adaptive X-Ray Optics II*, *Proc. SPIE*, vol. 8503, no. 850308, 2012

[4] A. Vikhlinin, P. Reid, H. Tananbaum, D. A. Schwartz, W. R. Forman, C. Jones, J. Bookbinder, V. Cotroneo, S. Trolier-McKinstry, D. Burrows, M. W. Bautz, R. Heilmann, J. Davis, S. R. Bandler, M. C. Weisskopf, and S. S. Murray, "SMART-X, 'Square meter, arcsecond resolution X-ray telescope'," in *Conf. Space Telescopes and Instrumentation—Ultraviolet to Gamma Ra*y, vol. 8443, no. 844316, 2012

[5] M. Dubois, P. Muralt, D. V. Taylor, and S. Hiboux, "Which PZT thin films for piezoelectric microactuator applications?" *Integrated Ferroelectrics*, vol. 22, pp. 525-543, 1998

[6] V. Cotroneo, R. Allured, P. B. Reid, C. T. DeRoo, D. A. Schwartz, V. Marquez, A. A. Vikhlinin, M. Civitani, B. Salmaso, and G. Pareschi, "Thermal forming of substrates for the x-ray surveyor telescope," *Proc. SPIE*, vol. 9965, no. 99650C, 2016

[7] V. Cotroneo, R. Allured, C. T. DeRoo, K. L. Gurski, V. Marquez, P. B. Reid, and E. D. Schwartz, "Thermal forming of substrates for adjustable optics," *Proc. SPIE*, vol. 10399, no. 103990Y, 2017

[8] W. N. Davis, P. B. Reid, and D. A. Schwartz, "Finite element analyses of thin film active grazing incidence X-ray optics," *Proc. SPIE*, vol. 7803, no. 78030P, 2010.

[9] R. Wilke, R. L. Johnson-Wilke, V. Cotroneo, S. McMuldroch, P. B. Reid, D. A. Schwartz, and S. Trolier-McKinstry, "Fabrication of Adjustable Cylindrical Mirror Segments for the SMART-X Telescope," *IEEE Trans. UFFC*, vol. 61, no. 8, pp. 1386-1391, 2014

[10] R. Allured, V. Cotroneo, R. Johnson-Wilke, V. Marquez, S. McMuldroch, P. B. Reid, D. A. Schwartz, S. Trolier-McKinstry, A. Vikhlinin, and R. H. T. Wilke, "Improved control and characterization of adjustable x-ray optics," *Proc. SPIE*, vol. 9603, no. 91441D, 2015

[11] J. Walker, T. Liu, M. Tendulkar, D. N. Burrows, C. T. DeRoo, R. Allured, E. N. Hertz, V. Cotroneo, P. B. Reid, E. D. Schwartz, T. N. Jackson, and S. Trolier-McKinstry, "Design and fabrication of prototype piezoelectric adjustable X-ray mirrors," *Optics Express*, vol. 26, no. 21, pp. 27757 – 27772, 2018

[12] J. Walker, T. Liu, M. Tendulkar, D. Burrows, C. T. DeRoo, R. Allured, E. Hertz, V. Cotroneo, P. Reid, E. D. Schwartz, T. N. Jackson, and S. Trolier-McKinstry, "Design and fabrication of adjustable x-ray optics using piezoelectric thin films," *Proc. SPIE*, vol. 10399, no. 103991K, 2017

[13] R. L. Johnson-Wilke, R. H. T. Wilke, V. Cotroneo, W. N. Davis, P. B. Reid, D. A. Shwartz, and S. Trolier-McKinstry, "Improving yield of PZT piezoelectric devices on glass substrates," *Proc. SPIE*. vol. 8503, no.85030A, 2012

[14] C. T. DeRoo, R. Allured, V. Cotroneo, E. Hertz, V. Marquez, P. B. Reid, E. D. Schwartz, A. A. Vikhlinin, S. Trolier-McKinstry, J. Walker, T. N. Jackson, T. Liu, and M. Tendulkar, "Deterministic figure correction of piezoelectrically adjustable slumped glass optics," *J. Astronomical Telescopes, Instruments and Sys.*, vol 4, no. 1, pp. 019004, 2018

[15] R. Allured, S. Ben-Ami, V. Cotroneo, V. Marquez, S. McMuldroch, P. B. Reid, D. A. Schwartz, S. Trolier-McKinstry, A. A. Vikhlinin, and M. L. Wallace, "Improved control and characterization of adjustable x-ray topics," *Proc. SPIE*, vol. 9603, no. 96031M, 2015

[16] R. Allured, V. Cotroneo, R. Johnson-Wilke, V.Marquez, S. McMuldroch, P. B. Reid, D. A. Schwartz, S. Trolier-McKinstry, A. A. Vikhlinin, and R. H. T. Wilke, "Measuring the performance of adjustable x-ray optics with wavefront sensing," *Proc. SPIE*, vol. 9144, no. 9144D, 2014

[17] H. Windischmann, "An intrinsic stress scaling law for polycrystalline thin films prepared by ion beam sputtering," *J. Appl. Phys.*, vol. 62, no. 5, pp.1800-1807, 1987

[18] J. A. Thorton, "Influence of apparatus geometry and deposition conditions on the structure and topography of thick sputtered coatings," *J. Vac. Sci. Technol.*, vol. 11, no. 4, pp. 666-670, 1974

[19] J. A. Thorton, "The microstructure of sputter-deposited coatings," *J. Vac. Sci. Technol.* A, vol 4, no. 6, pp. 3059-3065, 1986

[20] V. Cotroneo, C. T. DeRoo, T. N. Jackson, V. Kradinov, T. Liu, V. Marquez, P. B. Reid, D. A. Schwartz, E. D. Schwartz, M. Tendulkar, S. Trolier-McKinstry, and J. Walker, "Process in development of adjustable optics for x-ray astronomy," *Proc. of SPIE*, vol. 10761, no. 1076109, pp. 1-10, 2018

[21] M. L. Wallace, "Performance of PZT based MEMS devices with integrated ZnO electronics," Ph.D. dissertation, Department of Materials Science and Engineering, pp. 49-65, Pennsylvania State University, University Park, PA, U.S.A, 2016

[22] J. I. Ramirez, "ZnO thin film electronics for more than displays," Ph.D. dissertation, Department of Electrical Engineering, pp. 67-101, Pennsylvania State University, University Park, PA, U.S.A, 2015

[23] M. Tendulkar, T. Liu and T. N. Jackson, "ZnO TFTs on curved substrates using optical lithography," in *61st Electronic Materials Conference (EMC)*, 2019, MRS, Session FF01, Ann Arbor, MI, U.S.A

[24] *Processing Procedures for CYCLOTENE 4000 Series Photo BCB Resins*, Dow Chemical Company, Midland, MI, U.S.A, Feb. 2005

[25] S. A. Vitale, H. Chae, and H. H. Sawin, "Etching chemistry of benzocyclobutene (BCB) low-k dielectric films in F_2 + O_2 and Cl_2 + O_2 high density plasmas," *Journal of Vacuum Science & Technologies A*, vol. 18, no. 6, pp 2770-2778, 2000

[26] C. J. Mogab, A. C. Adams, and D. L. Flamm, "Plasma etching of Si and SiO_2—the effect of oxygen additions to CF4 plasmas," *J. Appl, Phys*., vol. 49, no. 7, pp. 3796-3803, 1978

[27] C. I. M. Beenakker, J. H. J. van Dommelen, and R. P. J. van de Poll, "Decomposition and product formation in CF_4-O_2 plasma etching silicon in the afterglow," *J. Appl. Phys*., vol. 52, no. 1, pp. 480-485, 1981

[28] R. d'Agostino, F. Fracassi, C. Pacifico, and P. Capezzuto, "Plasma etching of Ti in fluorine-containing feeds," *J. Appl. Phys*., vol. 71, no. 1, pp. 462-471, 1992

[29] R. Loffler, M. Fleischer, D. P. Kern, "An anisotropic dry etch process with fluorine chemistry to create well-defined titanium surfaces for biomedical studies," *Microelectronic Engineering*, vol. 97, pp. 361-364, 2012

[30] F. Watanabe and Y. Ohnishi, "Oxygen reactive ion etching of organosilicon polymers," *Journal of Vacuum Science & Technology B*: Microelectronics Processing and Phenomena, vol. 4, no. 1, pp. 422-425, 1986

Chapter 6. Summary and future work

6.1 Summary

This thesis discussed the development thin thin-film PZT materials and devices on two types of unconventional substrates: thin flexible polyimide and curved borosilicate glass.

Due to thermal challenges in direct deposition of PZT films on polymeric substrates, a release process was developed to allow the transfer of high temperature crystallized PZT films from silicon substrates to a few micron thick polyimide layers via dissolution of an underlying ZnO release layer. This process enabled the study of electrical and piezoelectric responses for 1 μm thick partially-oriented PZT films in a fully released state. Polarization-electric field hysteresis measurements showed nearly a 45% increase in the remanent polarization (from 17.5 μC/cm^2 to 26 μC/cm^2). Poling at $3E_c$ for 15 minutes at 125°C either induced more ferroelectric and ferroelastic realignment or significantly decreased the domain walls that move reversibly, which resulted in a 17% reduction in relative permittivity compared to 3% for clamped films. These measurement results, along with Rayleigh analysis, strongly confirmed the correlation between reduced substrate clamping and improved irreversible domain wall mobility in films on polymeric substrates.

Evaluation of piezoelectric responses in the released state was attempted through measurements of d_{33} using a commercial double-beam laser interferometer. Windows were etched in the polyimide substrate so that the laser beams could directly probe the top and bottom electrodes of the released PZT structure. However, large apparent d_{33} values were measured due to uncompensated bending in the PZT membrane. The tilt of the sample structure caused the two laser-beams to misalign, thus adding erroneous phase-change contributions to the interference intensity. Although correct d_{33} data in the released state were not obtained, the experiments identified a critical measurement artifact in the system, which has been overlooked by reports in the literature. Solutions were proposed to address the excess bending via (1) patterning the PZT layer into isolated islands for each top electrode, and (2) expanding the polyimide etch window so that no polyimide remains directly below the PZT to introduce structural asymmetry.

The release process served as the pedestal for the integration of flexible PZT ultrasonic transducers on flexible polyimide substrates. Transducers were demonstrated using 1 μm thick PZT films patterned into bar resonators targeted to operate in the width extension mode. Flexible ribbon cables were fabricated and bonded to the released transducers and inserted into a ZIF connector mounted on a printed circuit board to establish external electrical connections. The ability to transmit and receive acoustic signals in water was first confirmed with a 3.5 MHz commercial transducer. Then, pitch-catch was demonstrated with two 100 μm × 1000 μm neighboring elements respectively transmitting an acoustic signal to a reflector at a distance of 1.5 cm and receiving the reflected signal. The element in receive detected a 0.2 mV pre-amplified signal at a driving frequency of 9.5 MHz. Hydrophone measurements determined a sound pressure output of these devices at 33 kPa and a -6dB bandwidth at 32% at 6 mm distance. These are the first high-temperature crystallized thin-film PZT ultrasonic transducers transferred over a large area to flexible polymeric substrates that have been reported. The development of flexible PZT devices provides a pathway for multiple applications that are not accessible by conventional bulk or rigid substrate-based thin-film devices.

For the development of PZT films on curved glass substrates, two generations of piezoelectrically adjustable X-ray mirror prototypes were investigated. The mirror segments were integrated with individually addressable thin-film PZT actuators to locally induce strain in the optic to achieve deterministic figure correction. The mirror parts were 0.4 mm thick curved Corning Eagle XG glass substrates with a ROC of 220 mm. The earlier generation was a cylindrical optic (HFDFC3) with 112 actuator cells and the later generation (C1S04) was a pseudo-conical mirror with 288 actuator cells routed through an insulation layer using two-level metallization.

For the actuator device stack development, HFDFC3 had a 1.5 μm thick PZT film sputtered at room-temperature and crystallized in an RTA at 650°C on a 100 nm thick blanket Ti/Pt bottom electrode. The individual actuator cells were defined by patterning the Pt top electrodes into 0.5 mm (axial) × 1 mm (azimuthal) rectangles separated by 1 mm alley way distance. The Pt pattern also included the traces that wired the cells to the contact pads at the axial edges for ribbon cable bonding. The cables were bonded to

the mirror using anisotropic conductive film (ACF) technology with a custom support mandrel and custom fabricated cables. 100% PZT yield was achieved for HFDFC3. Upon fabrication and mounting, the processing-induced impact to the mirror figure exceeded the dynamic range of the PZT adjusters, and thus absolute figure correction could not be realized. However, HFDFC3 provided empirical influence function data that, through FEA simulations, proved the feasibility of figure correction by the integrated PZT actuators.

For the fabrication of C1S04, the thickness of the bottom Pt electrode was halved to 50 nm to reduce the stress. The PZT layers were crystallized in a box furnace using a slower ramping rate (10°C/min) and a longer duration (18 hours) to achieve a lower and more uniform integrated stress. The number of top Pt electrodes was increased to 288 while the dimensions of a single pixel and the alley way gap were reduced to 5 mm × 5 mm and 0.2 mm in order to improve the correction resolution. A two-level metallization regime was therefore employed to accommodate the densified actuator population. To achieve this, a photo-patternable BCB insulation layer was deposited and lithographically patterned over the Pt top electrodes followed by deposition of a secondary Ti metal layer through and over the BCB to fanout the electrodes for ribbon cable bonding.

The two-level metallization development took two iterations. The initial attempt resulted in a large number of shorted pixels and a low yield of 15% due to densely populated defects in the 1 μm BCB layer. A rework was carefully planned and carried out to remove the Ti and BCB layers by reactive ion etching without harming the PZT actuators. A new insulation layer was then applied using three individually patterned and cured BCB coatings to offset the defects. After the re-deposition of Ti, C1S04 reached an improved 77% yield. And this number was further increased to 99% as 62 out of the 66 shorted actuator cells were repaired by vaporizing the conducting defects either by electrical current induced Joule heating or laser-cutting.

6.2 Future work

6.2.1 Substrate-agnostic release process

The first recommendation for future work is to advance the release technique described in Chapter 2 into a substrate-agnostic process to benefit a broader scope of applications. The transfer destination does not need to be limited to polyimide or a solution-cast film, but can include a variety of materials that are either flexible or rigid, such as metal foils, plastic sheets, glass plates, and even textiles.

It is proposed that a non-solution-cast substrate could be added to the device stack prior to release by laminating the two components using a polymeric film as a bonding agent.

Preliminary experiments along these lines were conducted by bonding a 1 mm thick borosilicate glass substrate to a Si piece and separately, to a polyimide/PZT/Si stack using polymethylglutarimide (PMGI), a polymer developed for photolithography applications that is commonly known as LOR [1]. Heat and pressure were applied to the sandwiched structure using a hot press in a non-vacuum, non-cleanroom environment, as schematically illustrated in Figure 6-1 (a).

For the PMGI application, the glass piece was first cleaned with a sulfuric acid and chromic acid mixture (KleanAR, Avantor, USA) and treated with an oxygen plasma. PMGI solution (MicroChem Corp, USA) of 15.8 w/w% concentration was spin-coated on the clean substrate at 2000 RPM and baked at 180°C on a hotplate in air for 10 minutes to obtain a ~3 μm thick film. To carry out the bonding, the PMGI-coated substrate was pressed against the device stack on a hot press at about 4000 PSI pressure level while the temperature was increased from room temperature to 240°C and held for 20 minutes [2,3]. The pressure was removed when the hot press was cooled below 40°C. Figure 6-1 (b) shows an example of a laminated structure with Si attached to a piece of 1 mm thick borosilicate glass that is partially coated with PMGI. The boundary of the bonding agent and the bonding interface can be visualized through the transparent glass substrate. An air bubble, resulting from trapped dust particles, is observed at the interface. Panel (c) is an example of a polyimide/PZT/Si stack bonded to a glass piece.

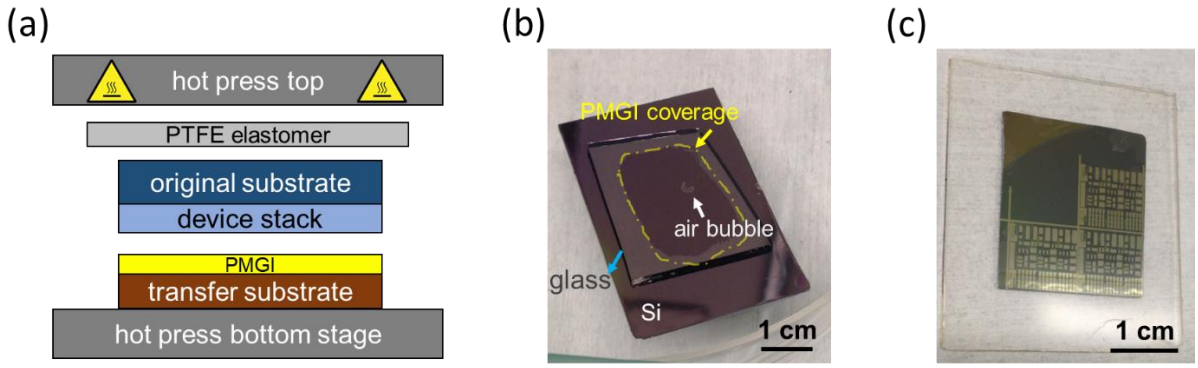

Figure 10-1. (a) Schematic of the hot press setup that bonds the device stack to an arbitrary substrate coated with a PMGI layer as adhesive. A PTFE elastomer layer over the bonding stack serves to distribute the force more uniformly. (b) A laminated stack consisting of silicon (bottom) and a glass piece (top) partially coated with PMGI covering ~80% of the glass. The bonding interface can be seen through the glass. An air bubble at the interface is a result of dust particles trapped in between. (c) The image of a polyimide/PZT/Si device stack attached to a glass piece.

To further this work, the bonding strength needs to be quantitatively evaluated and improved. Delamination occurred in the bonded stack both before and after transfer. In the first case, the glass became separated from the counterpart during a mechanical lapping process for silicon thickness reduction. In the second case, after the flexible device structure was transferred to the glass piece, the PZT/polyimide combination delaminated as soon as it was exposed to DI water. The bonding strength is presumably a function of many parameters, such as substrate surface energy, the temperature and pressure profile of the hot press, contamination from the ambient, and the choice of the adhesive film. A thorough investigation of these parameters is imperative to achieve a reliable bonding process.

6.2.2 Breaking the rules with more than substrates

As the release process enables access to the film-substrate interface at growth, the bottom electrode can be added after crystallization. This sequence-change relaxes the material selection restriction on the bottom electrode due to undesirable reactivity and diffusivity at high temperature. Therefore, there is more freedom in terms of choosing the conductivity of the electrode or the work function for adjusting the Schottky barrier height. In addition, the post-crystallization electrode deposition

enables consistent defect chemistry at growth as the piezoelectric layer can be grown on the same surface, which then allows the investigation of electrode-dependent defect chemistry.

The lifting of the constraints not only applies to the bottom electrode, it will also affect how integration works with another device or field of technology. The possibility of shifting the high-temperature annealing and/or the contaminant-containing (e.g., Pb) process to the beginning of a fabrication sequence can enable the integration with, or provide an effective alternative to previously incompatible processes. For example, the release and transfer method can be considered as an alternative approach to integrate thin-film PZT devices with Si-based CMOS circuitry.

6.2.3 Further investigation for the PZT degradation by imidization

There are still unanswered questions about the PZT degradation during imidization of the poly(amic acid) precursor PI-2611. Though a workable approach was developed to co-process PI-2611 with patterned PZT, neither the degradation nor the damage-prevention mechanism was clearly understood. The variations in the results for patterned and blanket PZT/Pt structures suggest that the fundamentals of the processing are incompletely controlled. Further investigation is therefore recommended. An important factor that hinders the understanding of the degradation is the uncertainty of the species evolved during the polyimide imidization process. To tackle this problem, thermogravimetric analysis coupled with mass spectrometer (TGA/MS) is suggested to analyze and compare the gaseous species formed during the PI-2611 curing by varying the PZT/Pt structure (blanket *vs.* patterned) and the imidization ambient (in air *vs.* inert gas). Once the source is understood, its interactions with PZT and the prevention mechanisms could be further investigated.

6.2.4 Suppressing excess bending in the d_{33} measurement system

In Chapter 4, it was predicted that expanding the polyimide etch-window and patterning the PZT into individual islands could prevent large-magnitude bending, and thus keeping the top and bottom

measurement beams aligned. Misalignment in the two measurement beams would add an additional pathlength contribution to the interference intensity and result in inflated d_{33} values. In case that excess bending still persists with the modified sample structure, fixing the flexible structure (with patterned polyimide) to a transparent, rigid substrate could perhaps be considered as an alternative. It is to be emphasized here that there is no intention to fully suppress bending, but to keep the magnitude below a threshold that the two measurement beams stay aligned. Such a configuration could be realized using the substrate-bonding process like that proposed in 6.2.1.

As schematically illustrated in Figure 6-2, prior to release, the device stack is bonded to a glass piece using PMGI (left). Then, through XeF_2 etching Si (discussed below), the patterned PZT/polyimide combination is transferred to the glass (right).

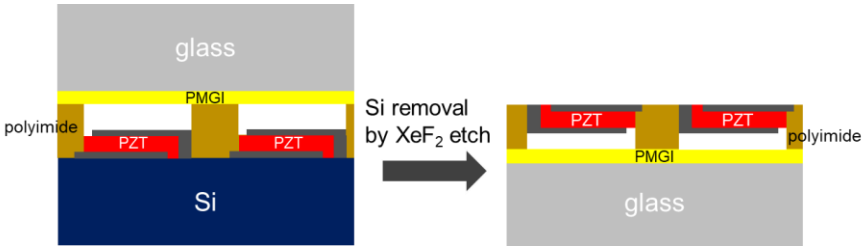

Figure 10-2. Schematics for the proposed configuration of a DBLI testing sample with minimized bending contribution. The device stack is bonded to a glass piece using PMGI (left) before release. Through XeF_2 etching Si, the patterned PZT/polyimide combination is transferred to the glass (right).

It is suggested that the release be carried out by etching the Si substrate with XeF_2 vapor as the ZnO sacrificial-etching approach is constrained by a difficulty in etchant mass transport. When the sacrificial layer is sandwiched between two rigid substrates, it becomes hardly accessible by the acetic acid as little exchange takes place between reaction products and fresh etchant solution. XeF_2 vapor etching, on the other hand, has no difficulty accessing the sacrificial layer, i.e., the silicon substrate. The etching reaction takes place in a chamber regulated at few Torr pressure level, at which XeF_2 exists in the vapor phase and reacts with Si to form volatile products SiF_4 and Xe. The extremely high selectivity (>1000:1) causes no damages to crystalline PZT, Pt, polyimide, and glass. [4,5].

Preliminary etching experiments were performed in a Xactix XeF_2 etcher (SPTS Technologies, USA) to remove the Si substrate as part of the structure in Figure 6-1 (c). The etching was carried out in multiple reaction cycles at 2 Torr with a fixed time of 60 seconds for each cycle. One cycle started with introduction of the XeF_2 etchant to the chamber to react with Si and continued until the gaseous species (remaining etchant and reaction products) were pumped away. The optimal duration is the time needed to consume all the XeF_2 etchant fed into the reaction chamber. The etch rate was a strong function of the exposed Si lateral dimension due to the loading effect. For a 1 cm × 1 cm Si piece of 0.55 cm thick, ~300 cycles were used for a complete removal. The number of cycles was, however, substantially increased to over 2000 for a 2.5 cm × 2.5 cm Si. The slow etch was resolved by reducing the Si thickness through mechanical lapping prior to etching.

Using the PMGI bonding approach in combination with the subsequent XeF_2 etching method, the patterned Pt/PZT/Pt/polyimide stack can be transferred to the receiving glass substrate, achieving the structure illustrated in Figure 6-2 (right).

The proposal of this structure is under the assumption that the glass does not deform when the PZT is actuated. The pathlength change as laser propagate through the glass should be a static contribution and therefore can be compensated.

While the PZT is in the released state de-clamped from the Si substrate, the structure is prevented from excess flexing as the polyimide is bound to the glass. Bending is likely still present in the structure but perhaps not large enough to cause misalignment in the two measurement laser beams. However, this configuration requires the laser beam to travel through a series of non-air media: glass, PMGI, and polyimide. It is therefore imperative to investigate and quantify the possible phase change contributions and perform corresponding compensation *ex situ*. As analyzed in Section 4.2.1, the difference in the refractive index of the non-air medium (i.e., polymer and glass) changes the wavelength of the laser beam and alters the pathlength when propagating in the medium relative to air. The phase change contribution can therefore be simulated based on the information of the refractive index and thickness of the polyimide, PMGI, and glass. Then, empirically, the verification can be achieved by measuring the 3-

direction displacement of PZT films of a known d_{33} that is clamped on a double-side-polished Si substrate and comparing the results with the same structure mounted on a receiving glass substrate with polyimide and PMGI sandwiched in between.

6.2.5 Investigation of the roles of grain size and defect chemistry

Relative to bulk PZT ceramics, thin-film PZT has very different (mostly inferior) material properties due to the smaller grain size, different charge transport mechanisms, and the substrate clamping effect [6-10]. As the release method in Chapter 2 and 3 enabled fully released PZT films, the relative roles of grain size and/or defect chemistry in controlling the properties can be deconvoluted from the substrate-clamping effect. To do so, it is suggested that the d_{33} coefficient, dielectric permittivity, P-E hysteresis, and Rayleigh analysis results in fully released PZT films be compared with those of bulk ceramics of the same composition. The study can certainly be expanded to other piezoelectrics besides PZT.

6.2.6 Impact of thermally insulating substrates on breakdown strength of released PZT films

The patterned PZT resonators on Si showed lower electric breakdown strength relative to blanket PZT films on the same substrates, which was likely due to PZT sidewall damage and/or redeposition of conductive Pt on the sidewall during the reactive ion etch [11]. The breakdown strength was observed to have further deteriorated once the patterned PZT devices were transferred from Si to polyimide. For example, the released PZT films could not be driven with a maximum excursion field exceeding 400 kV/cm for polarization-electric field (P-E) hysteresis measurements, whereas a 600 kV/cm was approximately the average maximum field for films on Si. Going from a good thermal conductor to a thermal insulator, it is suspected that the removal of the thermal sink (i.e., Si) impeded heat dissipation, thus reducing the breakdown strength. It is therefore proposed that highly accelerated lifetime tests (HALT) and thermal camera assisted current-voltage (I-V) measurements be conducted to assess the lifetime characteristics and breakdown mechanisms of patterned PZT films on thermally insulating

substrates [12, 13]. Adding a thermal camera to the experiment will be helpful for visualizing heat dissipation.

6.2.6 Application-driven development for flexible PZT transducers

In Chapter 3, basic underwater acoustic characterization was conducted for the fabricated flexible PZT transducers to verify their ability to transmit and receive acoustic signals and assess the operating frequency, sound pressure level, and bandwidth. However, the actual vibration mode of each resonator is unknown. A laser vibrometer measurement is therefore suggested to assess whether the devices operate in a width extension mode as designed, or additional contributions are added to the response.

After achieving a thorough acoustic characterization, the next phase for the flexible PZT transducer development is integration into a complete imaging system. This means that components such as backing layers, impedance matching layers, shielding, and control electronics must be considered and added to the system to facilitate imaging.

A recommended route for the control electronics development is to employ flexible ZnO thin-film transistors (TFTs). Integration of thin-film PZT actuators with ZnO TFTs has been demonstrated on glass substrates for development of X-ray optics by Wallace *et al*. and Israel *et al*. [14, 15]. Flexible ZnO TFTs on PI-2611 polyimide substrates have also been reported by Li *et al*. [16]. The ZnO electronics could reduce the number of wires by using a row-column addressing system for a large number of transducer elements.

Lastly, a quantitative flexibility test is suggested for the transducer devices both *ex situ* and *in situ* (with ribbon cables attached). Li *et al*. have developed three apparatuses to flex and bend polyimide substrate-based ZnO TFT samples in a controllable manner [17]. The testing rigs can realize unguided bending, controlled-radius bending, and bending without additional tensile stress, respectively. The number of bending iterations is controlled and recorded by a computer program. Details are given in [17].

6.3 Chapter reference

[1] R. M. Kopchik, "Imidized acrylic polymers," U.S. Patent 4 246 374 A, Jan. 20, 1981.

[2] T. Matsumae, A. D. Koehler, J. D. Greenlee, T. J. Anderson, H. Baumgart, G. G. Jernigan, and F. J. Kub, "Temporary bonding with polydimethylglutarimide based lift off resist as a layer transfer platform," *ECS Journal of Solid State Science and Technology*, vol. 4, no. 7, pp. 190-194, 2015

[3] A. V. Gupta, A. N. Brigeman, E. W. Gomez, and T. N. Jackson, "Simple polymethylglutarimide microfluidic channels with hydrogel-assisted fluid exchange," *IEEE Transactions on Nanobioscience*, vol. 17, no. 2, pp. 96-101, 2018

[4] H. F. Winters, and J. W. Coburn, "The etching of silicon with XeF_2 vapor," *Appl. Phys. Lett.*, vol. 34, no. 70, pp. 70-73, 1979

[5] Q. Zhou, J. M. Cannata, R. J. Meyer, D. J. Van Tol, S. Tadigadapa, W. J. Hughes, and S. Trolier-McKinstry, "Fabrication and characterization of micromachined high-frequency tonpilz transducers derived by PZT thick films," *IEEE Trans. UFFC*, vol. 52, no. 3, pp. 350-367, 2005

[6] C.A. Randall, N. Kim, J.-P. Kucera, W. Cao, and T.R. Shrout, "Intrinsic and extrinsic size effects in fine-grained morphotropic-phase-boundary lead zirconate titanate ceramics," *J. Am. Ceram. Soc.*, vol. 81, pp. 677-688, 1998

[7] Y. Bastani, T. Schmitz-Kempen, A. Roelofs, N. Bassiri-Gharb, "Critical thickness for extrinsic contributions to the dielectric and piezoelectric response in lead zirconate titanate ultrathin films," *J. Appl. Phys*. vol. 109, pp. 014115, 2011

[8] M. V. Raymond, and D. M. Smyth, "Defects and charge transport in perovskite ferroelectrics," *J. Phys. Chem. Solids*, vol. 57, no. 10, pp. 1507-1511, 1996

[9] T. Fromling, A. Schintlmeister, Herbert Hutter, and Jurgen Fleig, "Oxide ion transport in donor-doped $Pb(Zr_xTi_{1-x})O_3$: the role of grain boundaries," *J. Am. Ceram. Soc.*, vol. 94, no. 4, pp. 1173-1181, 2011

[10] N. Donnelly, and C. A. Randall, "Mixed conduction and chemical diffusion in a $Pb(Zr_{0.53}, Ti_{0.47})O_3$ buried capacitor structure," *Appl. Phys. Lett.*, vol. 96, pp. 052906, 2010

[11] J. I. Yang, "Reliability and aging in patterned $Pb(Zr_{0.52}Ti_{0.48})O_3$ films, PhD dissertation, Department of Materials Science and Engineering, pp. 82-134, The Pennsylvania State University, University Park, PA, U.S.A, 2016

[12] W. J. Minford, "Accelerated life testing and reliability of high k multilayer ceramic capacitors," *IEEE Transaction on Components, Hybrids and Manufacturing Technology*, vol. CHMT-5, no. 3, 1982

[13] S. K. Kurtz, S. Levinson, and D. Shi, "Infant mortality, freaks, and wear-out: Application of modern semiconductor reliability methods to ceramic multilayer capacitors," *J. Am. Ceram. Soc.*, vol. 72, no. 12, pp. 2223-2233, 1989

[14] M. L. Wallace, “Performance of PZT based MEMS devices with integrated ZnO electronics,” Ph.D. dissertation, Department of Materials Science and Engineering, pp. 49-65, Pennsylvania State University, University Park, PA, U.S.A, 2016

[15] J. I. Ramirez, “ZnO thin film electronics for more than displays,” Ph.D. dissertation, Department of Electrical Engineering, pp. 67-101, Pennsylvania State University, University Park, PA, U.S.A, 2015

[16] H. U. Li, and T. N. Jackson, "Oxide semiconductor thin film transistors on thin solution-cast flexible substrates," *IEEE Electron Device Letters*, vol. 36, no. 1, pp. 35-37, 2014

[17] H. U. Li, and T. N. Jackson, “Flexibility testing strategies and apparatus for flexible electronics,” *IEEE Trans. Electron Devices*, vol. 63, no. 5, pp.1934-1939, 2016

VITA

Tianning Liu

Tianning Liu was born in Nanjing, China, a large historical city that served as the capital of various Chinese dynasties and kingdoms. She lived there until graduating from high school in 2008, when she flew to the United States to attend Pennsylvania State University in State College, PA. Tianning started as a student in Smeal College of Business but changed her direction to pursue a degree in Electrical Engineering two years later. After obtaining a B.S. in Electrical Engineering in 2013, Tianning remained at Penn State to further her study in the Ph.D. program in Electrical Engineering. She joined Prof. Kenji Uchino's research group and conducted research on bulk PZT ceramics in 2013. In 2015, she switched her focus to study ZnO thin-film transistors and PZT thin-film devices under the supervision of Prof. Thomas N. Jackson and Prof. Susan Trolier-McKinstry. Tianning's main research focus is flexible piezoMEMS device design and fabrication.